# Chemistry of Carbonaceous Aerosols: Studies of Atmospheric Processing and OH-Initiated Oxidation

by

Kirsten S. Johnson

B.S. Chemistry, University of Idaho, 2002
B.A. French, University of Idaho, 2002

Submitted to the Department of Chemistry
in partial fulfillment of the requirements for the degree of

DOCTOR of PHILOSOPHY in CHEMISTRY

at the

MASSACHUSETTS INSTITUTE OF TECHNOLOGY
[February 2008]
August 2007



Author .....
Department of Chemistry
August 31, 2007

Certified by .....
Mario J. Molina
Institute Professor
Thesis Supervisor

Accepted by .....
Robert W. Field
Chairman, Department Committee on Graduate Students

This doctoral thesis has been examined by a Committee of the Department of Chemistry as follows:

Professor Jeffrey I. Steinfeld ..... Thesis Chairman

Professor Mario J. Molina..... Research Advisor

Professor Sylvia T. Ceyer ..... Department of Chemistry

# Chemistry of Carbonaceous Aerosols: Studies of Atmospheric Processing and OH-Initiated Oxidation

by

Kirsten S. Johnson

Submitted to the Department of Chemistry
on August 31, 2007, in partial fulfillment of the
requirements for the degree of
DOCTOR of PHILOSOPHY in CHEMISTRY

## Abstract

Carbonaceous aerosols are among the most prevalent yet least understood constituents of the atmosphere, particularly in urban environments. We have performed analyses of field samples and laboratory studies to probe the physico-chemical properties of soot and organic aerosols in a complimentary approach to obtain information essential for understanding their atmospheric evolution and environmental effects.

Samples of particulate matter $\leq 2.5$ $\mu$m in diameter ($PM_{2.5}$) were collected from the Mexico City Metropolitan Area (MCMA) for both bulk compositional analysis and single particle characterization. Approximately 50% of the non-volatile component of $PM_{2.5}$ was found to consist of carbonaceous material, including both soot and organics. Other major components included sulfates, soil/dust and heavy metals indicative of industrial emissions. Single particle analysis confirmed the prevalence of soot particles; our evidence suggests they quickly became internally mixed with sulfates and other inorganic compounds in a day or less through extensive processing during their atmospheric residence times.

In the second half of our approach, a Quartz Crystal Microbalance - Chemical Ionization Mass Spectrometry (QCM-CIMS) system was developed to probe the OH-initiated oxidation of organic and soot thin films as atmospheric aerosol surrogates. Mass loss (volatilization) from the films was observed upon exposure to OH radicals in the presence of $O_2$ at 295 K and 100 Torr. The loss rate was found to be linearly dependent on OH and independent of $O_2$ concentrations over the range $O_2$ $\sim 10^{12}$ to $2 \cdot 10^{18}$ molec/cm$^3$. A relatively slower mass loss rate in the presence of $NO_x$ suggests simultaneous formation of alkyl nitrate compounds potentially important in polluted urban environments. Experimental data were used to extract the rate constants of individual steps within the context of a previously proposed oxidation mechanism. Volatilization was observed in 15% relative humidity at a rate slower than under dry conditions, suggesting water adsorption to the surface. Initially hydrophobic alkane surfaces became noticeably hydrophilic as a result of oxidation. Although the oxidized surfaces did not exhibit measureable water uptake, water contact angle measurements show increased hydrophilicity, suggesting formation of polar (oxygen-containing) organic functional groups.

Thesis Supervisor: Mario J. Molina
Title: Institute Professor

## Acknowledgments

This work has been more challenging and rewarding than I could have imagined. It would never have materialized without the advice and encouragement of many people.

My research advisor, Mario Molina, it has been an extraordinary privilege to have been a member of your group. Thank you for your advice and patience, for encouraging me to tackle the difficult problems, and for imparting upon me a deep respect for the environment and our shared responsibility to preserve it. The confidence you instilled in me during these years never failed to push me forward to further my scientific understanding and I will value this throughout my life.

Coming to MIT has been one of the best decisions of my life, not only for the opportunity to learn from such distinguished faculty and my fellow students, but also for opening up new perspectives on the excitement of scientific research and the diversity and complexities of our world. I loved (almost) every minute of it.

Participating in the MCMA-2003 campaign was an enormous opportunity to learn and appreciate the importance of our research. I would like to thank Luisa Molina for her guidance throughout. I was extremely fortunate to have worked with a strong network of mentors and colleagues, particularly Alex Laskin and Jose Jimenez whose advice shaped a great portion of this thesis. Both were more than generous with their time and always encouraged me to ask questions and voice my thoughts. My two trips to Mexico – Mexico City during the MCMA-2003 campaign and later Puebla for the PIXE-2007 conference – left me with great memories, friendships, and plans to return as soon as possible.

My profound gratitude goes to Kevin Kuchta and Brian Regel with whom I spent countless hours on the phone troubleshooting mass spec woes, and to Randall for his exertise in building the CIMS lens assembly. Without these gentlemen I might never have had a working instrument in the first place.

Friends and colleagues of the Molina group – Rainer Volkamer, Jong-Ho Park, Andrey Ivanov, Miguel Zavala, Philip Sheehy, Jun Noda, Bilal Zuberi, Faye McNeill, Ed Dunlea, Juan Cabada, Ben de Foy, Wenfang Lei, Liz Fitzgerald, Gregory Poskrebyshev, Diana Roseborough, Marco Martinez – you taught me as much about life as about science. With more time I would have loved to learn at least seven other languages. I want to emphasize

acknowledgment to Jong-Ho, Andrey, and Rainer who provided indispensible help battling lab gremlins ... I think we gained the upper hand in the end. Moving an entire physical chemistry lab 3,000 miles cross-country is definitely not for the faint-of-heart. Thanks to Andrey for many lengthy discussions on heterogeneous OH-initiated oxidation (reminding me how incredibly complex the system is), but more importantly for introducing me to Pink Floyd. Rainer always managed to ask the critical questions that required months of frustrating work to answer, but thankfully also was a great friend with a sharp sense of humor. Thanks to Jong-Ho for his extreme generosity and kindness, essential CIMS advice, and putting up with my choice of music in the lab.

My friends with unfailingly patient ears – Karen Raitanen, Andrea Gabert, Mala Radhakrishnan, Melva James, Denise Main, Vincent Bourdonneau, Katja Dzepina, Lauren DeFlores, Lisa Liu, Claudia Carvajal, Jen Seymour, Riz Virk, Henna Shah, Kielo Ahomaa – thank you for being there, particularly for making me laugh and reminding me that 5 cups of coffee per day is probably a little too much (except while writing your thesis!).

Finally there are simply no words to fully express the debt I owe to my family. Mom, Dad, Kevin – your support has brought me through some of the greatest challenges I have ever faced. I dedicate this to you.

# Contents


**1 Introduction** **17**

1.1 Definitions . . . . . 17

1.1.1 Size distribution . . . . . 18

1.1.2 Carbonaceous aerosols . . . . . 19

1.2 Atmospheric aerosol processing . . . . . 20

1.3 Heterogeneous reactivity . . . . . 20

1.4 Hydrophobic vs. hydrophilic properties . . . . . 22

1.5 Considerations for field analysis vs. laboratory study . . . . . 22

1.6 Thesis outline . . . . . 23

**2 Chemical composition and sources of urban aerosols** **25**

2.1 Mexico City Metropolitan Area . . . . . 25

2.2 PIXE, PESA, STIM analysis techniques . . . . . 26

2.3 Experimental . . . . . 27

2.4 Results on $PM_{2.5}$ composition and sources . . . . . 29

2.4.1 Sulfate . . . . . 30

2.4.2 Industry . . . . . 32

2.4.3 Biomass burning . . . . . 34

2.4.4 Soil/dust . . . . . 35

2.4.5 STIM and non-volatile $PM_{2.5}$ speciation . . . . . 37

2.5 Discussion within context of other studies on MCMA particulate emissions 37

2.6 Comparison with Aerosol Mass Spectrometry . . . . . 40

2.6.1 Aerosol collection . . . . . 41

2.6.2 PIXE sulfur and AMS sulfate . . . . . 42

2.6.3 PESA hydrogen and AMS organics . . . . . 45

**3 Atmospheric processing of soot** **51**

3.1 Introduction . . . . . 51

3.2 Experimental . . . . . 54

3.3 Results . . . . . 56

3.3.1 Freshly-emitted soot from traffic . . . . . 56

3.3.2 La Merced market area . . . . . 58

3.3.3 Particles collected from the CENICA Supersite . . . . . 59

3.4 Atmospheric processing and internal mixing . . . . . 61

3.5 Conclusions and atmospheric importance . . . . . 65

**4 OH-initiated oxidation of carbonaceous films as surrogates for atmospheric aerosols** **67**

4.1 Introduction . . . . . 67

4.1.1 Reaction mechanism for OH-initiated oxidation of alkane compounds in the gas phase . . . . . 68

4.1.2 OH attack . . . . . 70

4.1.3 Alkyl peroxy radical reactions . . . . . 70

4.1.4 Alkoxy radical reactions . . . . . 72

4.1.5 Atmospheric oxidation in liquids and solids . . . . . 75

4.1.6 Status of heterogeneous studies . . . . . 76

4.2 Experimental . . . . . 78

4.2.1 Chemical Ionization Mass Spectrometry (CIMS) . . . . . 78

4.2.2 Quartz Crystal Microbalance (QCM) . . . . . 81

4.2.3 Flow system . . . . . 82

4.2.4 Sample preparation and characterization . . . . . 85

4.3 Results on OH-initiated oxidation of an alkane surface . . . . . 86

4.3.1 OH–surface calibration . . . . . 87

4.3.2 Role of $O_2$ in alkane oxidation . . . . . 88

4.3.3 Effect of $NO_x$ . . . . . 93

4.3.4 Kinetics modeling of the heterogeneous reaction mechanism . . . . . 98

4.4 Carbon chain length dependence . . . . . 102

4.5 Organic functional group investigation . . . . . 105
4.6 Soot reactivity . . . . . 107
4.7 Discussion and conclusions . . . . . 109

**5 Hydrophilic properties** **111**
5.1 Introduction . . . . . 111
5.2 Hydration study of internally-mixed urban aerosols . . . . . 113
5.2.1 FTIR – flow cell technique . . . . . 113
5.3 Heterogeneous OH-initiated oxidation in the presence of water vapor . . . . 118
5.3.1 CIMS detection under relative humidity . . . . . 118
5.4 Conclusions . . . . . 121

**6 Conclusions** **123**
6.1 Emissions sources and chemical composition of urban aerosols . . . . . 124
6.2 Laboratory studies of OH-initiated oxidation of organics and soot . . . . . 125
6.3 Atmospheric processing: physical and chemical mechanisms as related to aerosol lifetimes . . . . . 126

**7 Recommendations for future research** **129**
7.1 S(IV) to S(VI) oxidation on a soot surface . . . . . 129
7.2 Influence of surface properties on oxidation kinetics of organic aerosol . . . 130
7.3 Effects of relative humidity in the heterogeneous OH-initiated oxidation of organic aerosol . . . . . 130
7.4 Temperature dependence in heterogeneous oxidation of organic aerosol . . . 131

# List of Figures


1-1 Atmospheric aerosol size distribution by mass and number . . . . . 18

1-2 Schematic representation of carbonaceous aerosol processing . . . . . 20

2-1 Topographical map of the Mexico City Metropolitan Area . . . . . 26

2-2 Typical energy levels and X-ray emission lines . . . . . 27

2-3 $PM_{2.5}$ samples collected by DRUM impactor . . . . . 28

2-4 Experimental setup for PIXE, PESA, STIM . . . . . 29

2-5 Emission source categories by Positive Matrix Factorization (PMF). . . . . 31

2-6 Time series of elemental markers for industrial emissions during MCMA–2003 33

2-7 Time series of fuel oil components and $SO_2$ during MCMA–2003 . . . . . 33

2-8 Elemental markers of biomass burning during MCMA–2003 . . . . . 34

2-9 Soil-related elements vs. organic H . . . . . 35

2-10 Time series of soil-related elements during MCMA–2003 . . . . . 36

2-11 Speciation of non-volatile $PM_{2.5}$ . . . . . 38

2-12 Time series of Zn and Cu during the MILAGRO campaign . . . . . 40

2-13 Mixed soot–metal particles collected during MILAGRO . . . . . 40

2-14 Sulfate time series by PIXE and AMS . . . . . 42

2-15 PIXE vs. AMS measurement of $SO_4^{-2}$ during MCMA–2003 . . . . . 43

2-16 PIXE sulfur vs. PESA hydrogen . . . . . 45

2-17 MCMA–2003 time series for PESA and AMS organic aerosol mass . . . . . 46

2-18 PESA organic H vs. AMS total organics . . . . . 46

2-19 PESA organic H vs. AMS organic components HOA and OOA . . . . . 47

2-20 Total organic aerosol mass obtained via PESA organic H. . . . . 48

3-1 Soot microstructure . . . . . 52

3-2 Three-dimensional structure of soot proposed by Akhter et al. (1991) . . . . 52
3-3 Time Resolved Aerosol Collector (TRAC) . . . . . 55
3-4 SEM images of freshly-emitted soot collected in city traffic during MCMA–2003 57
3-5 Normalized distribution of S/C ratios from CCSEM/EDX analysis of MCMA aerosol samples and of laboratory-generated ammonium sulfate particles . . 58
3-6 SEM images of partially-processed soot particles sampled near the downtown La Merced site during MCMA–2003 . . . . . 59
3-7 SEM images of ambient particles collected during MCMA–2003 . . . . . 59
3-8 Composition of a heterogeneous soot particle by SEM/EDX analysis . . . . 60
3-9 Surface characterization of particles collected during MCMA–2003 by TOF-SIMS analysis . . . . . 61
3-10 TEM images of mixed soot/sulfate particles . . . . . 62
3-11 Particle composition as a function of time as measured by CCSEM/EDX during MCMA–2003 . . . . . 62

4-1 Reaction mechanism for OH-initiated oxidation of *n*-hexane . . . . . 71
4-2 Gas-phase OH + RH reaction rate as a function of alkane chain length . . . 72
4-3 Chemical Ionization Mass Spectrometer (CIMS) . . . . . 79
4-4 QCM–CIMS system . . . . . 80
4-5 CIMS calibration plots for $NO_2$ and OH . . . . . 84
4-6 CIMS spectrum for $OH^-$ and $NO_2^-$ with $SF_6^-$ as the parent ion . . . . . 85
4-7 QCM measurement of alkane mass loss upon exposure to OH . . . . . 87
4-8 Mass loss by an ODT monolayer ($C_{18}$ alkane) . . . . . 88
4-9 Mass loss by $C_{36}H_{74}$ thin films as a function of exposure to OH and $O_2$ . . 89
4-10 Comparison of mass loss rate by $C_{36}H_{74}$ thin films as a function of $O_2$ concentration . . . . . 90
4-11 Mass loss by $C_{36}H_{74}$ thin films following OH exposure . . . . . 91
4-12 Volatilization of unoxidized alkane films at 1 Torr . . . . . 93
4-13 Comparison of OH production sources by mass loss measurements of $C_{36}H_{74}$ films . . . . . 94
4-14 CIMS detection of $OH^-$ and $NO_2^-$ with addition of NO . . . . . 95
4-15 Effect of increased $NO_x$ on OH-oxidation kinetics of $C_{36}H_{74}$ films . . . . . 96

4-16 Mass change of a $C_{36}H_{74}$ film upon exposure to OH in elevated $NO_x$ concentrations . . . . . 96
4-17 Mass change of a $C_{36}H_{74}$ film upon exposure to OH in elevated $NO_2$ . . . . 97
4-18 Proposed mechanism for heterogeneous OH-initiation oxidation of organic aerosol . . . . . 100
4-19 Time-dependent change in mass for $C_{24}H_{50}$, $C_{30}H_{62}$, and $C_{36}H_{74}$ upon exposure to OH . . . . . 103
4-20 Reactivity comparison of *n*-alkane films upon exposure to OH . . . . . 103
4-21 Mass loss comparison of alkane and dicarboxylic acids . . . . . 106
4-22 Mass loss by a methane soot film exposed to OH . . . . . 108

5-1 TEM grid area for hydration study by FTIR . . . . . 114
5-2 SEM images of aerosol samples collected during the 2006 MILAGRO campaign for study of their hygroscopic properties . . . . . 114
5-3 Deliquescence cycle of MCMA aerosol as measured by FTIR . . . . . 115
5-4 Relative humidity vs. water uptake by MCMA aerosol . . . . . 116
5-5 CIMS spectrum for $NO_2^-$ with $SF_6^-$ as parent ion and RH = 15% . . . . . 119
5-6 Mass change by $C_{36}H_{74}$ films by OH-exposure in dry and wet conditions . . 120
5-7 Water contact angle of an alkane thin film before and after OH-oxidation . 121

6-1 Physical and chemical aerosol processing leading to removal mechanisms for carbonaceous aerosols in the troposphere . . . . . 126

# List of Tables


2.1 Individual element concentrations in non-volatile $PM_{2.5}$ by PIXE, PESA, and STIM . . . . . 30

2.2 Element groups obtained from PMF . . . . . 31

2.3 Soil/dust aerosol composition during MCMA–2003 by element ratios . . . . 37

4.1 Rate constants for several atmospheric alkoxy radicals at 298K and 1 atm . 73

5.1 IR absorption bands for select inorganic and organic species . . . . . 115

5.2 Deliquescence RH for several atmospheric inorganic compounds . . . . . 117

# Chapter 1

# Introduction

Aerosols play important and complex roles in the atmosphere ranging from local to global in scale. They affect climate through direct and indirect effects, impair visibility, threaten human health, and act as sources and/or sinks for reactive atmospheric species through heterogeneous processes. The complexity of aerosol composition and lack of laboratory study regarding the physical and chemical mechansims involved in their atmospheric evoluation has led to considerable uncertainty in determining their lifetimes and overall impact on the environment, however (Forster et al., 2007). An understanding of the fundamental physical chemistry underlying these effects is critical to unraveling the role of atmospheric aerosols.

## 1.1 Definitions

A strict definition of "aerosol" refers to solid and/or liquid particles suspended in a gas. In atmospheric chemistry this term is commonly used to describe the particulate component only; "aerosol" and "particle" are used interchangably. They may be directly emitted (primary aerosol) or formed by gas-to-particle conversion (secondary aerosol). An abundance of surface-based biogenic and anthropogenic emissions results in the vast majority of mass residing in the troposphere, the lowermost layer of the atmosphere extending from the Earth's surface to approximately 10 km.

Urban air quality is under increasing scrutiny considering that more than half of the world's population is expected to live in urban locations by 2008 (UNFPA, 2007) with potentially serious consequences associated with growing industrialization and land use change.

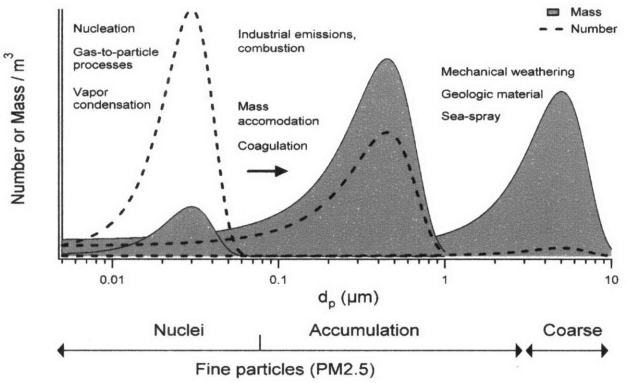


Figure 1-1: Typical atmospheric aerosol size distribution by mass (solid area) and number (dashed line).

The juxtaposition of high population densities and numerous particulate emission sources creates an immediate need to characterize the nature of urban aerosols. Epidemiological studies have shown that exposure to ambient particles is correlated with adverse respiratory and cardiovascular effects (Pope et al., 2002; Dockery et al., 1993; Ghio and Devlin, 2001), particularly smaller particles less than 2.5 $\mu$m in diameter ($PM_{2.5}$) which can penetrate the lungs more deeply. Both particulate concentration and chemical composition are understood to determine the overall toxicity.

### 1.1.1 Size distribution

Size and morphology of atmospheric particles have a direct influence on their physical and chemical properties. Urban aerosols generally follow a trimodal size distribution consisting of the nuclei ($d_p \leq 0.1$ $\mu$m), accumulation (0.1 $\mu$m $\leq d_p \leq$ 2.5 $\mu$m), and coarse modes ($d_p > 2.5$ $\mu$m) (Finlayson-Pitts and Pitts, 2000). "Fine particles" is the term used to describe total particulate matter $\leq 2.5$ $\mu$m in diameter ($PM_{2.5}$) while "coarse particles" in the most general sense refers to particulate matter $\leq 10$ $\mu$m in diameter ($PM_{10}$). Aerosol size distributions may be described by a log-normal function of the form:

$$\frac{dM}{d\log d_p} = \sum_i \frac{M_i}{\log \sigma_i \sqrt{2\pi}} exp\left(-\frac{(\log d_p - \log \bar{d_{pi}})^2}{2\log^2 \sigma_i}\right) \tag{1.1}$$

with mass concentration $M_i$ (or number, $N_i$), mean particle diameter $\bar{d_{pi}}$, and standard deviation $\sigma_i$ of the $i^{\text{th}}$ log-normal mode (Seinfeld and Pandis, 1998). Normalized size dis-

tributions of urban aerosol (Fig. 1-1) show that while mass is typically divided between accumulation and coarse modes, nuclei mode aerosols are more numerous. This high number density and fast Brownian diffusion for aerosols $< 0.1$ $\mu$m leads to fast coagulation rates and relatively short lifetimes due to rapid growth into the accumulation mode. Nuclei mode aerosols are mostly formed through homogeneous or heterogeneous nucleation, or by condensation of vapors produced from combustion processes. Accumulation mode aerosols enjoy longer residence times dictated for the most part by wet deposition removal, i.e., below-cloud or in-cloud scavenging. Coarse mode aerosols are formed through mechanical processes such as geological weathering and erosion; their greater mass results in efficient dry deposition through gravitational settling.

### 1.1.2 Carbonaceous aerosols

Research over the past several decades has revealed much about inorganic aerosols including sulfates, nitrates, and mineral dust, but far less information is available for carbonaceous compounds. Soot and organic particles make up a substantial fraction of all tropospheric aerosols, approximately 20 – 50% and as high as 90% in tropical forested locations (Kanakidou et al., 2005; McFiggans et al., 2005). Soot, also called "black carbon" (BC) from its absorptive properties, is a byproduct of incomplete combustion that is composed of both elemental and organic carbon. Soot particles are composed of individual spherules 20 – 30 nm in diameter aggregated together, giving rise to a large surface area (Seinfeld and Pandis, 1998). The exact chemical composition and morphology of soot particles depends upon conditions such as air-to-fuel ratio, temperature, and engine cycle (Chughtai et al., 2002; Burtscher et al., 1998). Spectroscopic and extraction analyses have shown that soot has both aliphatic and aromatic character, often with organic compounds including polycyclic aromatic hydrocarbons (PAHs) adsorbed on the surface (Akhter et al., 1985a,b; Zielinska et al., 2004).

Whereas soot comes solely from primary emissions, organic aerosols may be either primary (biomass burning emissions, unburned fuel and/or lubricating oils in vehicular exhaust, plant debris, seaspray containing dead organic matter) or secondary (gas-to-particle partioning or reactive uptake of volatile organic compounds (VOCs)). Detailed molecular speciation is challenging considering the large variety of alkane, alkene, carboxylic acid, aldehyde, ketone, and aromatic functional groups that may be present. Currently less than

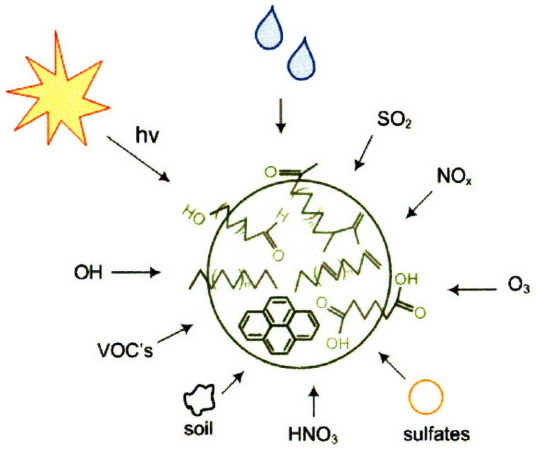


Figure 1-2: Schematic representation of carbonaceous aerosol processing.

about 20% of total atmospheric organic mass can be identified through chromatography and other analytical means (McFiggans et al., 2005; Rogge et al., 1993).

## 1.2 Atmospheric aerosol processing

Upon emission, aerosols may undergo extensive atmospheric *processing*, also known as *aging*, through interaction with radicals, gases, solar radiation, and other particles (Fig. 1-2). Physical processing includes condensation of low vapor pressure gas-phase species or coagulation with other particles, while chemical processing involves formation or breaking of bonds. Physical and chemical processing likely occur simultaneously depending upon the reactivity of the species of interest, availability of atmospheric reactants, and meteorological conditions. With sufficient residence time and/or reactivity, aerosols may become internally mixed, meaning that a single particle contains components derived from different sources, as opposed to externally mixed.

## 1.3 Heterogeneous reactivity

Aerosol reactivity is best expressed through a resistance model with individual terms describing gas–surface diffusion ($\Gamma_g$), uptake across the interface ($\alpha$), and liquid-phase solubility ($\Gamma_{sol}$) and reaction ($\Gamma_{rxn}$) (Finlayson-Pitts and Pitts, 2000):

$$\frac{1}{\gamma} = \frac{1}{\Gamma_g} + \frac{1}{\alpha} + \frac{1}{\Gamma_{rxn} + \Gamma_{sol}} \tag{1.2}$$

$$= \frac{\bar{c} d_p}{8 D_g} + \frac{1}{\alpha} + \frac{\bar{c}}{4 H R T \sqrt{D_{aq} k}} \tag{1.3}$$

where

$\gamma$ = net uptake coefficient

$\bar{c}$ = mean speed of gas-phase reactant = $\sqrt{8RT/\pi M}$

$D_g$ = gas-phase diffusion coefficient

$d_p$ = particle diameter

$\alpha$ = mass accommodation coefficient

$H$ = Henry's Law constant

$R$ = gas constant

$T$ = temperature

$D_{aq}$ = aqueous-phase diffusion coefficient

$k$ = first-order rate constant for aqueous-phase reaction

*Uptake* ($\gamma$) is defined as the probability that a gas-surface collision will result in reaction whereas *mass accommodation* ($\alpha$) is the probability that a gas molecule will enter into the bulk; therefore $\alpha$ is an upper limit to $\gamma$. A correction factor of 1/2 is required to account for distortion of the Boltzmann velocity distribution ($\bar{c}/4$) in cases of high uptake at the surface (Motz and Wise, 1960):

$$\frac{1}{\Gamma_g} = \frac{\bar{c} d_p}{8 D_g} - \frac{1}{2} \tag{1.4}$$

In this thesis, we will focus on the OH-reactivity of carbonaceous particles considering that OH is the most important and efficient oxidant in the atmosphere. As a result, reactions between OH and organics occur predominantly at or very near the surface, such that gas-to-surface diffusion is the parameter governing the reaction kinetics. When measured by means of a flow tube reactor, the uptake by a gas-phase molecule on a surface with observed rate, $k_{obs}$, depends on diffusion at a given pressure (P) to the surface from radius (r), and

the heterogeneous wall reaction:

$$\frac{1}{k_{\text{obs}}} = \frac{1}{k_{\text{diff}}} + \frac{1}{k_{\text{kin}}} = \left(\frac{r^2}{D_g}\right) P + \frac{1}{k_{\text{diff}}} \tag{1.5}$$

with uptake given by $k_{\text{kin}}$

$$\gamma = \frac{2rk_{\text{kin}}}{\bar{c} + rk_{\text{kin}}} \tag{1.6}$$

This approach has proven useful for investigating the heterogeneous kinetics for a large variety of atmospheric gases and inorganic/organic surfaces (Rudich, 2003, and references therein). While previous studies have largely favored detection of gas-phase reactants and products, fewer attempts have been made to directly probe the surface. Only recently have methods been developed to monitor a surface reaction as related to atmospheric processes in real time.

## 1.4 Hydrophobic vs. hydrophilic properties

The reaction between carbonaceous aerosols by OH or $O_3$ is especially important since initially hydrophobic C–C and C–H bonds may be oxidized to C–O functional groups (carboxylic acids, ketones, aldehydes, alcohols) to enhance possible water uptake and susceptibility for wet deposition removal (Rudich, 2003; Eliason et al., 2004; Petters et al., 2006). Similarly, the physical mixing with soluble organic or inorganic aerosols, or condensation of hygroscopic compounds is exptected to enhance the ability of carbonaceous compounds to attract and retain water (Shonija et al., 2007; Kotzick and Niessner, 1999). Studies have observed positive correlations between water uptake and the oxidation state of organic films (Demou et al., 2003), as well as the the amount of water-soluble compounds present (Facchini et al., 2000). Sufficiently hygroscopic aerosols may act as cloud condensation nuclei (CCN) (Shilling et al., 2007; Zuberi et al., 2005) thereby influencing cloud formation and precipitation through indirect climate effects (Facchini et al., 1999).

## 1.5 Considerations for field analysis vs. laboratory study

Atmospheric chemistry research generally falls within one of three major categories: (1) field measurements, (2) laboratory experimentation, or (3) modeling, where the latter two are intended to simulate atmospheric conditions. While the ideal would be to identify and

quantify all reactants, products, and chemical mechanisms with their reaction rates, the sheer number of interacting species makes this a formidable task beyond the capabilities of current analysis techniques. However, it is extremely useful to design laboratory experiments motivated by field observations. This allows for control over the number of variables and reaction conditions, and insures that the study is atmospherically-relevant. Laboratory conditions and detection constraints may require the use of artificially high reactant concentrations and/or accelerated time scales. Potential effects on the reaction mechanism or observed products must be taken into consideration when devising a research strategy in order to achieve meaningful results.

## 1.6 Thesis outline

The objective of this thesis is to contribute to the understanding of aerosol composition, physical nature and chemical reactivity through both field analysis and laboratory experimentation with particular focus on carbonaceous aerosols in urban environments.

We first discuss analysis of aerosol samples collected in the Mexico City Metropolitan Area (MCMA) during the MCMA–2003 Field Campaign, with additional select findings from the 2006 MILAGRO campaign. The speciated composition and emissions sources of $PM_{2.5}$, including information on the relative amounts of carbonaceous and inorganic compounds obtained through ion beam analysis techniques is presented in Chapter 2. In this section we report unique analysis of the organic component by comparing off-line and real-time techniques. Chapter 3 discusses detailed chemical and physical analysis of single particles through in-depth microscopy and X-ray analysis to gain insight into atmospheric processing of soot aerosols under urban conditions.

We then turn to laboratory investigation of chemical processing of carbonaceous aeosols, specifically the OH-initiated oxidation of carbonaceous thin films as aerosol surrogates. A new experimental apparatus was designed to monitor surface reactivity through mass change in carbonaceous films as a function of exposure to OH and $O_2$ concentrations. Experiments done in the presence and absence of $NO_x$ (= $NO_2$ + NO) were used to investigate effects relevant to urban vs. rural locations. Results are discussed within the context of a proposed heterogeneous oxidation mechanism in Chapter 4, and the effect of oxidation on water uptake ability and hydrophilic properties of the oxidized films is presented in Chapter 5.

We summarize conclusions and offer recommendations for future research in Chapters 6 and 7, respectively.

# Chapter 2

# Chemical composition and sources of urban aerosols

## 2.1 Mexico City Metropolitan Area

The Mexico City Metropolitan Area (MCMA) is both a complex and valuable environment for atmospheric chemistry research. A unique combination of geographic and socioeconomic factors has resulted in severe air pollution in Mexico City, which is further fueled by rapid population growth. The MCMA is located at a semitropical latitude enclosed in an elevated basin (2240 m above sea level) with mountains to the east, west and south (Fig. 2-1). More than 20 million people live within the basin encompassing 5000 $km^2$ total area (1500 $km^2$ urban area). The large majority of gaseous and particulate pollutants emitted in the MCMA are anthropogenic in nature, related to mobile sources, power generation, and other industrial activities. A fleet of over 3 million motor vehicles including older-model taxis and microbus "colectivos" poorly equipped for emissions control contribute to hazardous levels of criteria pollutants $NO_x$, ozone ($O_3$), particulate matter (PM), and volatile organic compounds (VOCs) (Molina and Molina, 2002). Official inventories have been compiled for gas-phase emissions (CAM, 2004) but such information for particulate emissions remains preliminary.

The MCMA–2003 Field Campaign was a collaborative study that took place throughout the month of April, 2003 with the participation of more than 30 academic and governmental institutions from the U.S., Mexico and Europe (Molina et al., 2007). The primary objective

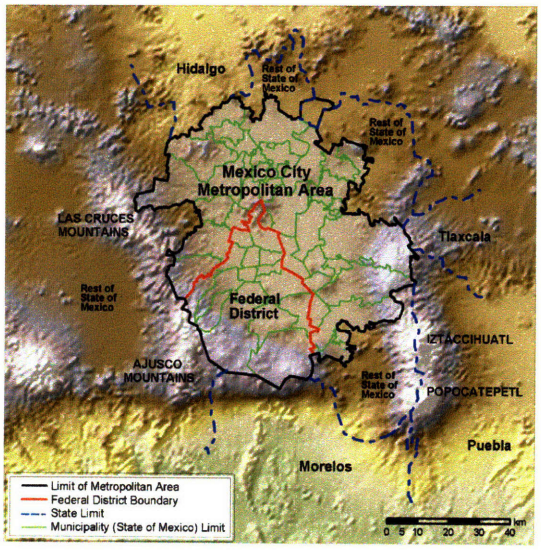


Figure 2-1: Topographical map of the Mexico City Metropolitan Area (Molina and Molina, 2002).

to analyze the chemical composition, reactivity, and dispersion of atmospheric constituents was accomplished through a comprehensive network of gas-phase, aerosol and meteorological measurements. A subsequent goal of the campaign was to provide the scientific basis for implementation of effective pollution control strategies, as well to serve as a case study for other megacities and urban environments.

A major focus of the MCMA–2003 campaign was characterization of the composition, emissions sources and formation mechanisms of atmospheric PM. The public health risks associated with PM inhalation create an immediate need for quantitative and detailed compositional information. Heavy metals are particularly important considering their toxicity for human health (Campen et al., 2001; Florea and Büsselberg, 2006; Chapman et al., 1997) as well as potential role in an array of heterogeneous reactions involving soot and organic compounds (Jung et al., 2003; Kim et al., 2005; Chughtai et al., 1993).

## 2.2 PIXE, PESA, STIM analysis techniques

Particle-Induced X-ray Emission (PIXE) is a highly sensitive and efficient means of deconvoluting the complex chemical composition of atmospheric aerosols. It consists of nondestructive irradiation of a sample with energetic particles, often protons, causing emission of

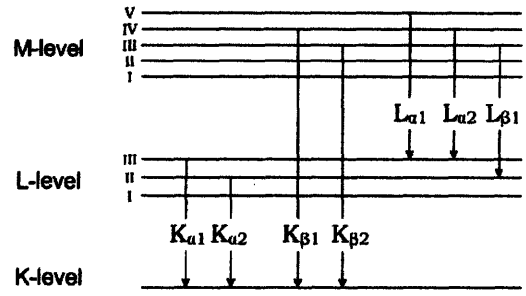


Figure 2-2: Typical energy levels and X-ray emission lines.

X-rays characteristic of the elements present ($Z \geq$ Na) (Fig. 2-2) (Johansson et al., 1995). Because detection levels for heavy metals are typically on the order of several ng/m$^3$, PIXE is well-suited to quantification of trace elements associated with anthropogenic emissions present in atmospheric aerosols. Several disadvantages to the PIXE technique must be considered, namely the loss of volatile compounds under vacuum during analysis and inability to determine the chemical form of individual elements. For these reasons, supplementary data from other techniques including ion chromatography (IC) (Malm et al., 1994) and Aerosol Mass Spectrometry (AMS) (see Sec. 2.6.2) are both useful and necessary for complete mass speciation. Other accelerator-based ion beam analysis techniques can provide complimentary information such as Proton Elastic Scattering Analysis (PESA) for hydrogen, and Scanning Transmission Ion Microscopy (STIM) for total mass concentrations (Bench et al., 2002; Shutthanandan et al., 2002). PESA is a forward scattering technique in which the H spectrum is distinguished from other light elements (C, N, O) by placing the detector at an appropriate angle, while STIM measures energy loss from the incident ion beam as it passes through the sample.

## 2.3 Experimental

Samples of size-segregated $PM_{2.5}$ were collected at the ground-based MCMA–2003 campaign "supersite" located at the Centro Nacional de Investigación y Capacitación Ambiental (CENICA) within the Universidad Autónoma Metropolitana (UAM) in southeastern MCMA. This mixed commercial–residential area contains several local industries and roads within a 1 to 2 km radius, and lies approximately 10 km south of downtown Mexico City.

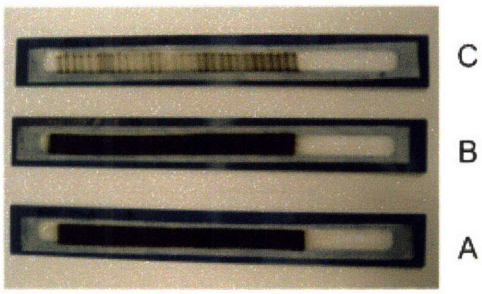


Figure 2-3: $PM_{2.5}$ samples collected by DRUM impactor onto Teflon strips in size ranges Stage A (1.15–2.5 $\mu$m), Stage B (0.34–1.15 $\mu$m), Stage C (0.07–0.34 $\mu$m).

Aerosol samples were collected continuously from April 3$^{rd}$ to May 4$^{th}$ onto Teflon substrates using a 3-stage IMPROVE DRUM impactor at a fixed flow of 10 SLPM with a rotation rate of 2 mm per 12 hours with the following size cuts: 1.15–2.5 $\mu$m (Stage A), 0.34–1.15 $\mu$m (Stage B) and 0.07–0.34 $\mu$m (Stage C).

PIXE, PESA, and STIM analyses were done within several weeks following the MCMA–2003 campaign at the Environmental Molecular Sciences Laboratory (EMSL) located at Pacific Northwest National Laboratory (PNNL). Experimental procedures were similar to those described in Shutthanandan et al. (2002). The Teflon substrates were carefully removed from the impactor, mounted on plastic strips (Fig. 2-3), and placed in a computer-controlled sample holder inside a vacuum chamber maintained at approximately $2{\cdot}10^{-7}$ Torr. A 3.5 MeV proton beam was used for PIXE and PESA (performed simultaneously) while a 0.75 MeV beam was used for STIM analysis. The experimental setup is shown in Figure 2-4. PIXE spectra were evaluated by the GUPIX program and concentrations of elements Na to Pb were determined by calibration to known standards. Elements were fit by their principal spectral lines except for Pb in which $L_\alpha$ (10.225 eV) was used due to S interference with $M_\alpha$ ($K_\alpha$(S) = 2.306 eV; $M_\alpha$(Pb) = 2.342 eV). Re-analysis showed that Pb concentrations were below detection level, although it should be noted that the relative intensity of $L_\alpha$ is about a factor of 10 lower than $M_\alpha$. Hydrogen concentrations were determined from PESA spectra with reference to Mylar ($C_{10}H_8O_4$) films of known thickness. Total aerosol mass collected on the substrates was determined from STIM spectra calibrated by several known standards.

Positive Matrix Factorization (PMF) was applied to PIXE and PESA data to identify possible emissions sources by temporal correlations among co-emitted elements. PMF is

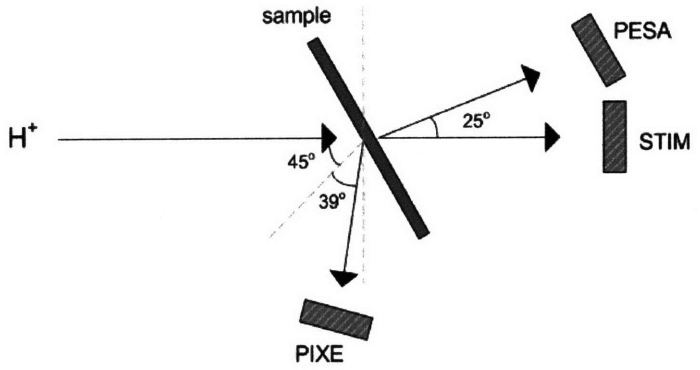


Figure 2-4: Experimental setup for PIXE, PESA, and STIM analysis.

preferable to other multivariate analysis methods such as cluster analysis (CA) and principle component analysis (PCA) for the ability to impose non-negative constraints given a set of specified criteria (Paatero and Tapper, 1994). The quality of the variables in our study was determined by both the number of below detection limit values and the signal-to-noise ratio. The number of PMF factors was determined by trial and error based on the interpretability of the resolved factors, the robustness of the objective functions, and the relative changes in the objective functions with the change of the number of factors (Johnson et al., 2006). For these studies, the proton accelerator was operated by Dr. V. Shutthanandan and the PMF analysis was done by Dr. YuLong Xie.

## 2.4 Results on $PM_{2.5}$ composition and sources

Element concentrations from PIXE analysis (Na, Mg, Al, Si, P, S, Cl, K, Ca, Ti, V, Mn, Fe, Ni, Cu, Zn, As, Br, Sn), hydrogen concentrations from PESA, and total mass from STIM are summarized in Table 2.1. The statistical error and detection limits derived from the PIXE spectrum fitting procedure were used in PMF analysis; median error values are shown in Table 2.1. Fit errors for major elements (S, Si, K) were about 5% while most other elements ranged from 10% to 50%. The overall uncertainty in mass calibration was 5% based on standards provided by MicroMatter (Deer Harbor, WA, USA).

The majority of $PM_{2.5}$ mass was contained in Stage B (50%) followed by Stage A (35%) and Stage C (15%). Among PIXE-measured elements, S was the highest in concentration surpassed only by Si in Stage C. Other major elements included Al, Fe, Mg, and K. PMF analysis of PIXE and PESA data identified 8 factors in Stage A, 7 in Stage B and 4 in Stage

Table 2.1: Individual element concentrations in Stages A, B, and C by PIXE, PESA, and STIM analysis. Average values that were below detection level are indicated by * and maximum concentrations for these elements appear in parentheses.

| | Stage A 1.15–2.5 $\mu$m | | | | Stage B 0.34–1.15 $\mu$m | | | | Stage C 0.07–0.34 $\mu$m | | | |
|---|---|---|---|---|---|---|---|---|---|---|---|---|
| | ave | max | min | error | ave | max | min | error | ave | max | min | error |
| (ng/m$^3$) | | | | | | | | | | | | |
| Na | 9.5 | 69.5 | 0 | 30% | 11.2 | 77.2 | 0 | 26% | 17.2 | 45.7 | 4.4 | 14% |
| Mg | * | (12.7) | 0 | 41% | 6.3 | 13.9 | 0 | 29% | 14.9 | 36.7 | 4.2 | 12% |
| Al | 25.9 | 77.5 | 5.1 | 8% | 40.5 | 109.7 | 0 | 6% | 73.7 | 188.1 | 13.4 | 3% |
| Si | 117.4 | 339.5 | 52.0 | 3% | 130.6 | 311.8 | 20.5 | 2% | 225.2 | 606.4 | 48.4 | 2% |
| P | 5.7 | 21.8 | 0 | 36% | 8.7 | 30.5 | 0 | 29% | * | (12.6) | 0 | 38% |
| S | 688.0 | 1551.6 | 292.7 | 1% | 957.6 | 1926.7 | 344.5 | 1% | 98.5 | 313.7 | 14.3 | 3% |
| Cl | 19.6 | 56.6 | 4.1 | 18% | 28.7 | 73.8 | 7.2 | 14% | 8.6 | 27.1 | 0 | 19% |
| K | 108.5 | 252.0 | 28.5 | 3% | 135.0 | 339.6 | 27.0 | 2% | 30.7 | 78.3 | 6.0 | 6% |
| Ca | 25.4 | 63.2 | 7.6 | 7% | 51.7 | 104.2 | 12.3 | 4% | 92.2 | 257.3 | 22.0 | 2% |
| Ti | 3.1 | 19.0 | 0 | 23% | 6.2 | 28.3 | 2.2 | 14% | 8.3 | 33.1 | 0 | 9% |
| V | 3.6 | 82.5 | 0 | 26% | 4.1 | 64.1 | 0 | 21% | * | (18.1) | 0 | 62% |
| Mn | * | (5.4) | 0 | 37% | 3.0 | 23.0 | 0 | 20% | 1.3 | 10.3 | 0 | 28% |
| Fe | 29.0 | 72.8 | 14.1 | 4% | 63.2 | 196.9 | 31.2 | 2% | 80.3 | 251.7 | 16.4 | 2% |
| Ni | * | (14.2) | 0 | 50% | * | (12.8) | 0 | 41% | * | (4.3) | 0 | 54% |
| Cu | 5.9 | 37.3 | 0 | 14% | 15.1 | 117.9 | 2.1 | 9% | 10.0 | 68.5 | 0 | 11% |
| Zn | 19.8 | 162.8 | 3.8 | 7% | 34.6 | 341.2 | 8.5 | 6% | 13.7 | 82.0 | 2.7 | 9% |
| As | * | (13.1) | 0 | 36% | 3.0 | 19.0 | 0 | 31% | * | (4.1) | 0 | 58% |
| Br | * | (11.3) | 0 | 42% | 3.2 | 32.9 | 0 | 36% | * | (2.8) | 0 | 37% |
| Sn | 28.3 | 91.8 | 0 | 31% | 43.8 | 97.9 | 0 | 23% | 13.3 | 49.4 | 0 | 35% |
| PESA H (ng/m$^3$) | 980.0 | 2405.4 | 165.7 | 5% | 506.6 | 1404.2 | 147.3 | 5% | 66.9 | 197.9 | 21.6 | 5% |
| STIM ($\mu$g/m$^3$) | 7.05 | 16.96 | 0.68 | 5% | 9.89 | 21.72 | 0.29 | 5% | 3.10 | 7.16 | 1.47 | 5% |

C (Figure 2-5) identified by the representative elements, the explained variation matrix and the shape of the source contribution and source composition profiles. Following is a brief description of each emission type.

### 2.4.1 Sulfate

Single particle analysis and AMS data confirm that sulfur was a major component of $PM_{2.5}$ present as ammonium sulfate during the majority of the campaign (see Sec. 3.3.3) (Johnson et al., 2006; Salcedo et al., 2006). The relatively high minimum of sulfur (0.826 $\mu$g/m$^3$) indicates a consistent background concentration of particulate sulfate. Aqueous phase S(IV) to S(VI) oxidation tends to dominate under tropospheric conditions with a positive dependence on relative humidity (RH), $O_3$, and hydrogen peroxide ($H_2O_2$) (Finlayson-Pitts and Pitts, 2000). A lack of correlation with the gas-phase $H_2SO_4$ production rate calculated from OH and $SO_2$ concentrations measured during the campaign suggest a heterogeneous mechanism (Salcedo et al., 2006).

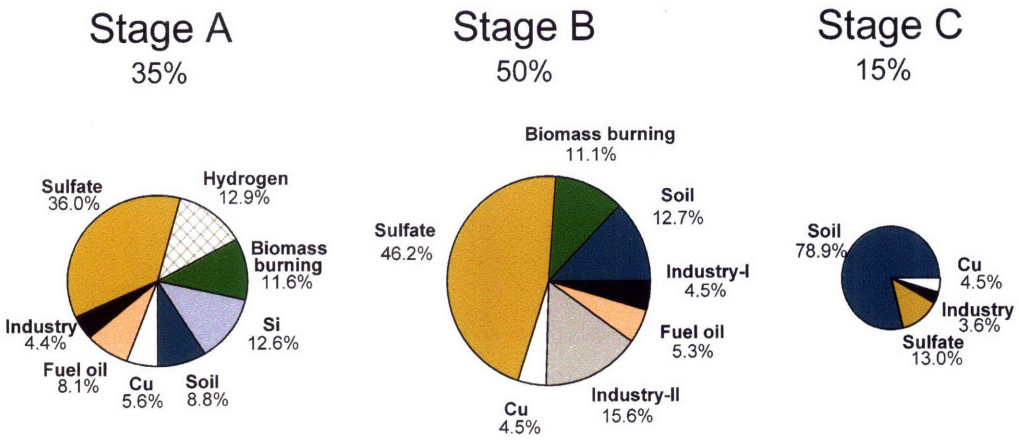


Figure 2-5: Emission source categories by Positive Matrix Factorization (PMF).

Table 2.2: Elements groups obtained from PMF.

| Factor | Source Description | Elements |
|---|---|---|
| **Stage A: F1** | Sulfates | S (P, Pb) |
| F2 | Soil | Mg, Al, Si, Ca, Ti, Mn, Fe |
| F3 | 2$^{rd}$ Si | Si (S, K, Mn, Zn) |
| F4 | Biomass burning | K, Cl, Br, Sn |
| F5 | Hydrogen | H, Cl, Sn |
| F6 | Industry | Zn (As, Mn, Na) |
| F7 | Fuel oil | V, Ni |
| F8 | Cu | Cu (As) |
| **Stage B: F1** | Sulfates | S (Pb) |
| F2 | Soil | Na, Mg, Al, Si, Ca, Ti, Mn, Fe, Sn |
| F3 | Biomass burning | K, Cl, H, Br |
| F4 | Industry–I | Zn (As, Mn, Na) |
| F5 | Industry–II | Mn, Zn, S, H |
| F6 | Fuel oil | V, Ni |
| F7 | Cu | Cu (As) |
| **Stage C: F1** | Sulfates-fuel oil | S, V, Ni |
| F2 | Soil | Mg, Al, Si, Ca, Ti, Mn, Fe |
| F3 | Industry | Zn, Mn |
| F4 | Cu | Cu |

$SO_2$ emissions in Mexico City originate from both anthropogenic and volcanic sources. The influence of the Popocatepetl volcano, located 60 km southeast of Mexico City (see Fig. 2-1) on sulfate aerosol production has been addressed (Moya et al., 2003; Raga et al., 1999), but the role of anthropogenic $SO_2$ and effects of sulfur-containing fuel in mobile source emissions remain unclear.

### 2.4.2 Industry

Heavy metals in atmospheric aerosols point to industrial emission sources. Copper comprises a separate factor in each size range (Fig. 2-5), perhaps signifying a particular sector such as smelting. Other factors identified by Zn, Mn, Na, and As may be a mix of various industrial processes; the two separate factors in Stage B have been labeled "Industry I" and "II" for lack of specific information on the activities involved. Zn has previously been traced to tire and brake wear (Smolders and DeGryse, 2002; Lin et al., 2005); vehicle debris mixed in dust may explain Si factor in Stage A which was weakly associated with Zn, Mn, and Fe.

These industrial factors reflect sporadic events rather than consistent patterns. Two such emissions events were apparent during MCMA–2003, on April $9^{th}$ and $10^{th}$, both occurring overnight to early morning. Figure 2-6 shows a sharp increase in Na, Mn, As and Zn concentrations on the $9^{th}$ clearly distinguishable above low background levels. To ascertain the likely direction of this plume, we performed simulations of particle back-trajectories as described by de Foy et al. (2006) and shown in Johnson et al. (2006). The paths for particle tracers show that the air masses during this time came from the north/northeast, consistent with the fact that many industries are located within the northern zone of Mexico City.

A similar sharp increase in V and Ni, known components of fuel oil, occurred on April $10^{th}$ (Fig. 2-7) also coinciding with a large $SO_2$ plume (97.6 ppb maximum) measured independently by researchers at the CENICA air quality monitoring station. Particle back-trajectory simulations confirm a north/northwest source direction with paths over the location of Tula, a major oil refinery located approximately 80 km north of CENICA. The ratio V/Ni = 5.25 determined from our data is comparable to that found in a U.S. study tracing the metals directly to power plant emissions (Kowalczyk et al., 1982). This finding underscores the importance of anthropogenic $SO_2$ emissions in the MCMA, and hence on sulfate aerosol formation.

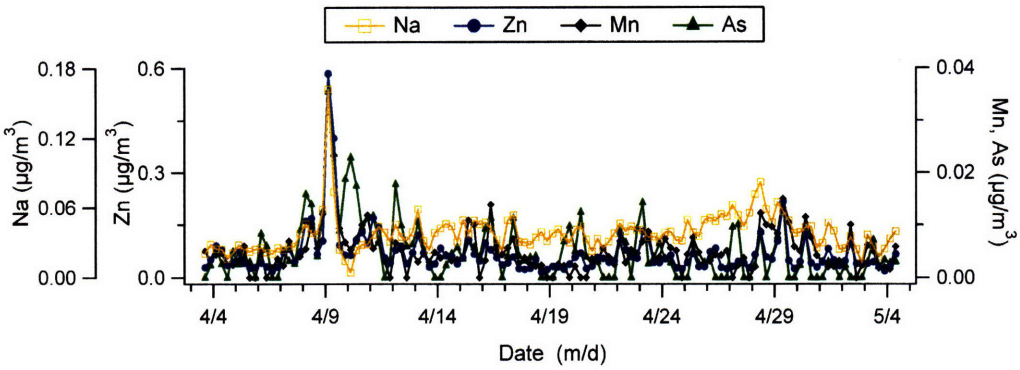


Figure 2-6: Time series of elemental markers for industrial emissions (Na, Zn, Mn, As) during MCMA–2003 showing an April $9^{th}$ emissions event.

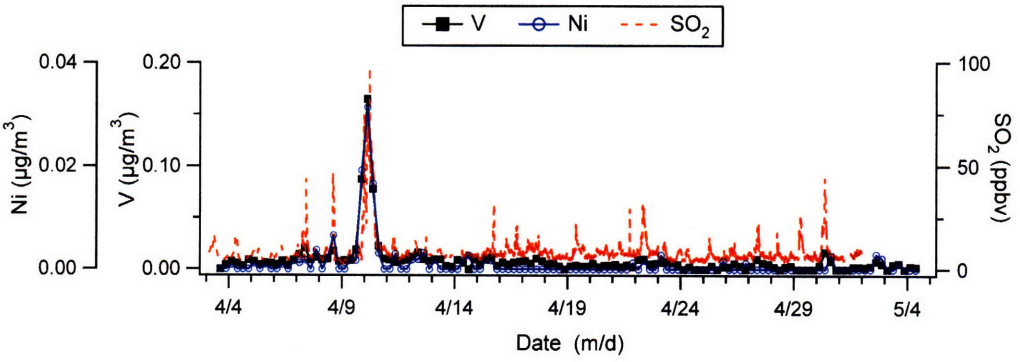


Figure 2-7: Time series of fuel oil components V, Ni shown with $SO_2$ measured at CENICA during MCMA–2003 showing a sharp increase on April $10^{th}$.

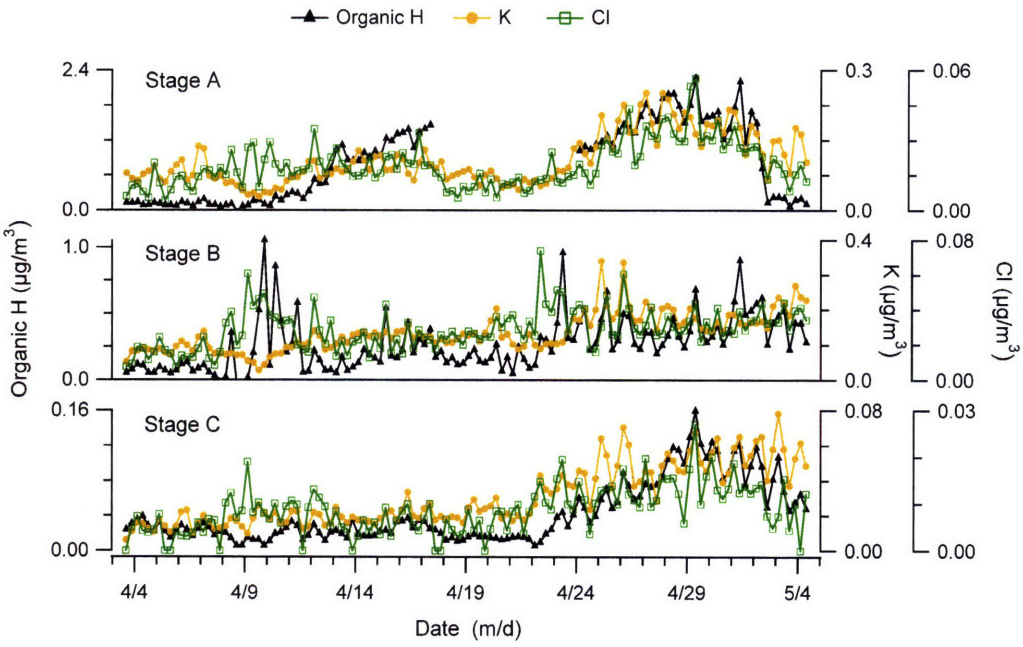


Figure 2-8: Elemental markers of biomass burning K, Cl, organic H during MCMA–2003. A portion of hydrogen data is missing in Stage A because minor damage to the substrate caused partial distortion of PESA spectra.

### 2.4.3 Biomass burning

Factors composed of elements K, Cl, Sn, Br, and H indicate biomass burning where H is an indicator for organic compounds (Malm et al., 1994; Miranda et al., 1996). Potassium salts, such as KCl, are commonly found in particulate emissions from burning vegetation (Li et al., 2003). The time series for K, Cl, and organic H appear in Figure 2-8 where organic H has been calculated as the quantity in excess of that associated with $(NH_4)_2SO_4$ (see Sec. 2.6.3) assuming loss of volatile compounds in the vacuum chamber during analysis. A portion of hydrogen data is missing in Stage A because minor damage to the substrate caused partial distortion of PESA spectra.

Wildfire emissions in, and immediately surrounding the MCMA basin have been correlated with $PM_{10}$ concentrations (Bravo et al., 2002); our data more specifically suggest that regional fires are a major source of $PM_{2.5}$ in Mexico City. Trajectories based on MODIS (Moderate Resolution Imaging Spectroradiometer) fire detection products (Justice et al., 2002) in Mexico during the time of the campaign show that the number of fires increased noticeably after April 22$^{nd}$ with decreased RH, and coincident with higher concentrations

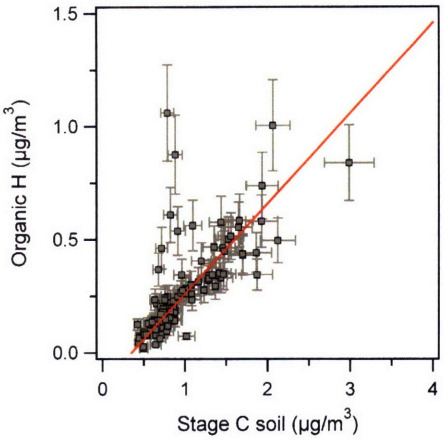


Figure 2-9: Stage C soil/dust particle mass calculated from PIXE metal oxides vs. organic H. A linear fit of y = (0.33 ± 0.03)x - 0.11 ± 0.02; $\chi^2$ = 64.3 assumes 10% and 50% errors for PIXE and PESA, respectively.

of K and Cl.

A strong correlation between biomass burning markers and soil-related elements in Stage C (0.07-0.34 $\mu$m) was observed. A linear fit of y = (0.33 ± 0.03)x - 0.11 ± 0.02; $\chi^2$ = 64.3 was determined according to the procedure given by Press (1992) assuming 10% and 50% errors for PIXE and PESA, respectively. These two particle types most likely shared a common source direction where dry conditions associated with the fires facilitated resuspension and transport of fine dust (Gaudichet et al., 1995). Note that the correlation between organic H and soil-related elements eliminates ambiguity introduced by the fact that K is a component of both smoke and soil.

### 2.4.4 Soil/dust

A soil/dust factor represented by common earth elements was identified in each size category. Figure 2-10 shows that the concentrations of Si, Ca, Al, Fe, Mg, and Ti clearly track one another throughout the campaign. Soil/dust particles followed a diurnal pattern with the highest concentrations in the morning when winds were typically calm and mixing heights were low (de Foy et al., 2005). An anti-correlation between fine soil particles and wind speed was observed and may be explained through dilution effects.

Overall increases in concentrations of soil-related elements from April 15$^{th}$ to 18$^{th}$, and after April 23$^{rd}$ were observed during periods of decreased RH. From the 15$^{th}$ to the 18$^{th}$,

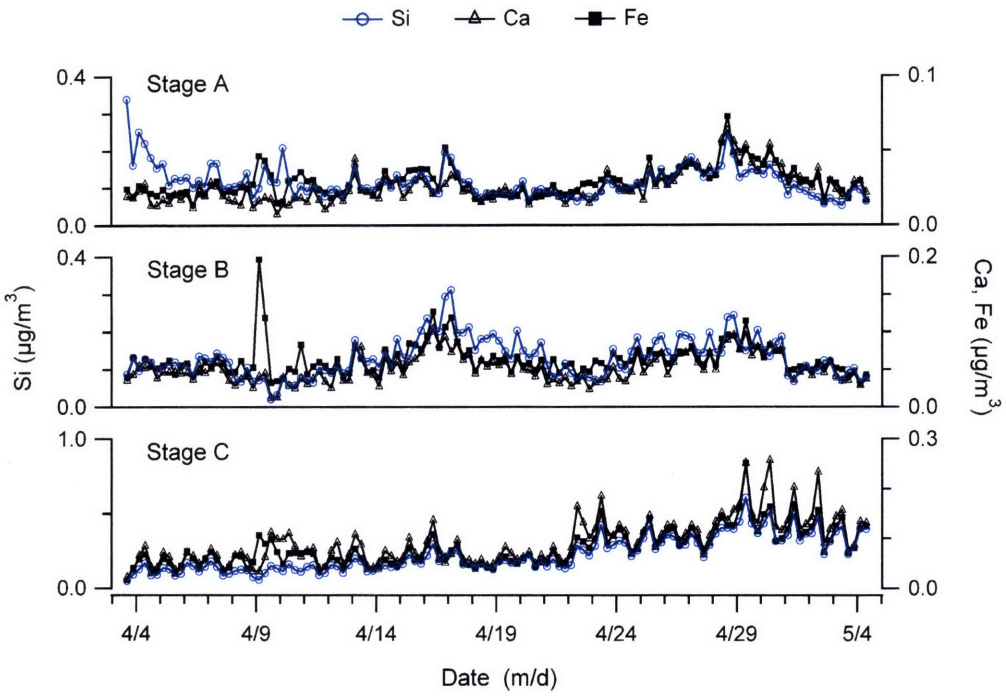


Figure 2-10: Time series of soil-related elements for Stages A, B, and C during MCMA–2003.

the average daily temperature measured at CENICA rose from 20.1 °C to 23.5 °C while the average RH dropped from 52.1% to 19.4%. Increased concentrations in Stage C particles (0.07–0.34 $\mu$m) after the 23$^{rd}$ suggest longer range transport from outside the basin facilitated by the aforementioned dry conditions accompanying fires burning within the region.

The total concentration of soil/dust mass in $PM_{2.5}$ may be estimated from individual element concentrations by accounting for their common oxides such as $SiO_2$, $Al_2O_3$, and $Fe_2O_3$ (Malm et al., 1994):

$$[\text{Soil}] = 2.20[\text{Al}] + 2.49[\text{Si}] + 1.63[\text{Ca}] + 2.42[\text{Fe}] + 1.94[\text{Ti}] \tag{2.1}$$

The resulting concentrations were: Stage A = 0.47 $\mu$g/m$^3$, Stage B = 0.66 $\mu$g/m$^3$, and Stage C = 1.08 $\mu$g/m$^3$. While soil comprised 6.6% of Stage A (with reference to STIM total mass) and 6.7% of Stage B, it contributed more than one-third (35.0%) of the Stage C mass. The composition of dust/soil particles in our samples was similar to paved, unpaved roads and/or tezontle soil based on a Mexico City fugitive dust emissions study done by

Table 2.3: Comparison of soil/dust aerosol composition in $PM_{2.5}$ during MCMA–2003 with results from a fugitive dust emissions study by Vega et al. (2001).

| | MCMA–2003 | Paved road | Unpaved road | Tezontle soil |
|---|---|---|---|---|
| Fe/Si | 0.365 | 0.231 | 0.219 | 0.345 |
| Ca/Si | 0.358 | 0.295 | 0.534 | 0.363 |
| Na/Si | 0.080 | 0.008 | 0.123 | 0.041 |
| Al/Si | 0.296 | 0.306 | 0.288 | 0.460 |
| K/Si | 0.579 | 0.058 | 0.067 | 0.058 |

Vega et al. (2001). Table 2.3 lists the element ratios obtained from PIXE for comparison. Higher K concentrations measured during MCMA–2003 are consistent with a contribution from biomass burning sources. Our results indicate an availability of fine particulate soil to become mixed with other aerosols, both organic and inorganic.

### 2.4.5 STIM and non-volatile $PM_{2.5}$ speciation

Considering the loss of volatile aerosol mass under vacuum during analysis, STIM mass may be apportioned to sulfates, soil, heavy metals, soot, and non-volatile organics. Although carbon was not directly detected in our study, we infer that about 50% of non-volatile $PM_{2.5}$ was carbonaceous, including both organic and black carbon, upon accounting for the contribution of inorganics directly measured via PIXE. Figure 2-11 shows the contribution for each component by mass, in qualitative agreement with total $PM_{2.5}$ speciation by Salcedo et al. (2006) using a combination of AMS, aethelometer, Tapered Element Oscillating Microbalance (TEOM), and PIXE data. They reported that nearly two-thirds of $PM_{2.5}$ during MCMA–2003 was carbonaceous (organics = 54.6%, black carbon = 11.0%), followed by sulfate (10.3%), nitrate (10.0%), soil (6.9%) and chloride (0.8%).

## 2.5 Discussion within context of other studies on MCMA particulate emissions

Variability in season, meteorology, and pollutant emissions complicate comparison among different field studies, yet it is useful to highlight several trends to improve our understanding of the spatial and temporal variability of Mexico City particulate matter. Our data are best compared to other PIXE and X-ray Fluorescence (XRF) studies (Miranda et al., 1992, 1994, 1996, 2004; Chow et al., 2002; Díaz et al., 2002; Aldape et al., 2005) which also pertain to

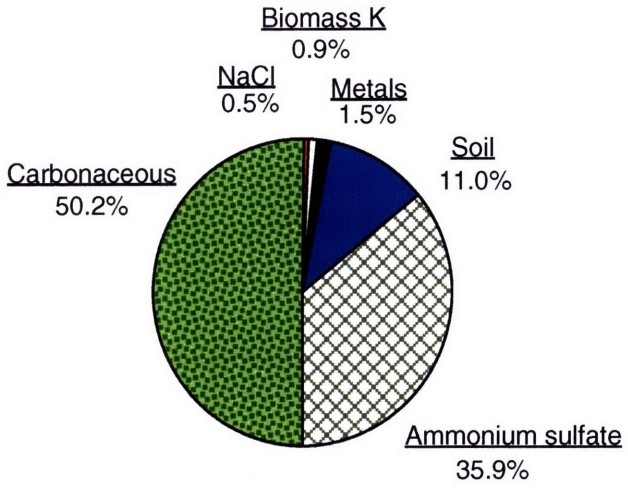


Figure 2-11: Speciation of non-volatile $PM_{2.5}$ into its major components via PIXE, PESA, and STIM.

non-volatile species. Among these works, several (Miranda et al., 1994, 1996, 2004; Díaz et al., 2002; Aldape et al., 2005) applied multivariate analysis and identified similar source categories, including sulfate aerosols and industrial plumes. Biomass burning emissions were either not discussed or only briefly mentioned, perhaps due to the fact that the common marker elements, K and Cl, have multiple sources. Our unique opportunity to correlate these elements with PESA hydrogen measurements enabled identification of a separate category in spite of the fact that organics and soil are likely both related to wildfire emissions.

Mobile source emissions are underestimated by this approach to source apportionment since soot and organic aerosols associated with traffic emissions are not directly detected by PIXE, PESA, or XRF. Miranda et al. (1996) identified a factor related to traffic emissions through Pb and Br, but levels of these gasoline additives have generally declined over time since leaded fuel was discontinued in Mexico City in 1997. Vega et al. (1997) employed a comprehensive chemical mass balance (CMB) receptor model including PIXE data, elemental and organic carbon (EC and OC), sulfates, and nitrates and reported that vehicle emissions were responsible for over 40% of $PM_{2.5}$, although it should be noted that samples were collected near major roadways. Recent advances enable real-time anlaysis of mobile source emissions in vehicle "chase" studies, also employed during MCMA–2003 (Jiang et al.,

2005; Kolb et al., 2004). Our single particle analysis (see Ch. 3) confirms that vehicle exhaust was dominated by soot and organics, a fraction of which was likely traced via PESA hydrogen.

As implied by our data and reported by others (Miranda et al., 1994, 2004), concentrations of heavy metals are generally higher towards the northern section of the city. We have found additional support during the 2006 MILAGRO campaign (Megacity Initiative: Local and Global Research Observations), a large-scale field study modeled after, and expanding upon the results of MCMA–2003. Three different sampling sites were chosen to investigate pollution generated within the city and the regional and long-range transport of pollutants from the MCMA basin:

- T0, the main supersite located at the Instituto Mexicano del Petroleo (IMP) in downtown (northern) Mexico City;
- T1, the northern boundary side located at the Universidad Tecnológica de Tecámac in the State of Mexico;
- T2, located approximately 35 km northeast of the T1 site at Rancho Bisnaga, north of Tizayuca in the State of Hidalgo.

Samples of $PM_{2.5}$ were collected at all three sites for PIXE, PESA, and STIM analysis in the same manner described previously (see Sec. 2.3). Figure 2-12 shows the time series for Zn and Cu at the T0 site in northern Mexico City. The metals followed a diurnal trend with maximum concentrations observed between midnight and 6 am. These concentrations were consistently higher than measured previously at the southeastern CENICA site during MCMA–2003.

Microscopy studies were performed on select aerosol samples coinciding with these overnight peak concentrations (see Sec. 3.2 for single particle analysis procedures). We found a high density of soot particles mixed with intricate, needlelike Zn particles whose X-ray spectra showed to be ZnO (Johnson et al., 2007a). Figure 2-13 shows two images of a sample collected over an average of 15 minutes at $\sim$ 1:30 am on March 23$^{rd}$, 2006. The left-hand image was taken in secondary electron (SE) mode to obtain high resolution for particle morphology, whereas the right-hand image shows the same area in backscattered electron mode (BSE) to clearly distinguish heavy metals from lighter elements. The sample collection was done in such a way to avoid artificial particle overlap (Laskin et al., 2003),

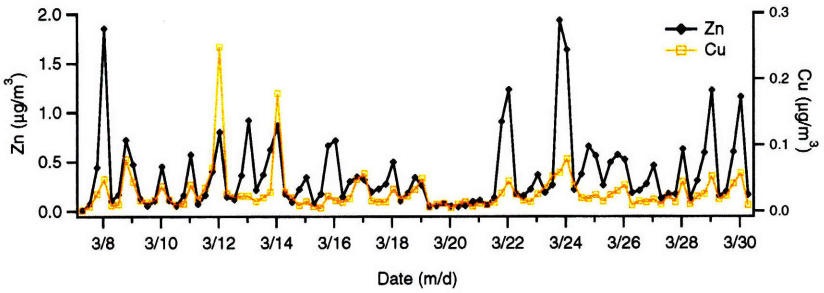


Figure 2-12: Time series of Zn and Cu in $PM_{2.5}$ (sum of Stages A, B, C) collected at the IMP site in northern Mexico City during the 2006 MILAGRO Field Campaign.

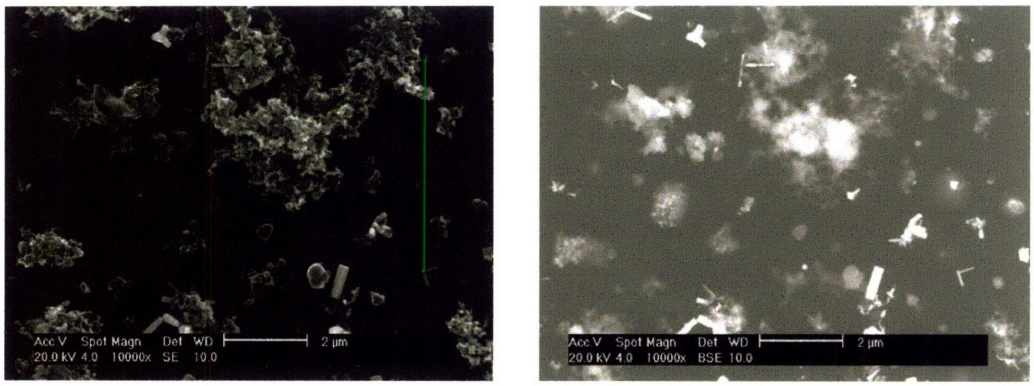


Figure 2-13: Microscopy images of particles collected at the IMP site during the MILAGRO campaign (March 23$^{rd}$, $\sim$ 1:30 am). Left: secondary electron (SE) mode showing fractal soot mixed with needle-like ZnO particles, Right: backscattered electron (BSE) mode emphasizing metals whose heavier mass results in brighter areas within the image.

showing that overnight industrial activities provide an important, likely underreported, particulate emissions source. These observations are complimentary to a Pb–Zn particle type identified by an Aerosol Time-of Flight Mass Spectrometer (ATOF-MS) collocated at the IMP site during MILAGRO (Moffet et al., 2007).

## 2.6 Comparison with Aerosol Mass Spectrometry

Advances in analytical instrumentation have enabled real-time measurement of atmospheric aerosols in addition to traditional filter-based measurements. The Aerodyne Aerosol Mass Spectrometer (AMS) provides size and compositional information on submicron, non-refractory aerosols at a time resolution of 2 to 3 minutes (Jayne et al., 2000; Jimenez et al., 2003). The AMS operates by drawing atmospheric aerosols into a series of vacuum chambers for

size determination by time-of-flight or chemical composition analysis. A collection of particles is typically vaporized into molecular fragments which are charged by electron impact (EI) for detection by quadrupole mass spectrometry. The identity of atmospheric compounds is determined with reference to a database of mass spectra compiled by NIST (i.e., http://webbook.nist.gov/chemistry/) and mass concentrations are calculated by calibration against laboratory standards.

The collocation of the DRUM impactor and an AMS operated by the Jimenez research group (University of Colorado–Boulder) during MCMA–2003 provided the unique opportunity for intercomparisons (Johnson et al., 2007c). PIXE/PESA and AMS employ fundamentally different methods of atmsopheric aerosol analysis yet the data obtained are remarkably complimentary; PIXE's sensitivity to high Z elements and inability to measure volatile compounds is inversely mirrored by AMS detection of only non-refractory aerosols that vaporize at temperatures $\leq$ 600 °C. Several direct, quantitative data comparisons are useful for gaining insight into Mexico City aerosol chemistry as well as evaluation of off-line vs. real-time detection techniques.

### 2.6.1 Aerosol collection

The AMS reports 100% collection efficiency for particles 60 to 600 nm in diameter with partial transmission up to 1.5 $\mu$m; the total size range is approximated as $PM_1$ (Salcedo et al., 2006). Particle shape and density are important parameters that affect AMS collection efficiency; the following expression relates vacuum aerodynamic diameter, $d_{va}$ (relevant in the free molecular regime used in AMS detection), with aerodynamic diameter, $d_a$ (applicable to the DRUM impactor):

$$d_{va} = d_a \sqrt{\frac{\rho_p}{\chi \rho_o}} \tag{2.2}$$

where $\rho_p$ is the density, $\rho_o = 1$ g/cm$^3$ is the standard density, and $\chi$ is a "shape factor", $\chi = 1$ for a perfect sphere and $\chi > 1$ for irregular particles such as soot aggregates (DeCarlo et al., 2004; Jayne et al., 2000). Assuming $\rho_p = 1.75$ g/cm$^3$ for spherical sulfate particles (Salcedo et al., 2006) effectively converts the AMS size range to 55 nm $\leq d_a \leq$ 756 nm. This simplified approximation does not take into account the fact that particles in Mexico City tend to be irregular in shape and internally-mixed (see Ch. 3). Given the most comparable size range from PIXE analysis 0.07 nm $\leq d_p \leq$ 1.15 $\mu$m (sum of Stages B and C), a

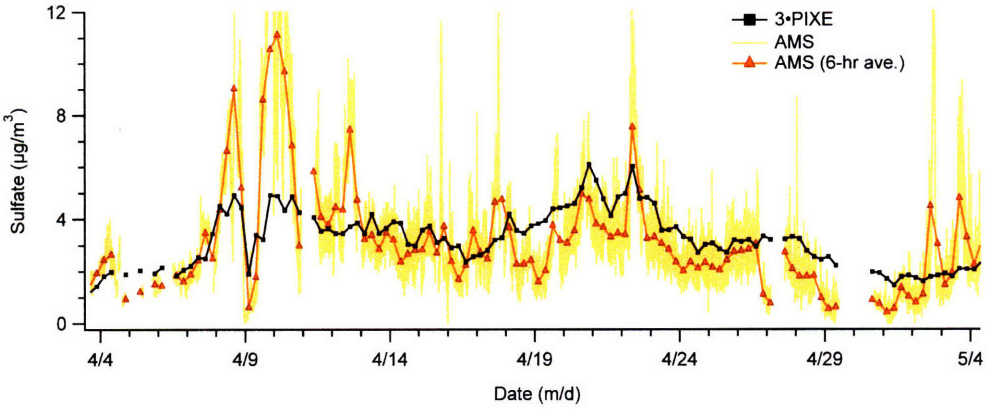


Figure 2-14: Time series for $SO_4{}^{-2}$ measured by PIXE and AMS.

systematic difference in measured mass is expected.

### 2.6.2 PIXE sulfur and AMS sulfate

Particulate sulfur was readily detected by both PIXE (elemental S) and AMS ($SO_4{}^{-2}$). The following expression was used to determine the PIXE sulfate mass, assuming all sulfur was present as $SO_4{}^{-2}$:

$$[SO_4{}^{-2}]_{\mathrm{PIXE}} = 3 \cdot [S]_{\mathrm{PIXE}} \tag{2.3}$$

The time series comparison (Fig. 2-14) shows agreement in the overall concentration trends during MCMA–2003. The PIXE concentrations are systematically higher as expected from the difference in particle collection size range. A clear discrepancy extending from April $8^{\mathrm{th}}$ to $12^{\mathrm{th}}$ is evident where AMS measurements are up to a factor of 2 higher; possible explanations for this are explored below. Momentarily excluding this period gives the x–y correlation shown in the left-hand plot of Figure 2-15 biased towards PIXE values with y = (0.87 ± 0.03)x by least-squares linear regression, $R^2$ = 0.62. The "missing" aerosol mass between the DRUM and AMS collections may be estimated by integrating the size distribution function for mass (Eq. 1.1) from 750 nm – 1.15 $\mu$m given the appropriate parameters for sulfate aerosols: $M_{SO_4}$ = 2.8 $\mu$g/m$^3$, $d_p$ = 345 nm ($d_{va}$ = 457 nm), and $\sigma$ = 1.7 (Salcedo et al., 2006). With this correction ($\sim$ 0.5 $\mu$g/m$^3$), the relationship approaches 1:1 as shown in the right-hand plot of Figure 2-15.

In constrast to the majority of the campaign where aerosols were neutralized by an abundance of $NH_3$, aerosols during April $8^{\mathrm{th}}$ to $12^{\mathrm{th}}$ were acidic. An ion balance of AMS

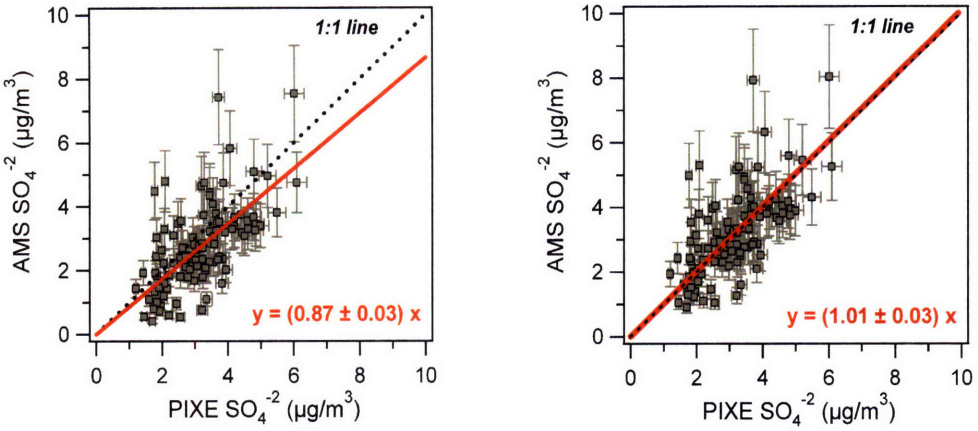


Figure 2-15: PIXE vs. AMS measurement of $SO_4^{-2}$ during MCMA–2003 (left) without correction, and (right) after accounting for size difference due to aerosol collection. Data from April 8 – 12$^{th}$ are excluded. Error bars represent 20% and 5% in AMS and PIXE, respectively.

data shows that the measured $NH_4^+$ was lower than the amount required to fully neutralize sulfate ($(NH_4)_2SO_4$), nitrate ($NH_4NO_3$) and chloride ($NH_4Cl$) (Salcedo et al., 2006). Because sulfuric acid has a low vapor pressure ($P_{H_2SO_4} = 2.2{\cdot}10^{-5}$ Torr) (Richardson et al., 1986), it readily partitions to the aerosol phase where the preferred form is solid or aqueous $(NH_4)_2SO_4$:

$$H_2SO_4 + NH_3 \rightarrow (NH_4)HSO_4 \tag{2.4}$$

$$H_2SO_4 + 2NH_3 \rightarrow (NH_4)_2SO_4 \tag{2.5}$$

In case of insufficient gas-phase $NH_3$ the aerosol remains acidic as ammonium bisulfate ($NH_4HSO_4$), driving nitrate ($P_{HNO_3} = 8$ Torr) into the gas phase. Recalling Sec. 2.4.2, this "acidic period" coincides with pronounced industrial emissions including the maximum $SO_2$ concentration of the campaign. The relative humidity (RH) during this period was also relatively high with overnight RH levels reaching up to 90%, which would be expected to enhance the sulfate production rate. An overnight thermal inversion may have prevented mixing between sulfate produced from $SO_2$ industrial emissions aloft and $NH_3$, whose sources are typically related to agriculture and/or automotive emissions, probably remaining close to the ground.

Although aerosol acidity appears the most likely explanation for the large differences in

concentrations apparent in Figure 2-14, several explanations are possible. From the perspective of PIXE detection, a heterogeneous reaction between the aerosol sample surface with $SO_2$ could have caused a mass artifact considering that a denuder was not used to remove reactive gases from our sampling line prior to aerosol collection. This type of interaction would most likely have increased, rather than decreased, the amount of sulfur detected by PIXE, however. Eldred and Cahill (1997) found no evidence to support an artifact due to $SO_2$ in absence of a denuder. A more plausible explanation might be associated with the reduced pressure and/or ion beam conditions during analysis. Richter et al. (1984), following work by Hansen et al. (1980), studied thermal decomposition of $H_2SO_4$, $NH_4HSO_4$, and $(NH_4)_2SO_4$ as a function of proton beam current density, substrate, and pressure. They found that a beam current $> 150$ nA/cm$^2$ led to losses up to $\sim 50\%$ with minor losses due to pressure over the range $4{\cdot}10^{-4}$ Torr to $7.5{\cdot}10^{-2}$ Torr. Thicker substrates (5 mg/cm$^2$ vs. 1 mg/cm$^2$) were shown to promote localized heating from exposure to the beam, leading to greater sample loss. Our analysis was done with 0.2 nA/cm$^2$ of current and Teflon filters $\sim 0.6$ mg/cm$^2$ thick such that these type of effects should have been minimal. The high aerosol density in Mexico City and collected in our samples may have caused unforeseen effects, however.

From the AMS perspective, field measurements have shown that both particle acidity and higher RH conditions result in a higher collection efficiency (CE), while dry particles, and those with irregular morphologies may "bounce" after impacting the vaporizer, effectively lowering the CE (Kleinman et al., 2007). Taking into consideration the meteorological conditions during MCMA–2003, a CE of 0.5 was assumed for the AMS with uncertainty of $-30\%$, $+10\%$ in mass concentration (Salcedo et al., 2006). It is possible that rapidly changing conditions, and the unique character of the aerosols during this particular time may have affected the CE beyond these estimates.

There is currently no evidence for significant concentrations of organosulfate or metal sulfate compounds during MCMA–2003, but we cannot rule out the possibility. The former may have evaporated under vacuum prior to PIXE analysis while the latter could have escaped AMS detection if they were not vaporized. A targeted study featuring side-by-side AMS and DRUM collection of laboratory-generated aerosols composed of various sulfate and other sulfur-containing compounds would be helpful to survey and assess their comparability for detection.

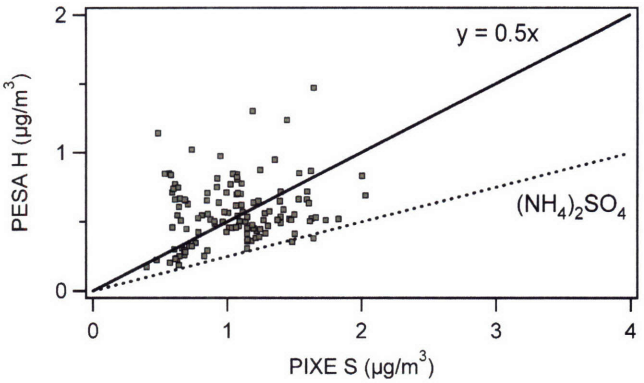


Figure 2-16: PIXE sulfur vs. PESA hydrogen for Stages B + C (0.07 $\mu$m $\leq$ $d_p$ $\leq$ 1.15 $\mu$m).

### 2.6.3 PESA hydrogen and AMS organics

Hydrogen mass obtained by PESA was apportioned to $(NH_4)_2SO_4$ and organic compounds considering loss of water and nitrates under vacuum, and in absence of any other major sources of hydrogen. Mass fractions of "organic H" and "sulfate H" were calculated from PESA and PIXE data as follows:

$$\begin{aligned} [\text{Organic H}] &= [\text{H}_{\text{Total}}] - [\text{Sulfate H}] \\ [\text{Organic H}] &= [\text{H}_{\text{Total}}] - 0.25[\text{S}] \end{aligned} \tag{2.6}$$

Each component contributes about 50% (0.25 $\mu g/m^3$) of the total hydrogen in Stages B + C, also evident from a plot of PIXE sulfur vs. PESA hydrogen (Fig. 2-16).

The organic H component exhibits a strong diurnal trend, as opposed to sulfate, with peaks during the late morning to early afternoon likely related to both anthropogenic emissions and photochemical reactivity. Figure 2-17 shows the time series for organic H and sulfate H with AMS organics for comparison; a correction has been made in the hydrogen apportionment during the aforementioned "acidic period" to account for the presence of $NH_4HSO_4$.

Good agreement between organic H and AMS organics validates our assumptions of source apportionment and indicates that a significant fraction of organic aerosols were retained under vacuum for PESA analysis. The correlation between the two is described by a linear fit y = (36.92 $\pm$ 2.77)x + 6.06 $\pm$ 0.49; $\chi^2$ = 120 assuming 20% error for AMS and 50% for PESA to account for higher uncertainty related to due to partial losses under

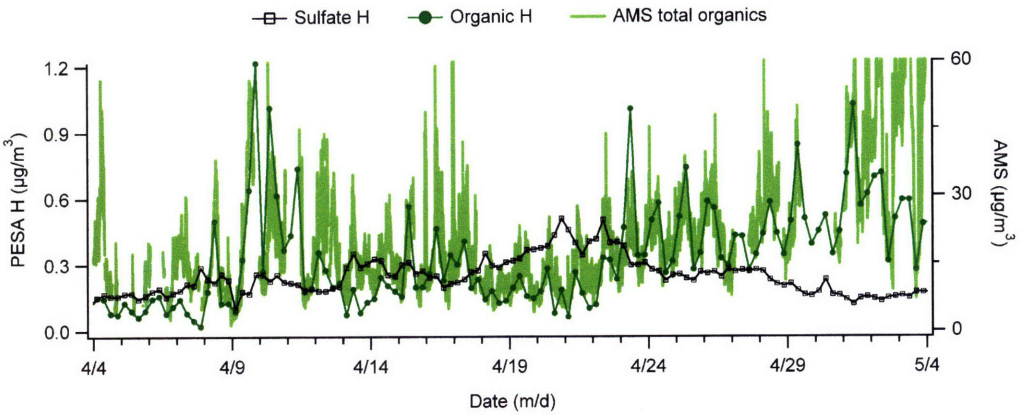


Figure 2-17: MCMA–2003 time series for PESA organic H and sulfate H, and AMS total organic aerosol mass.

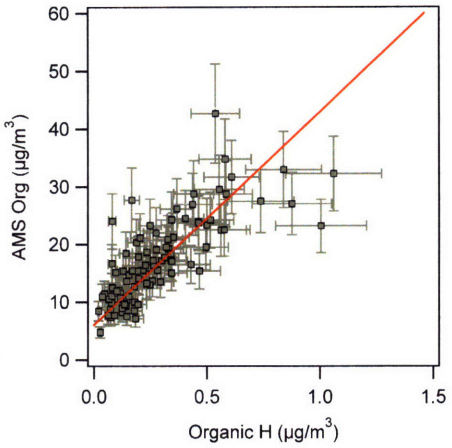


Figure 2-18: PESA organic H vs. AMS total organics; y = (36.92 ± 2.77)x + 6.06 ± 0.49; $\chi^2 = 120$ assuming 20% error in both coordinates.

vacuum (Fig. 2-18). The consistent offset $\sim 6$ $\mu g/m^3$ likely reflects this loss of more-volatile material.

The AMS data have been further analyzed by multivariate analysis for more in-depth interpretation of complex organic spectra. Zhang et al. (2005a) found that a linear combination of two components accurately describe the total organic mass: a hydrocarbon-like organic aerosol (HOA) related to primary emissions traced by m/z 57 ($C_4H_9^+$), and oxygenated organic aerosol (OOA) exhibiting greater C–O functionality and traced by m/z 44 ($CO^+$). The OOA component has been recently divided into two subclasses (OOA-I and OOA-II), and a fourth type related to biomass burning (BBOA) has been distinguished

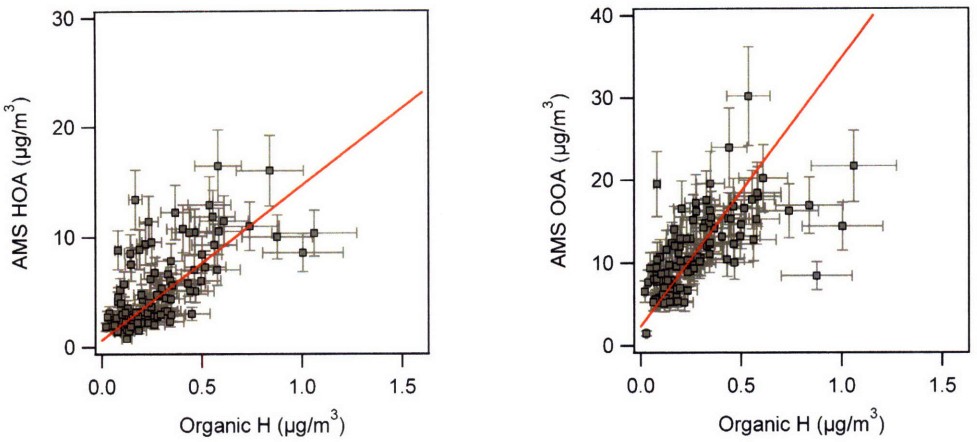


Figure 2-19: Correlation between PESA organic H and AMS organic aerosol components: Hydrocarbon-like (HOA): y = (14.05 ± 0.96)x + 0.65 ± 0.13, $\chi$ = 313; oxygenated (OOA): y = (32.54 ± 2.03)x + 2.35 ± 0.28; $\chi$ = 214; 20% errors were assumed in both coordinates.

(J. Jimenez, personal communication). The correlations between PESA organic H and AMS organics HOA and OOA appear in Figure 2-19 showing better agreement with OOA than HOA. Although HOA contains more hydrogen, oxidized compounds may have heavier molecular weights and hence lower vapor pressures for better retention under vacuum.

The concentration of non-volatile organic mass in Mexico City can be extracted from organic H provided that the average hydrogen content in organic mass is known or otherwise can be estimated. We have applied results from Zhang et al. (2005b) reporting the average HOA composition of C:H = 1:1.9 and OOA as C:H:O = 1:1.6:0.8. Considering that HOA and OOA comprised 1/3 and 2/3, respectively, of total organics during MCMA–2003 (Salcedo et al., 2006), the average hydrogen was 8.6%. Figure 2-20 compares two methods of obtaining organic mass from PESA data: the first by AMS correlation (Fig. 2-18), and the second by a direct scaling by a factor of 100/8.6% = 11.6[Organic H] as shown by Malm et al. (1994). Poor agreement in case of the latter emphasizes the fact that organics encompass a range of vapor pressures in Mexico City.

Although PIXE has been used extensively in atmospheric aerosol measurement, few researchers have adopted PESA hydrogen as a marker for organic compounds. The most prominant example, however, is the IMPROVE network (Interagency Monitoring of Protected Visual Environments) which uses PESA hydrogen measurements to quantify organic mass as part of a comprehensive approach to chemical speciation of $PM_{2.5}$ and $PM_{10}$ in

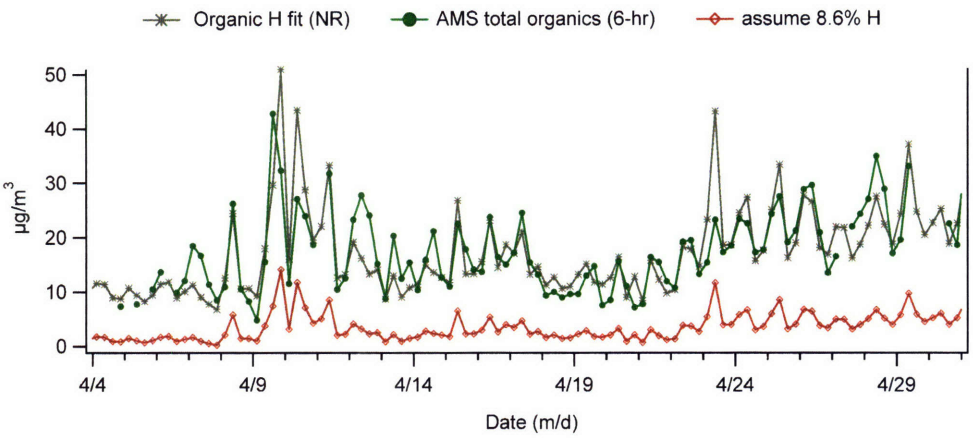


Figure 2-20: Total organic aerosol mass obtained via PESA organic H.

U.S. national parks (UC-Davis, 1995). They compare PESA data – obtained under vacuum for samples collected on nylon filters – with independent measurements of organic carbon mass by thermal optical reflectance (TOR) – done at atmospheric pressure for aerosol samples collected on quartz filters. TOR is an analytical method by which aerosol samples are heated in successive increments to measure the evolved carbon; initially in a He atmosphere to measure the organic carbon, followed by a $He/O_2$ mixture at higher temperatures to detect the elemental carbon as $CO_2$. The IMPROVE data analysis procedure involves multiplying PESA hydrogen concentrations by a factor of $\sim$11 to determine total organic mass, corresponding to an average 9% hydrogen content (empirical formula $C_9H_5O_2$). This method has shown favorable agreement even though no allowances are made for sample losses at reduced pressure employed during PESA (Malm et al., 1994). Organic aerosol concentrations measured in these remote U.S. parks range from 1 to 5 $\mu g/m^3$, or one-tenth that measured in Mexico City during MCMA–2003 ($> 20$ $\mu g/m^3$). Organic aerosols present in forested national parks are likely composed of compounds with a large degree of atmospheric processing due to long residence times. In contrast, urban environments undoubtedly contain a wide variety of fresh and aged emissions, which explains why a simple scaling of PESA is not valid in our case. Figure 2-20 clearly illustrates this difference on the order of 10 $\mu g/m^3$. The fitting function determined by comparison with AMS data provides much better agreement, and provides an estimate for the fraction of organics retained under vacuum. Non-volatile organics comprised roughly 25% of the total organic mass, extracted from the slope of the linear fit obtained in Figure 2-18 and assuming 8.6% average hydrogen

content as follows from AMS organic aerosol components HOA and OOA.

This is the first comparison of PIXE/PESA (off-line) and AMS (real-time) analysis of atmospheric aerosols; to our knowledge also the first reported application of PESA hydrogen organic aerosol measurement within an urban environment. Organics characterized by a low vapor pressure, high molecular weight would be consistent with the presence of humic acid compounds (Zappoli et al., 1999), oligomers (Samburova et al., 2005; Kalberer et al., 2004), biomass burning emissions (Reid et al., 2005; Gao et al., 2003), and/or extended C−O functionality. Chemical processing of organics via OH or $O_3$ oxidation could increase molecular mass by formation of carbon-oxygen functional groups which could in turn lower the vapor pressure.

The chemical reactions involved in chemical processing of aerosols are not yet widely understood. Oxidation of organic aerosol has been shown to both raise and lower the vapor pressure of a reacting compound. In studies on the potential for diesel exhaust emissions to form secondary organic aerosol (SOA), Robinson et al. (2007) assumed that OH-initated oxidation reduced the volatility of gas-phase organics by one order of magnitude. They concluded that low-volatile gas-phase species ("intermediate-volatility organic compounds", IVOC) were more efficient than VOCs in secondary organic aerosol (SOA) production through photochemical processing. However, Molina et al. (2004) found that OH-initated oxidation of organic films as atmospheric aerosol proxies led to net volatilization from the surface via C−C bond scission. The effect of oxidation on the fate of organic compounds is of considerable interest and will be further explored in Chapter 4.

# Chapter 3

# Atmospheric processing of soot

## 3.1 Introduction

Soot particles are ubiquitous in the troposphere as primary components of vehicular exhaust and industrial emissions concentrated in urban areas, and of biomass burning plumes in remote areas (Reid et al., 2005). Bond et al. (2004) estimates the total global burden of black carbon (BC) or soot at 8.0 TgC/year with contributions of 4.6 TgC/yr from fossil fuel combustion and 3.3 TgC/yr from open biomass burning. Long-range transport of soot has been documented (Sharma et al., 2004; Novakov et al., 2000), provoking questions regarding the length of the particles' atmospheric lifetimes, the extent to which atmospheric processing influences their physico-chemical properties, and their local/regional/global effects on the environment.

The microphysical structure and chemical composition of soot has been the subject of considerable research and debate over the past several decades. It is generally understood that individual carbon spherules 20 – 30 nm in diameter are formed from polycyclic aromatic hydrocarbon (PAH) precursors during the initial stages of combustion. These basic units further aggregate into the irregular fractal particles $d_p = 0.1 - 1$ $\mu$m which are observed in the atmosphere (Fig. 3-1). This unique structure has been described as "onion-like" with both aromatic and aliphatic functionality. A three-dimensional structure proposed by Akhter et al. (1991) based upon detailed spectroscopic analysis of hexane soot is shown in Figure 3-2. Numerous studies have identified organic gases and semi-volatile compounds adsorbed to the surface during the cool-down phase following combustion (Burtscher et al., 1998; Zielinska et al., 2004; Kittelson et al., 2005; Akhter et al., 1985b).

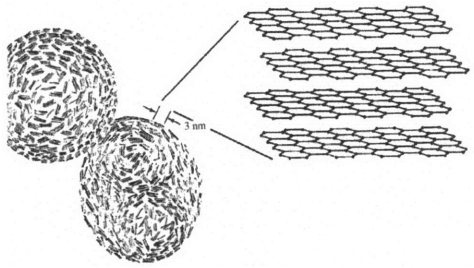


Figure 3-1: Soot microstructure (Seinfeld and Pandis, 1998).

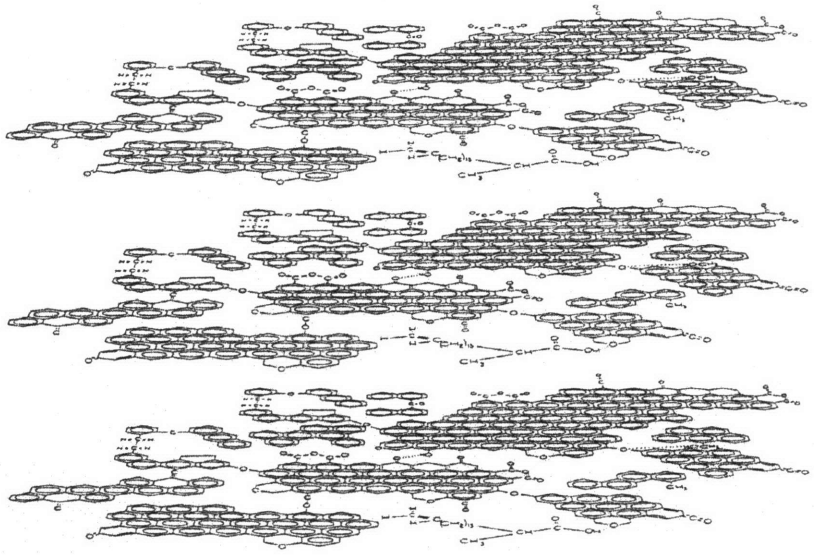

Figure 3-2: Three-dimensional structure of soot proposed by Akhter et al. (1991).

Whereas freshly-emitted soot is typically hydrophobic, it may become more hydrophilic over the course of physical and chemical atmospheric processing. Numerous studies have investigated heterogeneous reactions on a soot surface in a simulated polluted environment (Chughtai et al., 1993; Ammann et al., 1998; Aubin and Abbatt, 2003; Kamm et al., 1999). Oxidation by gaseous OH, $O_3$, and $NO_x$ has shown to cause formation of polar surface groups that can attract and retain water (Decesari et al., 2002; Chughtai et al., 1999; Zuberi et al., 2005). Soot particles may also become more hydrophilic through coalescence with, or condensation of, soluble inorganic or organic compounds such as sulfates, nitrates, and organic acids (Schnaiter et al., 2003; Kotzick and Niessner, 1999).

Soot plays an exceptionally complex role in climate. In the direct effect, it strongly absorbs solar radiation thereby exerting a positive radiative forcing ($0.25 \pm 0.08$ W/m$^2$) in the same way as greenhouse gases such as carbon dioxide, $CO_2$ ($1.66 \pm 0.17$ W/m$^2$), methane, $CH_4$ ($0.48 \pm 0.05$ W/m$^2$), and nitrous oxide, $N_2O$ ($0.16 \pm 0.02$ W/m$^2$) (Forster et al., 2007). The relatively long lifetimes ($\sim$100 yrs) of these gases lead to substantial, globally-averaged warming related to their long-term accumulation. The climate effects of soot occur on more localized spatial scales with a net forcing dependent upon specific morphological and chemical characteristics of the particles. The mixing state of soot particles significantly impacts their optical properties; an internal mixture consisting of a soot core coated by an aqueous sulfate layer is projected to amplify forcing by 50% compared to externally-mixed soot due to the greater refractive index provided by the shell (Jacobson, 2000). In addition to its direct effects, soot plays an important, indirect role by modifying the microphysical properties associated with the formation and lifetime of clouds. The surface area and availability of heterogeneous reaction sites provided by soot can lead to a higher number of smaller cloud droplets, and reduced rainfall. Soot may also cause a localized warming that reduces the relative humidity, destabilizes the troposphere, and inhibits cloud formation (Ackerman et al., 2000).

Despite an immediate need to better quantify the lifetime of soot in the atmosphere, the manner and extent to which particles react and become mixed with other atmospheric aerosols remains ill-defined. Estimates for the atmospheric lifetime of BC or soot depend on the hydrophobic to hydrophilic time-scales that are assumed (Chung and Seinfeld, 2002; Cooke and Wilson, 1996; Barth and Church, 1995; Liousse et al., 1996). For instance, a sensitivity analysis for BC hydrophilicity done by Cooke and Wilson (1996) showed a range

of 6 to 10 days. Furthering our understanding the nature of mixed soot particles, including their physical, chemical and optical properties is essential in determining the role of soot in the atmosphere.

## 3.2 Experimental

Methods of electron microscopy are effective and direct tools for studying composition and morphology of atmospheric particles. Scanning Electron Microscopy (SEM) and Transmission Electron Microscopy (TEM) with X-ray analysis provide detailed information on the nature of individual particles while Computer-Controlled Scanning Electron Microscopy with Energy Dispersed analysis of X-rays (CCSEM/EDX) provides a wealth of information on thousands of particles.

For single particle microscopy studies, the Time Resolved Aerosol Collector (TRAC) is a simple and efficient means of collecting and cataloguing atmospheric samples in a time-resolved fashion (Laskin et al., 2003). The TRAC is a conventional one stage jet-to-plate impactor which deposits aerosols on filmed TEM grids prearranged on an impaction plate (Fig. 3-3). The specially designed arrangement of the filmed grids in the impaction plate provides their tight contact with the plate surface.

Two TRAC devices were used to collect samples during MCMA–2003, the first installed at the CENICA supersite and a second placed on board the Aerodyne Mobile Laboratory (AML). Particle collections at CENICA were made continuously during the campaign whereas the AML sampled at specific times and locations within the MCMA as part of in-city vehicular emissions characterization experiments. Aerosol inlet flows for both TRAC instruments were maintained at approximately 0.8 L/min with sampling intervals of 15 and 5 minutes for CENICA and the AML, respectively. Particles were dried to 20% relative humidity at CENICA prior to collection. The sample substrates were Cu 400 mesh TEM grids covered with thin Carbon Type-B films (Ted Pella, Inc., Redding, CA). During collection, each sample grid was continuously advanced in order to prevent collected particles from artificial overlap. After the run, plates with the collected aerosol samples were sealed for storage. Particle samples were analyzed at the Environmental Molecular Sciences Laboratory (EMSL) located at Pacific Northwest National Laboratory (PNNL) immediately following the campaign. A FEI XL30 digital field emission gun Environmental Scanning

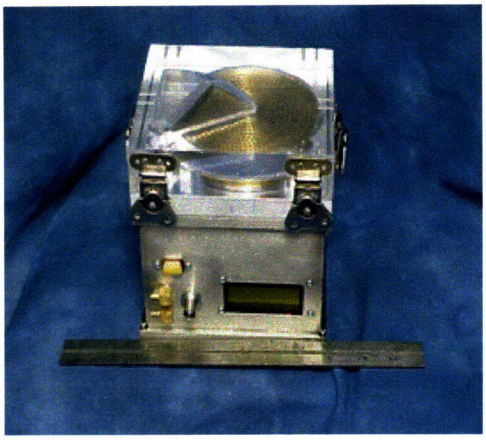

Figure 3-3: Time Resolved Aerosol Collector (TRAC). Aerosols are impacted onto Cu-supported grid substrates as the impactor plate advances continuously below the sampling inlet. The grids may then be directly used in single particle microscopy analyses.

Electron Microscope equipped with EDX microanalysis spectrometer (EDAX, Inc.) were used for CCSEM/EDX and SEM/EDX analysis (Laskin et al., 2003). TEM studies utilized a high resolution JEOL JEF 2010F microscope operating at 200 keV. The images were recorded digitally with a slow scan charge-coupled device (CCD) camera. Time-of-Flight Secondary Ion Mass Spectrometry (TOF-SIMS) analysis was done with a Physical Electronics TRIFT II instrument for an sample area measuring 50 $\mu$m x 50 $\mu$m was sputtered using a 60 pA DC beam for 120 seconds (for a total dose of $2{\cdot}10^{15}$ ions/cm$^2$).

Three sampling sites were chosen in an effort to characterize samples at different stages of atmospheric processing:

- **Fresh city traffic particulate emissions.** Vehicle exhaust plumes in the city center were directly sampled in order to capture freshly-emitted particles with minimal atmospheric residence time prior to collection.

- **La Merced.** La Merced is a large congested market near downtown Mexico City selling a variety of food and household items. A small percentage of soot particles sampled at this site were attributed to fresh emissions from vehicles passing near the collection device; the majority were most likely processed over less than a few hours residence time in the atmosphere.

- **CENICA supersite.** CENICA is located in a mixed commercial-residential area with relatively few industries or congested road networks, and was thus assumed to

be representative of ambient urban conditions. It is located 8.8 km southeast from La Merced, and 2 km south from a large food market (Central de Abastos) frequented by delivery trucks, particularly in the early morning. An analysis of the meteorological patterns during the collection period shows that particles were transported to CENICA in air masses coming predominantly from the north (de Foy et al., 2005). In the absence of any major non-traffic soot source in the immediate neighborhood, soot particles collected at CENICA were assumed to have originated in vehicular emissions primarily near the downtown area. Ambient particles were expected to have had the longest residence time of the three types of samples studied here, reflecting the maximum extent of processing in the urban environment.

## 3.3 Results

CCSEM/EDX, SEM and TEM analyses confirmed that soot and other carbonaceous particles were major components of MCMA aerosol concentration in the accumulation mode (TRAC collection size range of 0.2 – 2.0 $\mu$m). The physical and chemical characteristics of the individual particles observed in the analyzed samples were found to strongly depend upon their local environments.

### 3.3.1 Freshly-emitted soot from traffic

The AML was equipped with gas inlets that allowed for mobile sampling from different locations within and surrounding the MCMA. In "chase mode", the AML followed a target vehicle to characterize its emissions in real time (see for example, Canagaratna et al. (2004)). A video camera on-board provided a visual record of the vehicles sampled, which for the discussion here consisted mostly of taxis and colectivos. For these studies we did not attempt to investigate the particles emitted by individual vehicles, but instead sampled over a 5-minute average to include a representative collection of traffic emissions.

Mixed-traffic particulate emissions consisted of soot aggregates coated with a liquid-like substance as shown in Figure 3-4. This coating – apparent in the image as the darker gray substance surrounding the irregular soot aggregates – was most likely residue from unburned lubricating oil or fuel remaining on the emitted soot particles, and may have also included water soluble residues left on the substrate after drying in the vacuum chamber of

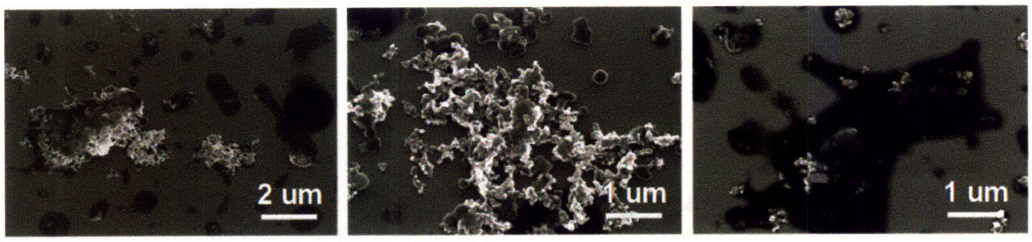


Figure 3-4: SEM images of freshly-emitted soot particles collected in city traffic during MCMA–2003. The darker areas apparent around the soot aggregates suggest a coating of unburned fuel and/or lubricating oil co-emitted during combustion.

the microscope. Sakurai et al. (2003) have shown that lubricating oil may comprise more than 95% of the volatile mass in diesel and gasoline emissions. Although this coating does not permit reporting an average particle diameter by CCSEM/EDX, closer inspection of the images reveals that mixed traffic emissions in the MCMA contained both submicron soot particles and larger aggregates $> 1$ $\mu$m in diameter.

More than 5000 individual particles were analyzed by CCSEM/EDX. Relative changes in particle elemental composition (element weight percent) are expressed in reference to carbon (S/C, O/C, N/C) to account for the carbon signal both from particles and the thin film substrate. This relative approach has been proven instrumental for distinguishing mixing characteristics of field collected particles including semi-quantitative analysis of low-Z elements (C, N, O) (Laskin et al., 2003).

Particulate traffic emissions in the MCMA were mostly carbonaceous with very low sulfur content. Figure 3-5a shows the narrow distribution and low median value of the S/C ratio in these particles determined by EDX. Since the very short residence time of fresh traffic particles leaves little opportunity for atmospheric processing, the sulfur detected in fresh soot particles most likely came directly from the fuel. During combustion, sulfur in gasoline or diesel fuel may be converted to sulfate in the presence of water vapor to condense on the soot particles (Shi and Harrison, 1999). Gasoline and diesel fuel at the time of this study reportedly contained a maximum of 500 to 1000 ppm, and average of 100 to 650 ppm of sulfur depending on grade (PEMEX, 2003). This is only slightly higher than sulfur in the fuel used by Tobias et al. (2001) in studies of diesel particulate emissions where only few percent $H_2SO_4$ was observed.

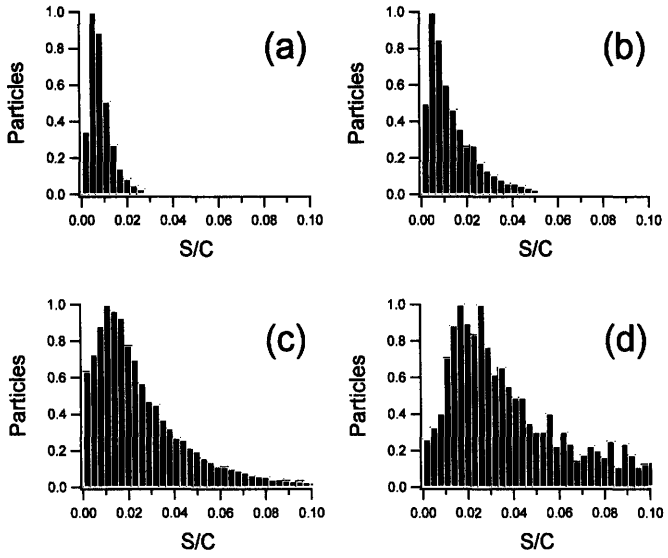


Figure 3-5: Normalized distribution of S/C ratios from CCSEM/EDX analysis of MCMA samples and of laboratory-generated $(NH_4)_2SO_4$ particles. S/C median values are (a) freshly-emitted soot from traffic = 0.007, (b) La Merced (downtown) = 0.010, (c) CENICA (ambient) = 0.020, (d) ammonium sulfate = 0.045.

### 3.3.2 La Merced market area

Particles collected near the La Merced market are visually and chemically distinguishable from those freshly-emitted and captured in traffic exhaust. As shown by SEM in Figure 3-6, particles from the La Merced site exhibited both internal and external mixing as they have coagulated with or become entrained within other particulate matter. A small percentage of unmixed soot aggregates suggests influence of fresh emissions from traffic passing in close proximity to the sampling site. A liquid-like coating was observed on the particles, but appeared less thick than observed on freshly-emitted soot particles. Differences in particulate emissions according to vehicle type and its fuel efficiency may explain the nature of this coating. The majority of particles are submicron in size with an average diameter of $0.37 \pm 0.20$ $\mu$m.

Nearly 75% of particles collected at La Merced contained sulfur; mixed particles also contained Si, K, Fe and Na. Sulfate inclusions on soot aggregates readily decomposed under the intensity of the electron beam as noted in other microscopy studies (Ebert et al., 2002; Li et al., 2003). Figure 3-5b illustrates the higher sulfur content of particles collected at La Merced and wider distribution of their S/C ratios in comparison to the particulate traffic

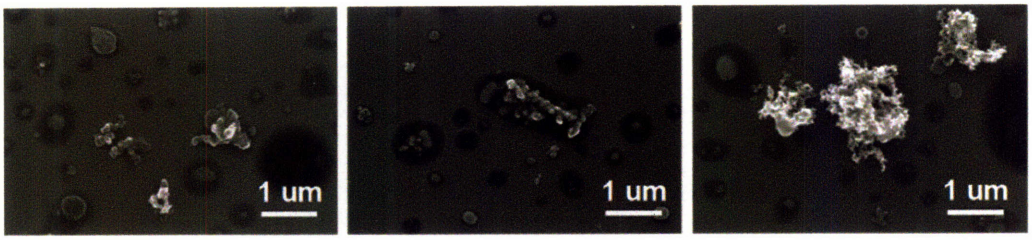


Figure 3-6: SEM images of partially-processed soot particles sampled near the downtown La Merced site expected to contain a mix of fresh particulate emissions from passing vehicles as well as more-aged particles.

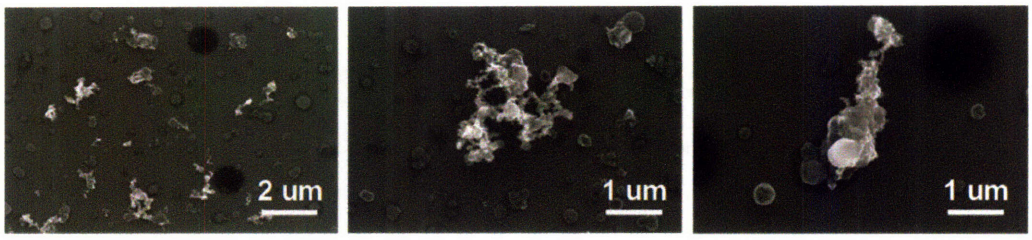


Figure 3-7: SEM images of ambient particles collected at CENICA during MCMA–2003.

emissions.

### 3.3.3 Particles collected from the CENICA Supersite

SEM analysis reveals that ambient soot particles in the MCMA were heavily internally mixed as shown in Figure 3-7. Detailed morphological and composition analyses show that they were extremely heterogeneous and contained inclusions of S, K, and Si, as well as Fe, Na and P to a lesser extent. Figure 3-8 shows an example of SEM/EDX analysis of an individual soot particle; inorganic components Si, K and S most likely originated from different sources and emphasize extensive particle mixing. Compositional analysis of MCMA aerosol by Proton-Induced X-ray Emission (PIXE) at the CENICA site confirms S, Si and K as leading inorganic elements in $PM_{2.5}$ (see Sec. 2.4). Although the vacuum conditions necessary for SEM and TEM analysis limit the detection of volatile organic, nitrate and chloride compounds, the heavy internal mixing shown in Figure 3-8 observed for the large majority of ambient particles strongly suggests that soot may be mixed with these compounds as well.

Ambient particles had relatively high sulfur content as shown in Figure 3-5c where their S/C ratios follow a wider distribution than particles collected either in traffic exhaust or

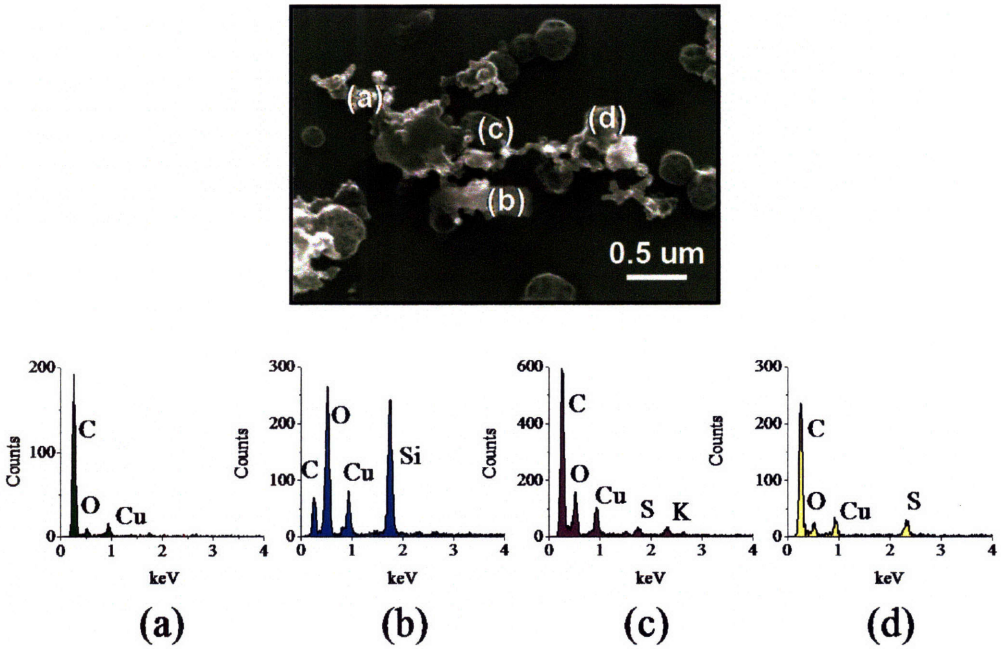


Figure 3-8: SEM/EDX analysis showing the relative amount of the element indicated in a single soot particle collected at CENICA; Cu is an artifact of the substrate grid.

near La Merced. CCSEM/EDX analysis of over 32,000 particles from CENICA shows that nearly 90% contained sulfur and the average particle diameter was 0.39 $\pm$ 0.19 $\mu$m.

Ammonia measurements, and Aerosol Mass Spectrometry (AMS) indicate that aerosols were neutralized during the majority of the campaign (Salcedo et al., 2006). To verify that sulfur was in the form of $(NH_4)_2SO_4$, TOF-SIMS analysis was done to make site-specific correlations among chemical ions in the particles. Overlapping $S^-$ and $NH_4^+$ in Figure 3-9 confirm the presence of $(NH_4)_2SO_4$ or $NH_4HSO_4$. $Si^+$ and $Al^+$ indicate soil components, while $K^+$ and $Na^+$ suggest biomass burning sources. The overlap between ion pairs indicates that both components were found on the surface of the particles, which implies a degree of internal mixing. Laboratory-generated $(NH_4)_2SO_4$ particles (0.55 $\pm$ 0.31 $\mu$m in diameter) were analyzed by CCSEM/EDX following the same procedure as MCMA samples in order to compare typical S/C values. The carbon signal detected by EDX in this sulfate control sample originated solely from the substrate. Figure 3-5 shows that the S/C ratios of aerosol particles collected at the CENICA site approach those measured for laboratory-generated $(NH_4)_2SO_4$ particles, and support extensive processing of particles by inorganic sulfates.

While the CCSEM was used to provide data over large number of particles with statis-

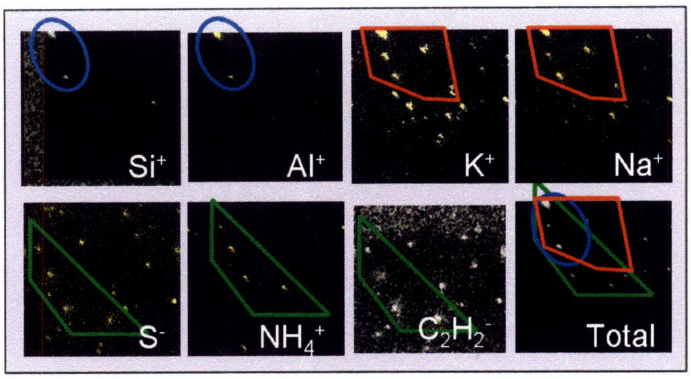


Figure 3-9: TOF-SIMS analysis of a particle sample collected at CENICA. The single ion and composite images show the presence of the ion as bright signal against the dark background. Borders have been drawn to emphasize overlapping areas. $S^-$ and $NH_4^+$ ions indicate ammonium sulfate, $Si^+$ and $Al^+$ suggest soil, $K^+$ and $Na^+$ most likely originate from biomass burning or crustal salts. Each image area is 50 $\mu$m x 50 $\mu$m.

tical depth, Transmission Electron Microscopy (TEM) was performed to study the internal structure and composition of individual particles of specific interest. TEM images shown in Figure 3-10 demonstrate two characteristic types of mixed soot/sulfate particles typical among the CENICA samples. In both images, soot, labeled (a), was unaffected by analysis whereas ammonium sulfate, labeled (b), rapidly decomposed under the intensity of the electron beam leaving behind sulfur residue. Whereas image (i) shows soot with a sulfate inclusion presumably from coagulation, image (ii) reveals soot spherules entirely embedded inside the remains of a sulfate particle and suggests condensation of sulfate on aged soot particles. The latter exemplifies the shell/core model discussed by Jacobson (2000), among others, in determining the optical properties of mixed soot particles which has been used to evaluate black carbon specific absorption during MCMA-2003 (Barnard et al., 2007). This important distinction in soot/sulfate mixing suggests that multiple mechanisms occur in the MCMA, consistent with previous observations of structural and compositional variation in carbonaceous particles found in urban environments (Katrinak et al., 1992; Wentzel et al., 2003).

## 3.4 Atmospheric processing and internal mixing

One of the distinct advantages of the TRAC–CCSEM/EDX approach is the ability to study aerosol composition as a function of time. Figure 3-11 shows the median values of S/C,

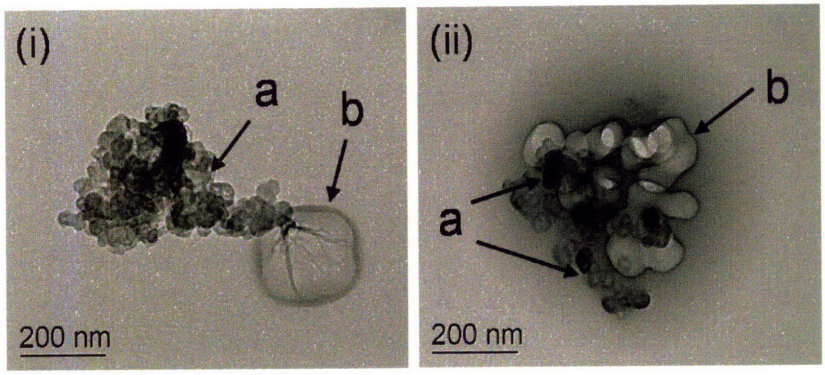


Figure 3-10: TEM images of mixed soot/sulfate particles collected at CENICA during MCMA–2003. In both images, soot chains (a) are internally-mixed with sulfate, (b) which is damaged by the electron beam leaving sulfur residue behind. Image (i) suggests coagulation whereas (ii) may indicate condensation of sulfate.

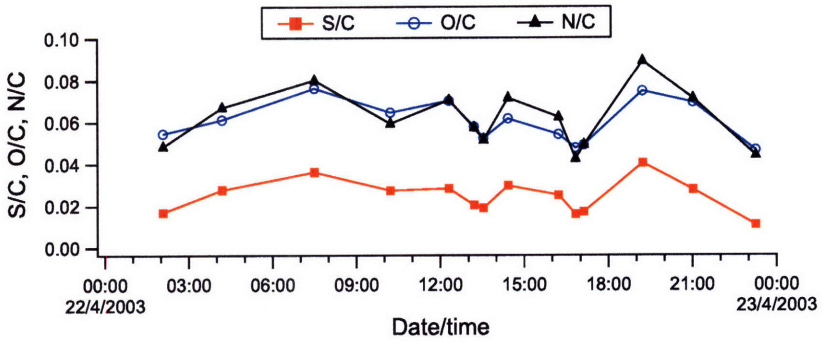


Figure 3-11: Particle composition as a function of time as measured by CCSEM/EDX for particles collected on April 22$^{nd}$ at CENICA during MCMA–2003.

O/C and N/C ratios from EDX analysis of individual ambient particles at CENICA over the course of one day (April 22$^{nd}$) during MCMA–2003. The ratios track one another and provide further evidence for ammonium sulfate in the mixed aerosol, as well as relatively high sulfur content in the particles. It is worth noting that a rain event occurred in the afternoon from approximately 3:30 – 4:30 pm. A decrease in S/C, O/C and N/C ratios after the rain is consistent with preferential washout of particles with higher degree of mixing which would arguably make them more hygroscopic.

As previously noted, the coating observed on both fresh soot and partially-processed soot is most likely unburned lubricating oil and/or condensed water remaining on the particles after their emission in vehicle exhaust. The limitation of microscopic analysis techniques to measure volatile and semi-volatile compounds complicates chemical identification of these

splashes. Although much of the organic particulate mass was assumed to have volatilized in the vacuum chamber prior to SEM/EDX analysis, the images of fresh soot particles suggest that a portion of the organics was retained or otherwise left a footprint around the soot particles. Measurements of organic H by PESA analysis (see Sec. 2.6.3) confirms retention of low vapor pressure organic compounds present in Mexico City aerosol. These microscopy images to suggest an organic coating are consistent with compositional studies on diesel particulate emissions by Sakurai et al. (2003) who noted a signature of unburned lubricating oil. Apparent differences in coating thickness may be related to the evaporation rate of the condensed species and effect of engine load on the volatile fraction of particulate emissions (Virtanen et al., 2004; Burtscher et al., 1998). The effect of an oil coating on the reactivity of soot, as well as the consequences on health have not been addressed and should be considered in future studies.

TEM has been used previously to investigate soot/sulfate mixing both in laboratory and field studies (Ebert et al., 2002; Pósfai et al., 1999). The fact that we have observed sulfate either encapsulating a soot aggregate, or as individual inclusions on soot suggests that multiple soot/sulfate mixing mechanisms occur in the MCMA. Two types of mixing shown by TEM analysis in Figure 3-10 offer evidence for both coagulation and condensation of sulfate on soot. These processes may occur on different time-scales depending on particle concentration and the rate of sulfate formation. For example, Riemer et al. (2004) modeled aging of soot and calculated that condensation of sulfate (as $H_2SO_4$) dominates during the day whereas coagulation is favored at night, largely due to the daytime production of sulfate by OH oxidation of $SO_2$.

In order to place our observations within context regarding particulate transport and residence time, it is important to note that MCMA pollutants are generally swept from the basin daily (Fast and Zhong, 1998; de Foy et al., 2006). As such, extensive internal mixing of soot cannot be explained by multiple day accumulation that allows for gradual processing. Most of our CENICA samples, including those featured in Figure 3-7, were collected on days when the winds came predominantly from the north/northwest at speeds between 1 m/s and 4 m/s (de Foy et al., 2005). The transport time for particles to reach CENICA from downtown areas such as La Merced would therefore range from little more than 30 mins to several hours. If we assume that the majority of soot particles collected at CENICA originated from downtown traffic, consistent with the wind direction and large

contribution of mobile sources to soot emissions in the MCMA, our results indicate that extensive soot processing occurs within hours. As an observation-based approximation, this should prompt more detailed laboratory studies of soot mixing times and the mechanisms involved.

The influence of the local environment on processing of particles and their mixing characteristics has been noted previously. Mallet et al. (2004) and Hasegawa and Ohta (2002) discuss the differences in mixing characteristics of aerosols in urban vs. rural locations, and have used their findings to suggest that urban aerosols tend to be externally mixed whereas aerosols in remote areas are more often internally mixed. They reason that aerosols in remote areas have a longer residence time, resulting in more extensive processing. Indeed, Pósfai et al. (1999) and Clarke et al. (1997) report internal mixing of soot/sulfate particles over the South Atlantic Ocean; (Pósfai et al., 1999) estimated that 11% to 46% of sulfate aerosols contained a soot core. Our results show a high degree of internal mixing of aerosols in urban environments; the especially large vehicle fleet in Mexico City, high particulate emissions, and enclosed topography of the MCMA help to rationalize this intense particle mixing.

Internal mixing with sulfate is expected to affect the lifetime of soot in the atmosphere. Freshly-emitted soot particles are initially hydrophobic but may become more susceptible to removal by wet deposition once they have collected soluble components. Although the ability of soot particles to be washed out is not currently well characterized, measurements such as those by Sellegri et al. (2003) show substantial wet scavenging of aged carbon aerosols. Global climate models estimate a lifetime of soot of 4 to 10 days (Chung and Seinfeld, 2002; Cooke and Wilson, 1996; Barth and Church, 1995; Liousse et al., 1996) by making different assumptions on the time required for hydrophobic soot to become hydrophilic. Chung and Seinfeld (2002) used an exponential hydrophobic soot lifetime of 1.15 days, while Cooke and Wilson (1996) assumed an arbitrary 5% conversion per 2 hour time step. The extensive soot processing we have observed in the MCMA suggests that the hydrophobic lifetime of soot particles in urban environments, and hence the particles' overall atmospheric lifetimes, may be overestimated. A shorter lifetime of soot would also impact its range of transport after emission in traffic and from other anthropogenic sources.

## 3.5 Conclusions and atmospheric importance

The mixing state of soot has an immediate impact on its direct/indirect climate effects and atmospheric lifetime. The acquisition of water-soluble organic and inorganic compounds on soot surfaces increases their capacity to influence precipitation patterns, and accordingly their susceptibility for wet deposition removal. The ability of global climate models to accurately quantify the net climatic effects of soot is limited on an understanding of its hydrophobic-to-hydrophilic conversion rate, which depend upon the characteristics of the local environment in which the particles originate.

Mobile sources comprise a major fraction of particulate emissions in the MCMA, and an important source of soot aerosols. Comparative chemical and morphological analysis of freshly-emitted soot collected in city traffic, mixed particles with a few hours' estimated residence time, and ambient samples provided evidence for significant physical and chemical processing in the MCMA within short time-scales. It appears that particles become extensively internally mixed within several hours to one day, likely expedited by a high volume of particulate and gaseous emissions and intense photochemistry. TEM analysis shows two distinct types of soot/sulfate mixing which suggest that both sulfate coagulation and condensation are important within the urban atmsosphere, and encourage additional laboratory studies to clarify the detailed reaction mechanisms. Evidence for an oil coating on freshly-emitted soot particles should be examined more closely both in terms of reactivity and consequences for human health.

# Chapter 4

# OH-initiated oxidation of carbonaceous films as surrogates for atmospheric aerosols

## 4.1 Introduction

In addition to physical processing of carbonaceous aerosols, chemical reaction may also significantly change their properties. The hydroxyl radical (OH) is the most efficient oxidant in the atmosphere and the dominant sink for carbon monoxide (CO), methane ($CH_4$), and volatile organic compounds (VOCs). The lifetime of these species may be calculated from their respective rate constants and the OH concentration, $\tau = 1/k_{OH}[OH]$, giving $\tau_{CO}$ = 1 to 4 months, $\tau_{CH4}$ = 12 to 16 years, and $\tau_{VOC}$ = 1 hour to several weeks. OH radicals efficiently initiate reactions on organic aerosol surfaces (chemical processing) thereby directly impacting their atmospheric lifetimes and environmental effects. OH-initiated oxidation is a major force behind determining aerosol lifetimes based on the time required for either decomposition or increased hygroscopicity leading to efficient wet deposition removal.

The dominant source of OH in the troposphere is photolysis of ozone ($O_3$) forming excited oxygen atoms ($O(^1D)$) which react with water vapor:

$$O_3 + h\nu \ (\lambda < 335 \text{ nm}) \rightarrow O(^1D) + O_2 \quad (4.1)$$

$$O(^1D) + H_2O \rightarrow 2OH \quad (4.2)$$

where the $O(^1D)$ yield from $O_3$ is approximately 10% due to quenching to ground-state O ($^3P$) by collision with $N_2$ or $O_2$:

$$O(^1D) + M \rightarrow O(^3P) + M \tag{4.3}$$

Additional sources of OH include photolysis of nitrous acid (HONO), hydrogen peroxide ($H_2O_2$), and formaldehyde (HCHO) in a two-step reaction via hydroperoxyl radicals ($HO_2$):

$$HONO + h\nu \ (\lambda < 400 \text{ nm}) \rightarrow OH + NO \tag{4.4}$$

$$H_2O_2 + h\nu \ (\lambda < 370 \text{ nm}) \rightarrow 2OH \tag{4.5}$$

$$HCHO + h\nu \ (\lambda < 350 \text{ nm}) + 2O_2 \rightarrow 2HO_2 + CO \tag{4.6}$$

$$HO_2 + NO \rightarrow OH + NO_2 \tag{4.7}$$

OH plays an integral role in $O_3$ smog formation through $HO_x$ (= OH + $HO_2$) and $NO_x$ (= NO + $NO_2$) cycling reactions. The $NO_2$ generated in Reaction 4.7 readily photolyzes in the troposphere to produce oxygen atoms which combine with atmospheric $O_2$ forming $O_3$:

$$NO_2 + h\nu \ (\lambda < 420 \text{ nm}) \rightarrow NO + O(^3P) \tag{4.8}$$

$$O(^3P) + O_2 + M \rightarrow O_3 + M \tag{4.9}$$

$$NO + O_3 \rightarrow NO_2 + O_2 \tag{4.10}$$

Average OH concentrations in the troposphere range from 0.02–0.5 ppt ($0.05–1{\cdot}10^7$ $cm^{-3}$) (Finlayson-Pitts and Pitts, 2000).

### 4.1.1 Reaction mechanism for OH-initiated oxidation of alkane compounds in the gas phase

VOC reactions of the type OH + RH, where RH may be an alkane, alkene, or aromatic compound, have been extensively studied in the gas phase (Atkinson, 2000, 1997b). Direct measurements of the reaction products, or calculated values of individual reaction rates provide evidence of specific mechanisms. Far less information is available for heteroge-

neous oxidation, however. To date there have been no detailed studies into the reaction mechanisms responsible for oxidation of organic aerosol. Given the large variety of organic compounds present in the troposphere, and assuming that most have at least partial saturation, it is both appropriate and practical to focus on the OH-initiated oxidation of alkane molecules. This provides the background to our studies into the heterogeneous reaction with organic aerosols.

$$RH + OH^{\cdot} \rightarrow R^{\cdot} + H_2O \tag{4.11}$$

$$R^{\cdot} + O_2 + M \rightarrow RO_2^{\cdot} + M \tag{4.12}$$

$$RO_2^{\cdot} + RO_2^{\cdot} \rightarrow 2RO^{\cdot} + O_2 \tag{4.13}$$

$$\rightarrow R'OH + R''CHO + O_2 \tag{4.14}$$

$$\rightarrow ROOR + O_2 \tag{4.15}$$

$$RO_2^{\cdot} + HO_2^{\cdot} \rightarrow ROOH + O_2 \tag{4.16}$$

$$RO_2^{\cdot} + NO \rightarrow RO^{\cdot} + NO_2 \tag{4.17}$$

$$RO_2^{\cdot} + NO + M \rightarrow RONO_2 + M \tag{4.18}$$

$$RO_2^{\cdot} + NO_2 + M \leftrightarrow RO_2NO_2 + M \tag{4.19}$$

$$RO^{\cdot} \rightarrow R'^{\cdot} + R''CHO \tag{4.20}$$

$$\rightarrow R'^{\cdot}OH \tag{4.21}$$

$$RO^{\cdot} + O_2 \rightarrow R'CHO + HO_2^{\cdot} \tag{4.22}$$

Oxidation of gas-phase alkanes proceeds in a series of elementary reactions (Reactions 4.11 to 4.22); an illustration of the mechanism for *n*-hexane is shown in Figure 4-1. The key intermediates are alkyl ($R^{\cdot}$), alkoxy ($RO^{\cdot}$), and alkyl peroxy ($RO_2^{\cdot}$) radicals. OH initiates the reaction sequence by abstracting a hydrogen atom to produce water and $R^{\cdot}$ which promptly adds $O_2$ under atmospheric conditions to form the corresponding $RO_2^{\cdot}$ radical. Peroxy self-reaction, or reaction with another $RO_2^{\cdot}$ may produce $RO^{\cdot}$ radicals (Reaction 4.13) or non-radical products (Reaction 4.14); peroxide (ROOR) formation via molecular cross-linking (Reaction 4.15) is a minor channel under atmospheric conditions. Alkyl peroxy

radicals may also react with NO to form either RO$^{\cdot}$ radicals and $NO_2$ (hence participating in $NO_x$ cycling) or alkyl nitrates ($RONO_2$), or may also react with with $NO_2$ in a pressure-dependent, reversible process to form alkyl peroxynitrates ($RO_2NO_2$). Finally, RO$^{\cdot}$ radicals react in three major channels: unimolecular decomposition via C–C bond scission (Reaction 4.20), unimolecular isomerization (Reaction 4.21), or reaction with $O_2$ to generate $HO_2$ radicals and an aldehyde or ketone (Reaction 4.22). Note that the $HO_2$ generated in this reaction may further participate in $HO_x$ and $NO_x$ cycling. Under atmospheric conditions, these three channels dominate over reactions of the type RO$^{\cdot}$ + $NO_x$. Experimental difficulties associated with detection of short-lived radical intermediates have prohibited direct measurement of many species, but theoretical estimates based on molecular structure and quantum mechanical calculations have proven useful to supply missing rate and mechanistic information.

### 4.1.2 OH attack

Atkinson (2003) gives the OH + RH rate constants for a large body of gas-phase alkanes (Fig. 4-2) showing a positive correlation with increasing carbon chain length. Thermochemical arguments based on molecular structure are useful to rationalize observed reaction rates. Hydrogen abstraction by OH is thermodynamically driven by formation of a strong O–H bond (498 kJ/mol) vs. breaking the weaker C–H bond (410 kJ/mol). OH attack occurs preferentially on tertiary or secondary C–H bonds due to a 15 to 30 kJ/mol lower bond dissociation energy in comparison to primary C–H bonds. A greater number of $CH_2$ groups available for H-abstraction helps to explain increasing reaction rate with carbon chain length. The plateau in Figure 4-2 suggests that RH + OH reaction rates approach the gas–kinetic limit ($k \approx 10^{-10}$ cm$^3$/molec/s). Entropy, in addition to enthalpy, contributes to the overall reaction rate. Increasing molecular weight causes a decrease in the entropy of activation ($\Delta S^{\ddagger}$) per H as changes in translational and rotational degrees of freedom related to formation of the activated complex become progressively smaller. Size-related entropic effects become negligible as C $\geq$ 12, however (Cohen, 1991).

### 4.1.3 Alkyl peroxy radical reactions

Alkyl radicals resulting from OH-attack react rapidly and exclusively with $O_2$ under atmospheric conditions with a lifetime on the order of ~10 ns. Gas-phase $RO_2^{\cdot}$ radicals in

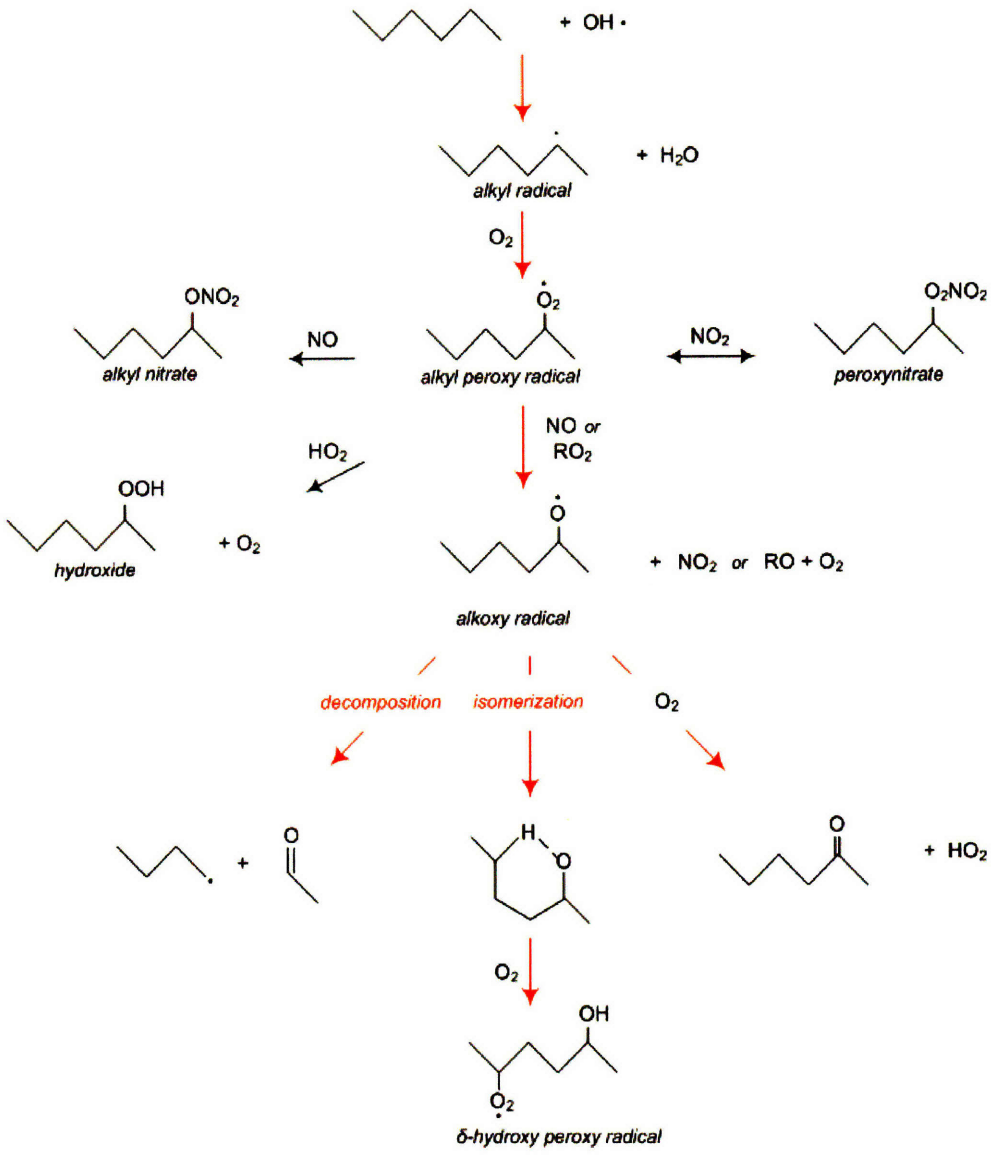


Figure 4-1: Reaction mechanism for OH-initiated oxidation of $n$-hexane.

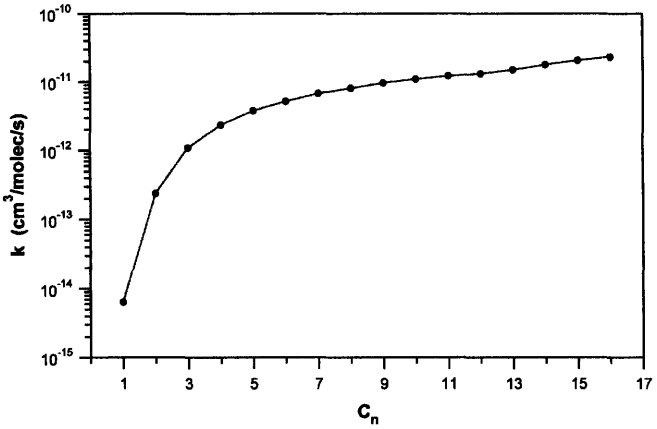


Figure 4-2: Rate constant for gas-phase OH + RH as a function of alkane chain length; data from Atkinson (2003).

the troposphere react predominantly with other $RO_2\cdot$ radicals, $HO_2$ radicals, and $NO_x$. Self-reaction rates can vary by orders of magnitude depending upon the structure of $RO_2\cdot$ and decrease with greater substitution at the carbon atom (primary > secondary > tertiary) due to steric effects. Rate constants for $RO_2\cdot + HO_2$ have been measured at $k = (4\text{–}12)\cdot 10^{-12}$ $cm^3$/molec/s while reactions $RO_2\cdot + NO$ proceed faster, $k = (0.7\text{–}2)\cdot 10^{-11}$ molec/$cm^3$/s (Wallington et al., 1992). Alkyl peroxy radicals can combine with NO or $NO_2$ in a pressure and temperature dependent reaction to form alkyl nitrate or alkyl peroxynitrate compounds, respectively. Formation of alkyl nitrates is postulated to proceed via isomerization of a short-lived ROONO intermediate (Zhang et al., 2004). Product studies for $C_5$ – $C_{15}$ linear alkanes indicate an increasing yield of alkyl nitrate and hydroxyalkyl nitrate compounds with increasing chain length, suggesting greater importance of NO addition (Reisen et al., 2005; Lim and Ziemann, 2005; Arey et al., 2001). Alkyl peroxynitrates are less stable than alkyl nitrates and thermally decompose with a lifetime of several seconds at ambient temperatures (Lightfoot et al., 1992; Zabel et al., 1989).

### 4.1.4 Alkoxy radical reactions

As key intermediates in the breakdown of VOCs, alkoxy radicals have been the focus of many studies (Atkinson, 1997a; Orlando et al., 2003; Libuda et al., 2002; Johnson et al., 2004; Kwok et al., 1996; Eberhard et al., 1995; Cassanelli et al., 2005; Méreau et al., 2000;

Table 4.1: Rate constants for several atmospheric alkoxy radicals at 298K and 1 atm; adapted from Finlayson-Pitts and Pitts (2000).

| Radical | $k_{4.20}$ ($s^{-1}$) | $k_{4.21}$ ($s^{-1}$) | $k_{4.22}$ ($cm^3$/molec/s) |
|---|---|---|---|
| $CH_3CH_2O^{\cdot}$ | 0.31 | – | $1{\cdot}10^{-14}$ |
| $CH_3CH_2CH_2CH_2O^{\cdot}$ | $5.8{\cdot}10^{2}$ | $2{\cdot}10^{5}$ | $1{\cdot}10^{-14}$ |
| $CH_3CHO^{\cdot}CH_2CH_3$ | $2.3{\cdot}10^{4}$ | – | $8{\cdot}10^{-15}$ |
| $(CH_3)_3CO^{\cdot}$ | $1{\cdot}10^{3}$ | – | – |
| $CH_3CHO^{\cdot}CH_2CH_2CH_3$ | $1.7{\cdot}10^{4}$ | $2{\cdot}10^{5}$ | $8{\cdot}10^{-15}$ |
| $CH_3CH_2CHO^{\cdot}CH_2CH_3$ | $1.6{\cdot}10^{4}$ | – | $8{\cdot}10^{-15}$ |
| $CH_3CHO^{\cdot}(CH_2)_3CH_3$ | $2.8{\cdot}10^{4}$ | $2{\cdot}10^{6}$ | $8{\cdot}10^{-15}$ |
| $CH_3CH_2CHO^{\cdot}(CH_2)_2CH_3$ | $3.4{\cdot}10^{4}$ | $2.0{\cdot}10^{5}$ | $8{\cdot}10^{-15}$ |
| $(CH_3)_3CCH_2O^{\cdot}$ | $9.8{\cdot}10^{3}$ | $\geq 7{\cdot}10^{4}$ | $7.6{\cdot}10^{-13}$ |

Buback et al., 2005). Table 4.1 lists experimentally measured rate constants for the three major reaction channels (Reactions 4.20 to 4.22) for a selection of simple alkoxy radicals. Competition among decomposition, isomerization, and reaction with $O_2$ under various atmospheric conditions is expected to determine the final oxidation product distribution.

- **Decomposition**

  Unimolecular decomposition leads to rapid fragmentation of the parent hydrocarbon and production of shorter chain radicals available to participate in subsequent radical cycling reactions. Differences in RO$^{\cdot}$ decomposition rates are attributed to the Arrhenius activation energy ($E_a$) required to break the C–C bond:

$$k = Ae^{-E_a/RT} \tag{4.23}$$

  which in turn depends upon molecular structure. Various studies have invoked an Evans–Polanyi relationship to estimate the reactivity for a wide array of organic compounds (Choo and Benson, 1981; Johnson et al., 2004). This approach assumes a linear relationship between $E_a$ and the reaction enthalpy ($\Delta H_{rxn}$):

$$E_a = \alpha \Delta H_{rxn} + \beta \tag{4.24}$$

  where $\alpha$ and $\beta$ are empirical constants extracted from analysis of experimental data. The value of $\alpha$ has been found to depend upon the structure of the alkyl radical scission product, decreasing with increased radical stability. An alternative structure-reactivity approach expresses the stability of the R$^{\cdot}$ radical in terms of its ionization

potential (IP) (Orlando et al., 2003; Atkinson, 1997b):

$$E_a = (2.4(IP) - 11.8) + 0.58\Delta H_{rxn} \tag{4.25}$$

Formation of the most highly substituted radical is generally favored to minimize energy in accordance with molecular orbital (MO) theory.

Studies involving short-chain alkane molecules ($C_2$ to $C_4$) show that the $RO_2^{\cdot}$ + NO reaction (4.16) is exothermic by 50 – 100 kJ/mol; energy transferred to the $RO^{\cdot}$ product can result in its prompt decomposition (Cassanelli et al., 2005; Libuda et al., 2002; Orlando et al., 2003). The $E_a$ barriers for $RO^{\cdot}$ decomposition have been measured within a range of 84 kJ/mol for $C_2H_5O^{\cdot} \rightarrow CH_3^{\cdot} + CH_2O$, to 42 kJ/mol for $(CH_3)_3CCH_2O^{\cdot} \rightarrow C(CH_3)_3^{\cdot} + CH_2O$ (Orlando et al., 2003). Substituted $RO^{\cdot}$ radicals may have lowered $E_a$ values depending on the nature of the radical created by the C–C bond scission and opportunity for increased stabilization. The magnitude of the energy barrier for decomposition in relation to atmospheric temperature is an important consideration when extrapolating laboratory results to various altitudes given the decrease of 6 – 7 °C per km in the troposphere (Finlayson-Pitts and Pitts, 2000).

- **Isomerization**

  Alkoxy radical isomerization results in a hydroxy-substituted alkyl radical where a 1,5-H shift is preferred due to formation of a 6-membered, essentially unstrained, transition state. Addition of $O_2$ leads to formation of the corresponding $\delta$-hydroxyperoxy and $\delta$-hydroxyalkoxy radicals; subsequent isomerizations of $RO^{\cdot}$ are expected to occur more quickly (Atkinson, 1997a; Kwok et al., 1996). Absolute rates or temperature dependences for isomerization are not readily available but rate information may be obtained in relation to the other channels for decomposition or reaction with $O_2$. Activation energies have been estimated by quantum mechanical calculations with values 30 – 40 kJ/mol and preexponential A-factors within a range of $(2\text{–}5)\cdot 10^{12}$ $s^{-1}$ (Orlando et al., 2003). Isomerization A-factors are roughly 1 to 2 orders of magnitude lower than decomposition due to a high entropy of activation.

  Product studies have shown evidence for faster rates of isomerization with increasing alkane chain length (C $\geq$ 4) including increased yields of hydroxycarbonyl and

hydroxyalkyl nitrates (Eberhard et al., 1995; Reisen et al., 2005; Kwok et al., 1996; Arey et al., 2001). Kwok et al. (1996) reported a decreasing yield of carbonyl products with the same number of carbons as the parent alkane ($n$-butane to $n$-octane), but an increase in the hydroxycarbonyl/carbonyl ratio, and concluded that formation of $\delta$-hydroxycarbonyls were the dominant products for OH-oxidation of longer-chain $n$-alkanes. Arey et al. (2001) has reported a positive correlation between the yield of $\delta$-hydroxyalkyl nitrates (in presence of NO) and carbon chain length.

- **Reaction with $O_2$**

  Oxygen reacts with RO· radicals via $\alpha$-hydrogen abstraction to generate $HO_2$ and carbonyl (aldehyde or ketone), thereby terminating the VOC decomposition sequence until initiation by another OH radical. The $HO_2$ radicals produced in this way may participate in $HO_x$ and $NO_x$ cycling related to $O_3$ formation. Since tertiary RO· radicals do not have an $\alpha$-hydrogen available for $O_2$ attack, this channel is only accessible to primary and secondary radicals. Reaction with $O_2$ is the dominant fate of RO· radicals C $\leq$ 3 with a rate $k_{4.22} = (0.5 - 2)\cdot 10^{-14}$ cm$^3$/molec/s (see Table 4.1) (Orlando et al., 2003; Finlayson-Pitts and Pitts, 2000). Similar to RO· decomposition, the relative importance of the $O_2$ reaction channel is sensitive to altitude considering a decrease in pressure (and $O_2$ concentrations) with increasing height. Because activation barriers for RO· decomposition are generally higher than for reaction with $O_2$, the latter channel likely becomes more dominant at higher altitudes (Cassanelli et al., 2005; Atkinson, 1997a).

In summary, OH-initiated oxidation of organic compounds proceeds via a radical mechanism involving R·, RO·, and $RO_2$· species where the accessibility of various reaction pathways depends upon the structure and stability of reactive intermediates, as well as energy available to surmount activation barriers. Although much of the previous discussion was specific to gas phase comounds, a similar sequence of reactions can describe heterogeneous oxidation.

### 4.1.5 Atmospheric oxidation in liquids and solids

Despite increasing recognition of the importance of heterogeneous processes in the atmosphere, parameterization of the chemical mechanisms involved remains preliminary (Rudich

et al., 2007). Many rate constants for the elementary reactions involved in heterogeneous OH-oxidation have not yet been measured experimentally, or are not known at ambient temperatures $\sim$ 300K. A large database of information on gas-phase reactions provides a valuable resource to draw upon, provided that certain differences applicable to surfaces are considered.

Whereas radical reactions in the gas-phase may occur within the entire given volume, the space available for reactions in liquids and solids is limited to a smaller "free volume". This is described by the "cage effect" where solvent molecules provide the cage in liquids, and close packing between molecules in a solid film creates a similar restriction ("rigid cage effect") (Denisov and Afanas'ev, 2005). The cage may enhance the probability for interactions between neighboring molecules, but may also impose diffusion or steric restrictions that impede reactants from meeting with the correct orientation, thereby decreasing reaction rates. The free volume can be obtained from a compound's crystal structure to assess possibility for steric restrictions. Solubility of gas-phase reactants into the medium and re-establishment of the equilibrium at the interface as expressed by the Henry's law constant should be considered in addition to diffusion restrictions. The diffusion of $O_2$ into polyethylene, $D_{O2} = 1.2{\cdot}10^{-6}$ cm$^2$/s (Denisov and Afanas'ev, 2005), is orders of magnitude slower than $O_2$ diffusion in air, $D_{O2} = 0.22$ cm$^2$/s (Ivanov et al., 2007), for example. Neighboring molecules may also help to stabilize the transition state and/or intermediates of a reaction with a decrease in the activation energy barrier. Thus additional structural parameters are required to accurately describe a heterogeneous reaction.

### 4.1.6 Status of heterogeneous studies

Numerous studies have been performed to investigate $O_3$ and $NO_x$ reactivity with organic aerosols or surfaces (Katrib et al., 2004; Ziemann, 2005; Hearn et al., 2005; McNeill et al., 2007; Knopf et al., 2006; Thornberry and Abbatt, 2004) with relatively few data available regarding OH radicals (Bertram et al., 2001; Molina et al., 2004; Eliason et al., 2004). This is despite the fact that the high reactivity of OH can compensate for its lower tropospheric concentration in comparison to $O_3$ and $NO_x$ ($\sim$ 100 ppbv = $2{\cdot}10^{12}$ molec/cm$^3$, urban environments) (Finlayson-Pitts and Pitts, 2000). Whereas $O_3$ reacts selectively with unsaturated bonds with an uptake coefficient $\gamma_{O_3} \sim 10^{-3}$ for oleic acid, linoleic acid, and linolenic acid (Hearn et al., 2005; Thornberry and Abbatt, 2004), OH readily reacts with a

wide variety of organic surfaces with an uptake near unity, $\gamma_{OH} \sim 1$ (Bertram et al., 2001).

OH-initiated oxidation of organic molecules may lead to either increased oxygen functionality via formation of carbon-oxygen containing groups on the surface, or decomposition through C–C bond scission. Experimental data show evidence for both reaction pathways, although the parameters favoring one over the other are unknown and the relevant reactions rates are uncertain. Eliason et al. (2004) studied the condensed phase products from oxidation of alkane films by exposure to a mixture of $O_3$ and OH in a $NO_x$–free environment. By chromatographic identification of the reaction products, they concluded that the mechanism proceeded by $RO_2\cdot$ to $RO\cdot$, forming ketones and aldehydes consistent with the decomposition and $O_2$ reaction pathways for $RO\cdot$ radicals.

Our laboratory recently reported that OH-initiated oxidation of organic thin films at room temperature leads to prompt surface degradation and volatilization through C–C bond scission (Molina et al., 2004). These results were used to develop a qualitative heterogeneous mechanism analogous to gas-phase oxidation with several key differences, notably enhanced OH reactivity, fast $RO_2\cdot$ self-reaction between neighboring molecules constrained to the surface, and efficient $\beta$-scission of the resulting $RO\cdot$ radical. Of the three competing $RO\cdot$ reaction channels (Reactions 4.20 to 4.22), only scission is expected to result in a net carbon loss from the surface in the form of gas-phase products. Because experimental conditions constrained $O_2$ to an upper limit of $3{\cdot}10^{16}$ molec/cm$^3$ (1 Torr), it was unknown to what extent $RO\cdot + O_2 \rightarrow RCHO + HO_2$ (Reaction 4.22) might become important in the troposphere, where $[O_2] = 5{\cdot}10^{18}$ molec/cm$^3$. Since H-abstraction by $O_2$ effectively terminates the oxidation sequence by formation of non-radical products, it is important to probe the mechanism over a range of $O_2$ concentrations to assess the importance of the decomposition as a possible atmospheric removal mechanism.

The following describes experiments examining OH-initiated oxidation of alkane and other carbonaceous surfaces under conditions applicable to the troposphere in order to gain more detailed information regarding the reaction mechanism. This information is essential to understanding the reactions for chemical processing of aerosols that determine their properties and atmospheric lifetimes, as well as the link to gas-phase radical cycling phase partioning.

## 4.2 Experimental

Studies were performed with a novel Quartz Crystal Microbalance – Chemical Ionization Mass Spectrometry (QCM–CIMS) system designed to enable real-time measurement of heterogeneous reactivity in conjunction with quantification of gas-phase reactants. The experimental setup is shown in Figures 4-3 and 4-4; a brief introduction and discussion of each of the individual components (CIMS, QCM, flow system and sample preparation) is provided below.

### 4.2.1 Chemical Ionization Mass Spectrometry (CIMS)

Chemical ionization (CI) is a "soft" ionization technique whereby the neutral analyte undergoes charge transfer from a parent ion for detection (Harrison, 1991). This approach generally prevents extensive fragmentation that can result from electron impact (EI). In negative CI, the analyte should have a higher electron affinity than the parent ion:

$$A + X^- \rightarrow A^- + X \tag{4.26}$$

where $A$ is the analyte and $X^-$ is the parent ion which enables charge transfer. Chemical ionization has been used extensively in our laboratory for detection and quantification of OH over a range of pressures with high sensitivity ($\geq 1{\cdot}10^{10}$ molec/cm$^3$ at S/N = 1) (Lipson et al., 1999; Bertram et al., 2001).

A quadrupole chemical ionization mass spectrometer (CIMS) was built specifically for use in the QCM–CIMS experiments in order to quantify OH concentrations prior to exposure to carbonaceous thin films. The CIMS instrumental design is shown in Figure 4-3, consisting of a CI region leading into two vacuum chambers housing a series of focusing lenses and the quadrupole used for ion detection. A 1 mm aperature separates the CI region from the main flow tube and creates a pressure drop in order to maintain the flow tube at relatively high pressure ($P_{FT}$ = 100 Torr) while reducing pressure in the CI region ($P_{CI}$ = 5 – 10 Torr) to optimize conditions for ion–molecule reactions. $SF_6^-$ parent ions were used throughout this study and were generated by passing a small flow of $SF_6$ through a $^{210}$Po $\alpha$-ionizer (NRD, LLC). The $SF_6^-$ ions and neutral/radical species originating in the flow tube meet in the CI region for charge transfer; the analyte is present in excess over $SF_6^-$ ions such that the obtained ion signal is proportional to the concentration in the flow tube. The

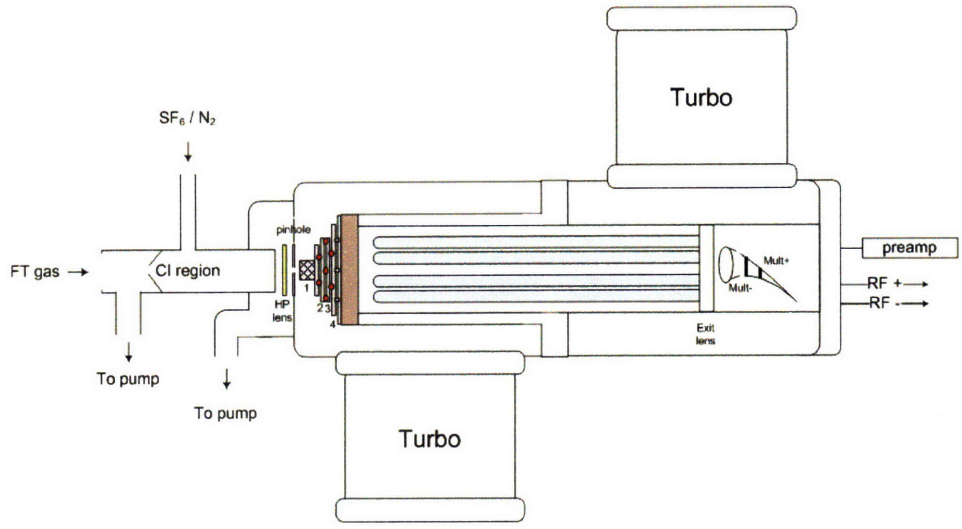


Figure 4-3: Chemical Ionization Mass Spectrometer (CIMS). Neutral/radical species from the flow tube (FT) undergo charge transfer with $SF_6^-$ ions in the chemical ionization (CI) region. The resulting ions enter the mass spectrometer chambers through a 200 $\mu$m pinhole and are focused by lenses for mass selection with the quadrupole.

resulting ions in the CI region are then focused through a high pressure (HP) lens and 200 $\mu$m pinhole into the vacuum region of the mass spectrometer. This orifice creates a second pressure drop from the CI region to maintain the mass spectrometer at low pressure by two turbomolecular pumps (Edwards EXT-501 and Varian V-550). The MS pressure is monitored by a nude-type tungsten filament ion gauge (Varian 580); pressures typically ranged from $(0.5 - 1)\cdot 10^{-5}$ Torr under flow conditions and $\sim 5\cdot 10^{-8}$ Torr in absence of gas flows. A custom-built lens assembly consisting of four optics was used to focus ions into the quadrupole (5/8" diameter rods, Extrel) and through a final exit lens to strike the surface of the electron multiplier (Burle Channeltron). An external preamplifier (MTS-100) processes the signal for analysis by specialized software (Merlin, Extrel). The quadrupole is controlled by a QC-150 RF power supply and two DC power supplies to support both low and high mass ranges. The QC-150 was calibrated for a total mass range 1 – 1000 amu at the time of these studies.

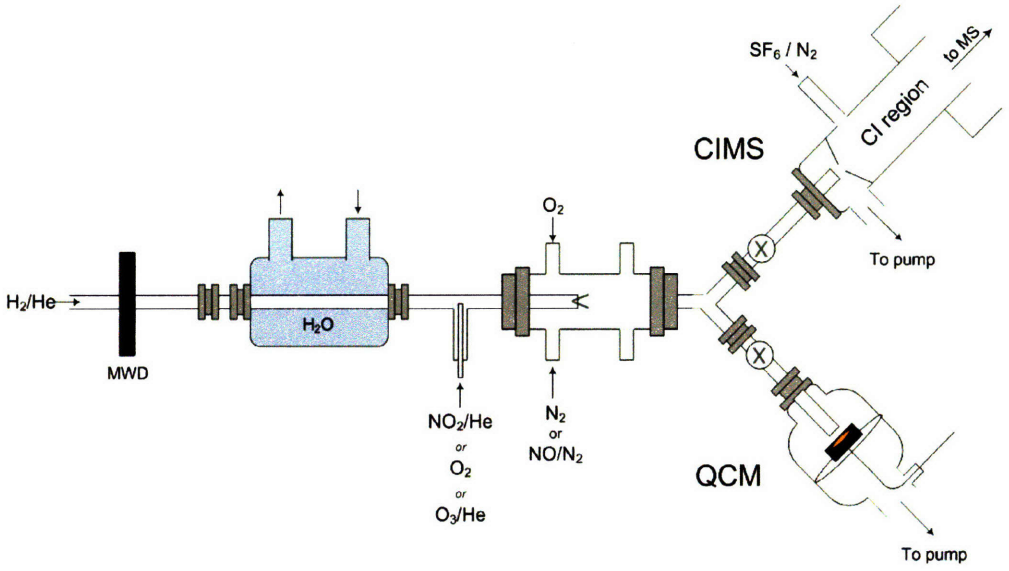


Figure 4-4: Quartz Crystal Microbalance – Chemical Ionization Mass Spectrometer (QCM–CIMS) system. A flow tube is used to generate and transport OH radicals to study the heterogeneous reaction between gaseous OH radicals and solid carbonaceous surfaces. The OH radicals are alternated between the CIMS and QCM by means of Teflon valves whereby the OH concentration is quantified by CIMS and the reaction monitored with the QCM through a relative change in organic mass deposited on an oscillating quartz crystal.

### 4.2.2 Quartz Crystal Microbalance (QCM)

The QCM is a highly sensitive piezoelectric sensor capable of detecting monolayer changes in mass deposited on a quartz crystal surface. For uniform thin films, the change in crystal oscillating frequency is linearly proportional to a change in mass as described by the Sauerbrey equation (Lu and Czanderna, 1984):

$$\Delta freq = -C_f \Delta mass \tag{4.27}$$

where $C_f$ is a sensitivity factor that depends upon the intrinsic properties of quartz:

$$C_f = \frac{2{f_q}^2}{\rho_q \nu_q} \tag{4.28}$$

$f_q$ = resonant frequency of the crystal

$\rho_q$ = density of quartz

$\nu_q$ = shear wave velocity

For the 6 MHz crystals used here, $C_f$ = 0.0815 Hz/ng/cm$^2$ corresponding to a mass resolution $\pm$ 1.2 ng/cm$^2$. In theory, the QCM does not require calibration but the above relationship applies only to uniform thin films in a gaseous environment. In the case of liquids, as in electroplating applications, the viscosity and density of the medium should be taken into account. Accuracy in QCM mass measurement depends upon the signal stability (i.e., ability to establish a lock on the fundamental vibrational frequency of the mass-loaded crystal) as well as possible external interferences. Our QCM-CIMS experimental setup was designed to maintain frequency stability under equilibrated temperature and pressure conditions such that only changes related directly to the carbonaceous film would result in frequency shifts detected by the QCM. In absence of reaction or volatilization of compounds due to vapor pressure considerations at reduced pressure, the QCM stability was typically $\pm$ 0.5 Hz, much less ($<$ 0.01%) than the mass initially deposited onto the crystal surface during preparation of the alkane films.

### 4.2.3 Flow system

OH radicals were generated in a flow tube 30 cm in total length, constructed of glass and coated with halocarbon wax on the interior wall to prevent heterogeneous radical loss. Experiments were performed at room temperature (295 K) and a pressure $P_{FT}$ = 100 Torr with an average gas flow velocity 1000 – 2000 cm/s. The CI region and FT pressures were monitored with MKS capacitance manometers (100 and 1000 Torr full scale). Gas flows were monitored with calibrated mass flow meters (Matheson, Tylan) and gases were of UHP quality unless otherwise noted. The rate constants for termolecular reactions were calculated at 100 Torr from the low ($k_0$) and high-pressure ($k_\infty$) rate limits according to the equation given by Troe (1979) to characterize the fall-off region:

$$k = \frac{k_o[M]}{1+\frac{k_o[M]}{k_\infty}} 0.6^{\left(1+log\left(\frac{k_o[M]}{k_\infty}\right)^2\right)^{-1}} \tag{4.29}$$

A microwave discharge (MWD) of $H_2$ diluted in He was used to generate H radicals for OH production in one of three different reaction schemes: titration with $NO_2$, $O_2$ (via a two-step reaction), or $O_3$:

$$H + NO_2 \rightarrow OH + NO \tag{4.30}$$

$$H + O_2 + M \rightarrow HO_2 + M \tag{4.31}$$

$$H + HO_2 \rightarrow 2OH \tag{4.32}$$

$$H + O_3 \rightarrow OH + O_2 \tag{4.33}$$

($k_{4.30} = 1.3{\cdot}10^{-10}$ cm$^3$/molec/s, $k_{4.31} = 1.3{\cdot}10^{-13}$ cm$^3$/molec/s, $k_{4.32} = 7.2{\cdot}10^{-11}$ cm$^3$/molec/s, $k_{4.33} = 2.9{\cdot}10^{-11}$ cm$^3$/molec/s; (JPL, 2003)). The above reactions can lead to production of vibrationally excited OH radicals, however the relaxation times ($\tau \sim 15$ $\mu$s) (D'Ottone et al., 2004) are short compared to the flow tube residence time ($\tau_{FT} \sim 20$ ms). A flow of $N_2/O_2$ carrier gas was introduced immediately downstream of the OH production region both to transport the reactants and to dilute a high local radical concentration in order to

prevent OH loss from secondary reactions:

$$OH + NO_2 + M \rightarrow HNO_3 + M \quad (4.34)$$

$$OH + O_3 \rightarrow HO_2 + O_2 \quad (4.35)$$

($k_{4.34} = 3.5 \cdot 10^{-12}$ cm$^3$/molec/s, $k_{4.35} = 7.3 \cdot 10^{-14}$ cm$^3$/molec/s; (JPL, 2003)). The choice of OH production source allowed us to investigate possible effects of $NO_x$ on the oxidation mechanism to assess potential differences relevant to rural ($NO_x$-poor) vs. urban ($NO_x$-rich) environments. Ozone was generated from $O_2$ with an ozonizer (OREC) and briefly trapped in silica gel at $-70$°C in order to prepare a $O_3$/He mixture. $NO_2$ (99.8%, Praxair) was introduced into the flow tube from a prepared $NO_2$/He mixture. Ultraviolet-visible (UV-vis) spectra of prepared $NO_2$/He mixtures were recorded to verify the purity and mixing ratio for CIMS calibration. The $NO_2$ concentration was calculated from the Beer-Lambert law, $A = \sigma bc$, where A is the measured absorbance at $\lambda = 415$ nm ($\sigma_{415nm} = 5.892 \cdot 10^{-19}$cm$^2$ (Mérienne et al., 1995)) through a 10.0 cm quartz cell.

The CIMS signal was calibrated by introducing a known amount of $NO_2$ to the flow tube and recording the corresponding $NO_2^-$ ion (m/z 46) intensity. The concentration of OH generated in the flow tube was determined by monitoring the $OH^-$ signal (m/z 17) dependence on $NO_2$; typical calibration plots are shown in Figure 4-5.

The $N_2/O_2$ mixing ratio was adjusted to maintain a constant flow velocity while varying $O_2$ from $\sim 10^{12}$ molec/cm$^3$ (ppm impurity in $N_2$) to $2 \cdot 10^{18}$ molec/cm$^3$. In the H + $NO_2$ and H + $O_3$ reaction schemes, the $NO_2$ or $O_3$ flow was varied to optimize OH by efficiently titrating H radicals to suppress formation of $HO_2$ radicals (Reaction 4.31) which react efficiently with OH:

$$OH + HO_2 \rightarrow H_2O + O_2 \quad (4.36)$$

($k_{4.36} = 1.1 \cdot 10^{-10}$ cm$^3$/molec/s; (JPL, 2003)).

In several experiments, concentrations of NO independent of the OH source were introduced by adding a small amount of NO (0.982% in $N_2$, Praxair) into the main carrier gas flow. Higher concentrations of $NO_2$ in the flow tube were also established in this way, such that the dilution by the carrier gas inhibited secondary $HNO_3$ production by reaction with OH.

$SF_6^-$ was used as the parent ion for CIMS detection with the following charge-transfer

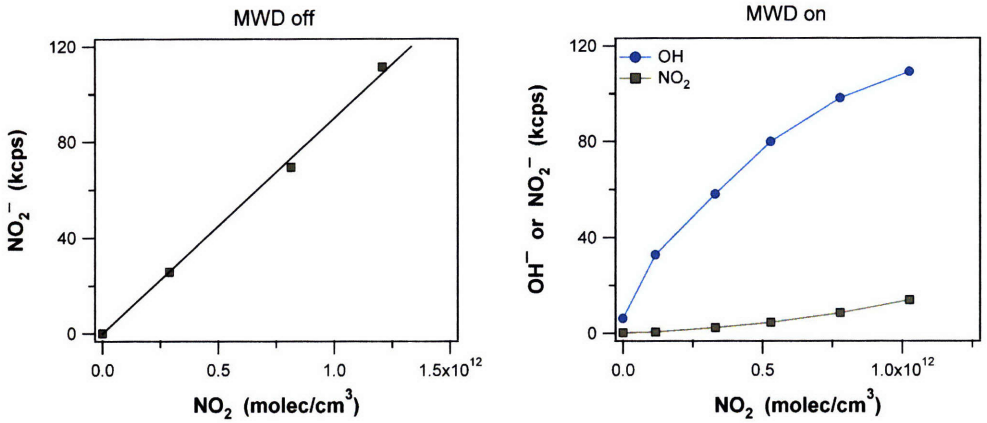


Figure 4-5: CIMS calibration plots for $NO_2$ (left) and OH (right). OH is produced by H + $NO_2$ → OH + NO where H atoms are generated by a microwave discharge (MWD). The linear portion of the $OH^-$ signal vs. $NO_2$ was used to determine its CIMS sensitivity; non-linear OH at increasing $NO_2$ arises as H atoms are titrated and/or secondary reactions. The linear fits obtained are: y = $9.0{\cdot}10^{-11}$x, $R^2$ = 0.99 ($NO_2$); y = $1.9{\cdot}10^{-10}$x, $R^2$ = 0.98 (OH).

reactions:

$$SF_6^- + OH \rightarrow SF_6 + OH^- \tag{4.37}$$

$$SF_6^- + NO_2 \rightarrow SF_6 + NO_2^- \tag{4.38}$$

($k_{4.37}$ = $2{\cdot}10^{-9}$ $cm^3$/molec/s, $k_{4.38}$ = $1.4{\cdot}10^{-10}$ $cm^3$/molec/s; (Lovejoy et al., 1990; Huey et al., 1995)). A calculation of $k_{4.37}$ by average dipole orientation (ADO) theory gives $k_{4.37}$ $1.7{\cdot}10^{-9}$ $cm^3$/molec/s, in agreement with the above estimate by Lovejoy et al. (1990). CIMS detection sensitivities for $NO_2$ and OH at S/N = 1 were $3{\cdot}10^9$ molec/$cm^3$ and $1.5{\cdot}10^9$ molec/$cm^3$, respectively. A typical CIMS spectrum employing the H + $NO_2$ production source with [$O_2$] = $2{\cdot}10^{18}$ molec/$cm^3$ appears in Figure 4-6. Ignition of the microwave discharge (MWD) produces OH radicals by generating H radicals for titration with $NO_2$. Nitric acid ($HNO_3$) could be detected at m/z 82 ($NO_3^-$HF) or m/z 62 ($NO_3^-$) in case of high OH and $NO_2$ concentrations. A peak at m/z 140 indicates $HO_2$ as $SF_4O_2^-$ (via a multistep reaction) with a detection sensitivity approximately a factor of 10 lower than that for $OH^-$ (Lipson et al., 1999).

Gas flows were alternated between the CIMS and QCM along equal path lengths by

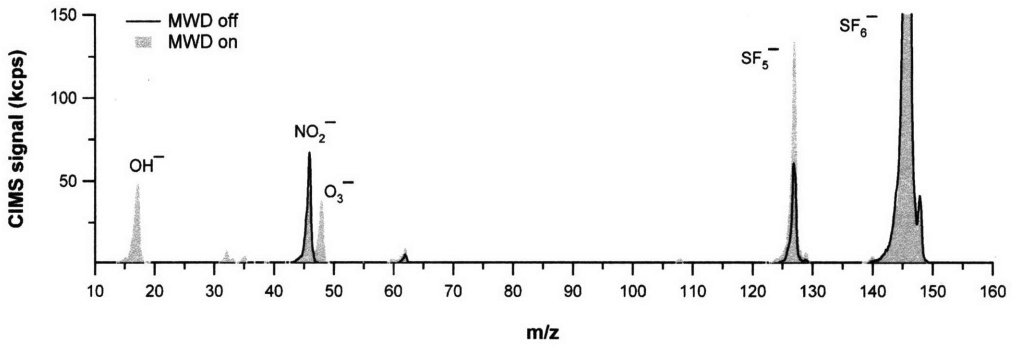


Figure 4-6: CIMS spectrum when using H + $NO_2$ → OH + NO as the OH production source in $[O_2] = 2{\cdot}10^{18}$ molec/cm$^3$ with $SF_6^-$ as the parent ion.

means of Teflon valves (Fig. 4-4). The QCM (Maxtek, Inc.) was incorporated into the flow tube in a custom-made glass cell in which gas-phase reactants were delivered to the organic surface through a 0.25 inch diameter injector positioned 2 mm directly in front of the crystal face. Gas flow conditions created a pressure drop of 5 – 10 Torr between the flow tube and the QCM; studies done ± 5 Torr did not show evidence for a pressure dependence on mass measurement within this range. A water circulator was installed immediately downstream of the microwave cavity with countercurrent flow to control possible temperature interference on QCM measurement upon turning the MWD on/off. Under these conditions, the gas flow temperature increased ≤ 0.3 °C within 10 mins after MWD ignition. Reference studies were done with halocarbon wax films which are known to exhibit low OH reactivity, $\gamma_{OH} = 6{\cdot}10^{-4}$ (Bertram et al., 2001). No net change in mass was observed upon exposing the films to OH, thereby confirming that external artifacts were minimal and did not affect QCM measurement.

### 4.2.4 Sample preparation and characterization

Thin films of hexatriacontane ($C_{36}H_{74}$) (Aldrich, 98%), triacontane ($C_{30}H_{62}$) (Alrich, 99%), tetracosane ($C_{24}H_{50}$) (Aldrich, 99%), paraffin wax (mp = 130–135°C, Sargent-Welch), tricontanoic acid ($CH_3(CH_2)_{28}COOH$) (Aldrich, 98%), azelaic acid ($HOOC(CH_2)_7COOH$) (Aldrich, 98%), glutaric acid ($HOOC(CH_2)_3COOH$) (Aldrich, 99%), and halocarbon wax (600 series, Halocarbon) were prepared by melting a small amount of the solid onto the crystal face. Film thicknesses typically ranged from 3 to 7 $\mu$m calculated from the total frequency shift relative to the uncoated crystal, further confirmed by profilometry measure-

ments (Dektak 3030). The organic films were smooth and assumed to be semi-crystalline. Nonacosane ($C_{29}H_{60}$) (Aldrich, 99%) films prepared in a similar manner were characterized by a more irregular morphology. Self-assembled monolayers of octadecanethiol (ODT, $C_{18}H_{23}SH$) (Aldrich, 99%) were prepared directly onto the QCM crystals according to the procedure given by Ishida et al. (1997). The purity of the ODT films was verified by X-ray Photoelectron Spectroscopy (XPS). Methane soot was deposited directly by holding a crystal 4 – 5 inches above a methane flame for several minutes at which point the crystal surface was brownish-black in appearance. Exploratory studies were done with pyrene ($C_{16}H_{10}$) (Aldrich, 98%) by melting the solid onto the crystal surface.

For all samples the total surface area of the crystal face was 1.53 $cm^2$; upon loading the crystal into the QCM holder the exposed area was 0.5 $cm^2$.

## 4.3 Results on OH-initiated oxidation of an alkane surface

The QCM–CIMS experiments consisted of measuring the OH concentration via CIMS both before and after monitoring the heterogeneous reaction with the QCM. Reproducibility in the OH signal upon turning the MWD on/off was verified prior to exposing the films to OH radicals. Data from a typical experiment appears in Figure 4-7 for a $C_{36}H_{74}$ thin film exposed to OH at 100 Torr in the presence of $[O_2] = 2{\cdot}10^{18}$ molec/$cm^3$ with H $+NO_2 \rightarrow$ OH + NO used as source of OH radicals.

The experimental procedure was as follows: upon recording the OH signal via CIMS, the MWD was turned off and gas flows were switched to the QCM whereby a stable frequency baseline was reached within several minutes. No mass change within error of QCM measurement was detected for unoxidized films exposed to $NO_2$ or $O_3$. The MWD was then turned on to initiate radical production and OH was exposed to the organic surface for 20 to 30 mins. A linear $\Delta$freq/time rate ($\propto$ $\Delta$mass/time) was generally established within 5 to 10 mins; a steady-state rate was determined by applying a least-squares linear fit to the data beginning 10 mins after turning on the MWD to begin OH production. The MWD was then turned off to terminate the OH exposure and the QCM frequency monitored for an additional 10 to 20 mins before returning the gas flows to the CIMS for a secondary check of the OH signal. Variability in the OH measured before and after reaction was within 5 to 10%.

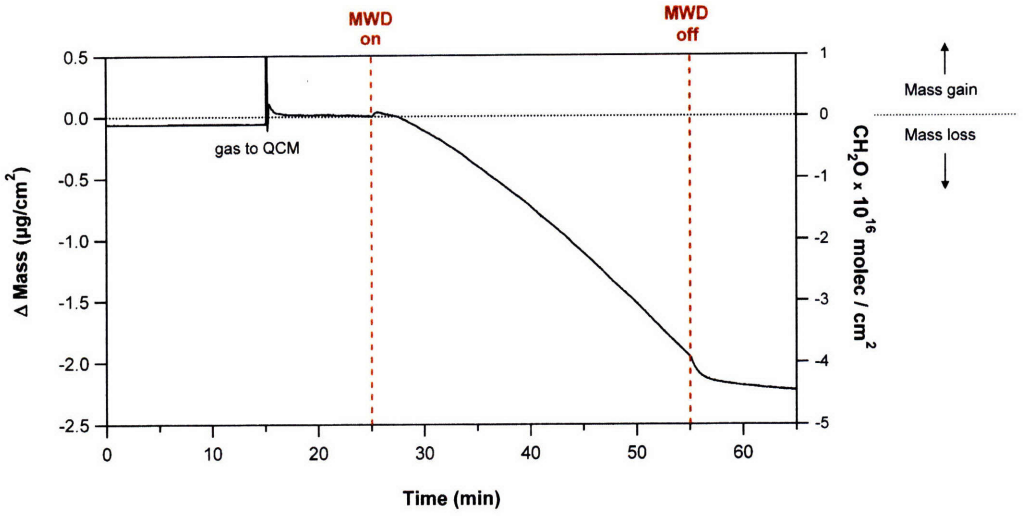


Figure 4-7: QCM measurement of mass loss by a $C_{36}H_{74}$ thin film upon exposure to OH at 100 Torr in the presence of $[O_2] = 2{\cdot}10^{18}$ molec/cm$^3$. The reaction H + $NO_2$ $\rightarrow$ OH + NO was used as the OH production source with H radicals produced by ignition of a microwave discharge (MWD). The right-hand axis displays the equivalent mass change in units of $CH_2O$ molecules per cm$^2$.

### 4.3.1 OH–surface calibration

High pressure diffusion limitations necessitated calibration studies to determine the OH concentration available for reaction at the QCM surface. This was done experimentally by comparing the lifetime of an ODT monolayer to that of octadecyltrichlorosilane (OTS) previously quantified by Molina et al. (2004) at low pressure conditions ($P_{FT} < 2$ Torr). Both ODT and OTS are $C_{18}$ alkane self-assembled monolayers and thus expected to exhibit comparable OH reactivity.

To match the conditions employed by Molina et al. (2004), QCM studies were done in $[O_2] = 3{\cdot}10^{16}$ molec/cm$^3$ and OH radicals were generated by H + $NO_2$ $\rightarrow$ OH + NO. Figure 4-8 shows the QCM data of $\Delta$mass/time where the left-hand axis gives the QCM-measured mass and the two right-hand axes provide the equivalent mass in units of $CH_2O$ molecules per cm$^2$, and surface $O_2$ molecules assuming $8{\cdot}10^{14}$ sites/cm$^2$. Based on the measured ODT monolayer lifetime $\tau_{ODT} \sim 20$ mins (the time at which a plateau was reached to indicate monolayer depletion), the OH concentration near the surface was on the order of 0.5 – $1{\cdot}10^7$ cm$^{-3}$. The ratio of the OH concentration available for reaction at the surface to that measured in the flow tube by CIMS, $[OH]_{QCM}/[OH]_{FT}$ is denoted $\alpha_{OH} = 1.25{\cdot}10^{-4}$ and

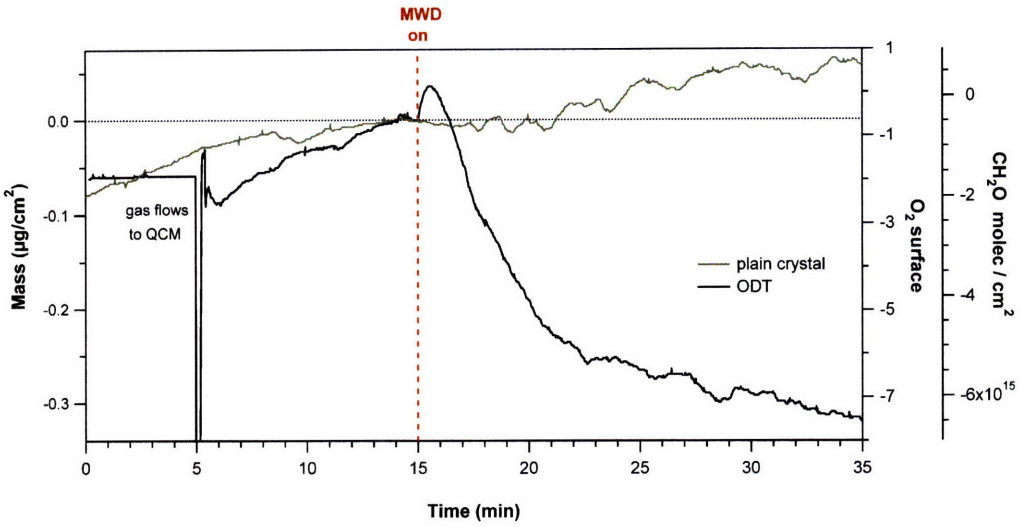


Figure 4-8: Mass loss by an ODT monolayer ($C_{18}$ alkane). The right-hand axis shows the equivalent number of surface $O_2$ molecules assuming $8{\cdot}10^{14}$ reactive sites/cm$^2$; the far right-hand axis expresses the mass change in equivalent $CH_2O$ molecules per cm$^2$. OH exposure was initiated by turning on the microwave discharge; data for a plain, uncoated crystal are shown for comparison.

was used in subsequent experimental and modeling analyses. The OH collision frequency leading to surface reaction may therefore be described by the following:

$$\gamma_{\mathrm{OH}} \cdot u_{\mathrm{OH}} \cdot [OH]_{\mathrm{QCM}} = \gamma_{\mathrm{OH}} \cdot \sqrt{\frac{RT}{2\pi M}} \cdot \alpha_{\mathrm{OH}} [OH]_{\mathrm{FT}} \tag{4.39}$$

where $u_{\mathrm{OH}}$ is the thermal velocity in the x-direction, $u_{\mathrm{OH}} = 1/4 \cdot c_{\mathrm{OH}}$. The mass volatilized from the ODT surface was $\sim 350$ ng/cm$^2$, or $\sim 8{\cdot}10^{14}$ $C_{18}H_{38}$ molec/cm$^2$, which is consistent with the expected density of reactive sites in a self-assembled alkane monolayer film (Ulman, 1991).

### 4.3.2 Role of $O_2$ in alkane oxidation

A major objective of this study was to assess decomposition as a potential removal mechanism for organic aerosol (employing organic films as proxy surfaces) by OH-initiated oxidation in the presence of $O_2$ concentrations relevant to the troposphere. For the $C_{36}H_{74}$ films used in the majority of our experiments, mass loss was observed upon exposure to OH for all $O_2$ concentrations. The mass loss rates were linearly dependent on OH and independent of $O_2$ within experimental error, summarized in Figure 4-9. The effects arising

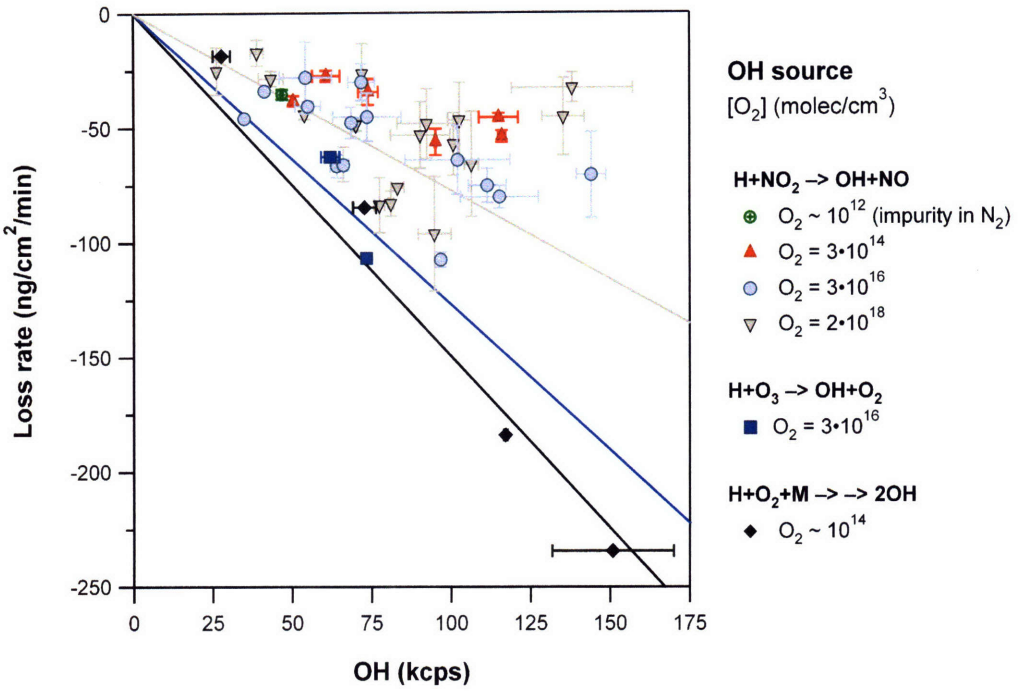


Figure 4-9: Mass loss by $C_{36}H_{74}$ thin films as a function of exposure to OH and $O_2$. Three different reaction schemes were used for OH production; the linear fits constrained through the origin are: y = -0.77x, $R^2$=0.68 (H + $NO_2$), y = -1.49x, $R^2$=0.99 (H + $O_2$ + M), y = -1.27x, $R^2$=0.99 (H + $O_3$).

from $NO_x$ will be discussed in Section 4.3.3, below. The error bars in the OH concentration represent the standard deviation in CIMS measurement of OH generated before and after the heterogeneous reaction monitored by the QCM; concentrations have been normalized to the intensity of the $SF_6^-$ parent ion signal. Error bars in the QCM-measured mass loss rates represent the deviation from the average rate within the entire reaction period, beginning 10 minutes after initial exposure to OH. Least-squares linear fitting of the mass loss rate vs. OH concentration for each OH production source were determined for [OH] $\leq$ 100 kcps relevant to atmospheric concentrations with the following linear fits constrained through the origin: y = -0.77x, $R^2$=0.68 (H + $NO_2$), y = -1.49x, $R^2$=0.99 (H + $O_2$ + M), y = -1.27x, $R^2$=0.99 (H + $O_3$). Figure 4-10 compares the mass loss rates obtained in the H + $NO_2$ $\rightarrow$ OH + NO scheme as a function of $O_2$ concentration for a given OH; no $O_2$ dependence was observed over the range $O_2 \sim 10^{12}$ to $2{\cdot}10^{18}$ molec/cm$^3$.

It should be emphasized that the QCM measures a *net* mass change; within the context of the present discussion this includes release of carbon-containing products into the gas

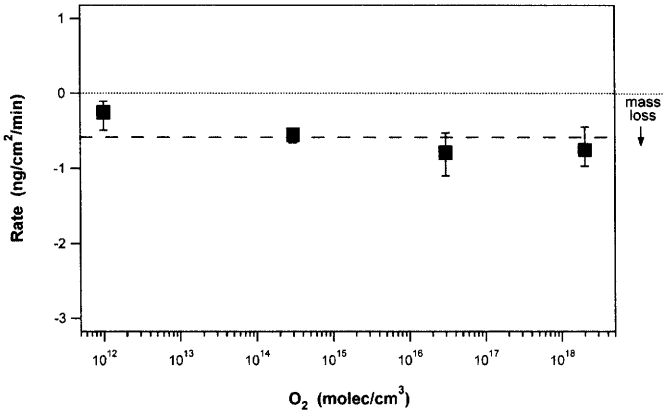


Figure 4-10: Comparison of mass loss rate by $C_{36}H_{74}$ thin films as a function of $O_2$ concentration for a given OH produced by $H + NO_2 \rightarrow OH + NO$. The rate is independent of $O_2$ concentrations (dashed line) over the range $O_2 \sim 10^{12}$ to $2{\cdot}10^{18}$ molec/cm$^3$.

phase as well as $O_2$ and/or $NO_x$ addition to the organic surface. Evidence for surface attachment was shown by a small mass increase typically observed within the first 30 seconds of reaction. In the case the ODT monolayer, the magnitude of the mass increase ($\sim$ 60 ng/cm$^2$) is consistent with monolayer $O_2$ attachment anticipated by the reaction $R^{\cdot}_{(s)} + O_{2(g)} \rightarrow RO_{2(s)}$ (Fig. 4-8). Kinetic modeling was done to compare the oxidation of ODT and OTS films as described in Section 4.3.4.

An interesting feature detected by the QCM was a sudden mass loss from the surface of the organic films immediately following OH exposure, in absence of OH. This phenomenon was observed when employing $H + NO_2 \rightarrow OH + NO$ as the OH production source in $[O_2] \geq 10^{16}$ molec/cm$^3$, and to a somewhat lesser degree in the $NO_x$–free system, $H + O_2 + M \rightarrow 2OH + M$, where $[O_2] = (0.5 - 1){\cdot}10^{14}$ molec/cm$^3$. The effect was slight when using $H + O_3 \rightarrow OH + O_2$; additional data would be necessary to compare with the other two reaction schemes for a wider range of OH concentrations. The effect was greatest for the $H + NO_2$ system; the amount of mass released from the surface after OH exposure was proportional to the OH concentration during exposure, shown in Figure 4-11. Three possible explanations for this observation are proposed:

1. OH attack results in a stoichiometric number of surface $R^{\cdot}_{(s)}$ radicals (hence $RO_2^{\cdot}{}_{(s)}$ and $RO^{\cdot}_{(s)}$ radicals in $O_2$) under steady-state conditions. The $RO^{\cdot}_{(s)}$ and $RO_2^{\cdot}{}_{(s)}$ radicals on the surface react analogously to gas-phase oxidation (Sec. 4.1.1) where the sudden mass release follows from the fact that turning off the MWD effectively limits

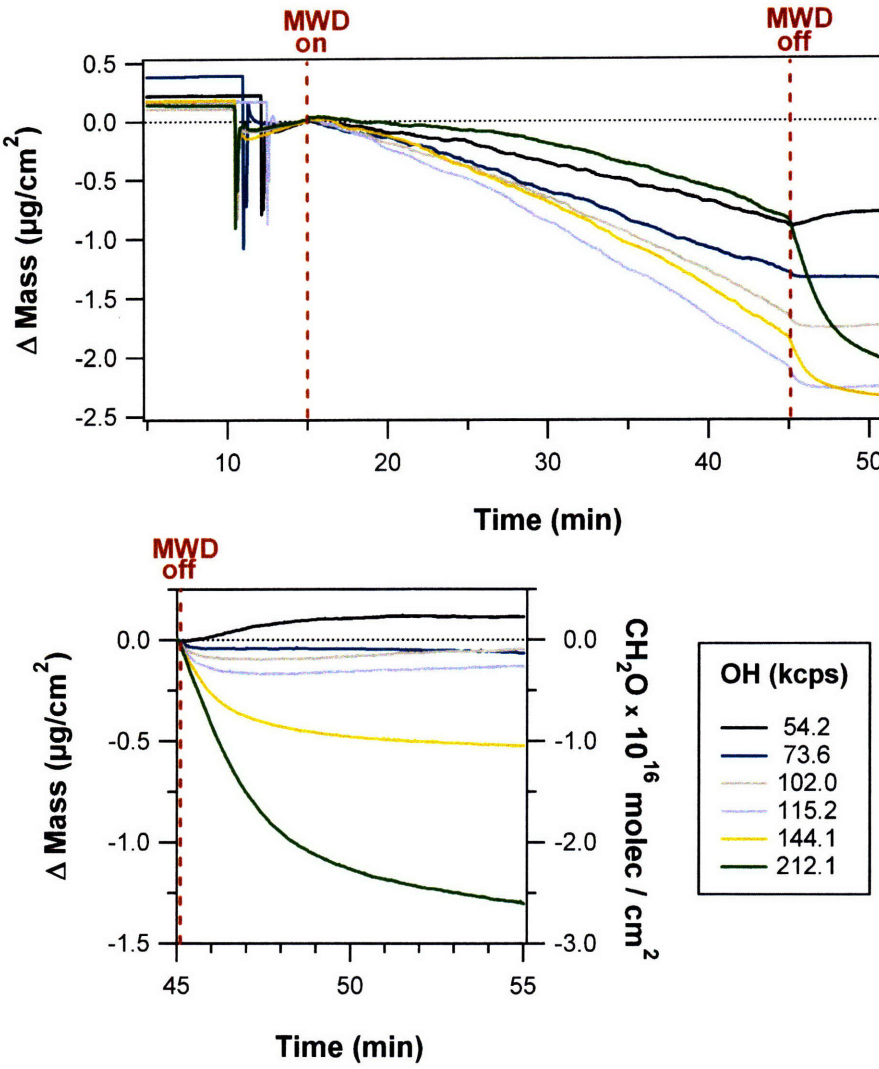


Figure 4-11: Mass loss by $C_{36}H_{74}$ thin films immediately following exposure to OH radicals. The bottom panel shows that mass loss observed after stopping OH production by turning off the MWD is proportional to the OH concentration during exposure.

continuous mass gain by $R^{\cdot}_{(s)} + O_{2(g)} \rightarrow RO^{\cdot}_{2(s)}$ and only mass loss by $RO^{\cdot}_{(s)}$ decomposition is detected by the QCM (neglecting H loss from release of $HO_2$, Reaction 4.22);

2. As the parent alkane molecule volatilizes through successive fragmentation, the vapor pressure of surface products increases to the point at which molecules can parition into the gas phase, most apparent when the steady-state surface attachment of $O_2$ (following OH-attack to form surface $R^{\cdot}$) stops;

3. In presence of $NO_x$, alkyl nitrate ($RONO_2$) or peroxynitrate ($RO_2NO_2$) compounds are formed on the surface in a quasi-stable state that decompose at ambient temperatures, releasing mass into the gas phase.

The latter two arguments are supported by experimental observations that mass loss could be observed for up to 1 hr after exposure to high OH concentrations. Limitations to the QCM–CIMS experimental approach prohibited identification of gas-phase products (small surface area afforded by the QCM crystal and CIMS detection limits); a combination of the above explanations seems feasible. In previous experiments by Molina et al. (2004), it was found that the reaction products from the OH-initiated oxidation of paraffin wax films consisted primarily of CO, $CO_2$, $CH_2O$, $CH_3CO$, $CH_3OH$, and HCOOH. It was therefore concluded that surface decomposition through C−C bond scission proceeds successively through $C_1$ and $C_2$ fragments. The CIMS sensitivities for longer chain fragments and/or other reaction products may have been too low for their detection, however.

To explore the possibility for increased vapor pressure of surface molecules as a result of fragmentation into shorter molecules, the volatiliation of several unoxidized alkane films were studied. Figure 4-12 shows mass loss by $C_{18}H_{38}$, $C_{24}H_{50}$, and paraffin wax films at a pressure of 1 Torr. Measurements were recorded upon reducing the pressure from atmosphere (756 Torr) to 1 Torr by opening the valve leading from the QCM cell exhaust to a vacuum pump. The initial loss rates measured for the films were $\sim$ 100 $\mu g/cm^2/min$ for $C_{18}H_{38}$, 0.180 $\mu g/cm^2/min$ for paraffin wax, and 0.06 $\mu g/cm^2/min$ for $C_{24}H_{50}$.

Analysis by gas chromotography–mass spectrometry (GC–MS) shows that paraffin wax consists of a mixture of *n*-alkanes primarily $C_{20}$ to $C_{33}$ (G. Poskrebyshev, personal communication). This agrees with the fact that freshly-prepared paraffin wax samples exhibited a volatility between that of $C_{18}H_{38}$ and $C_{24}H_{50}$. Under flow conditions at 100 Torr, the

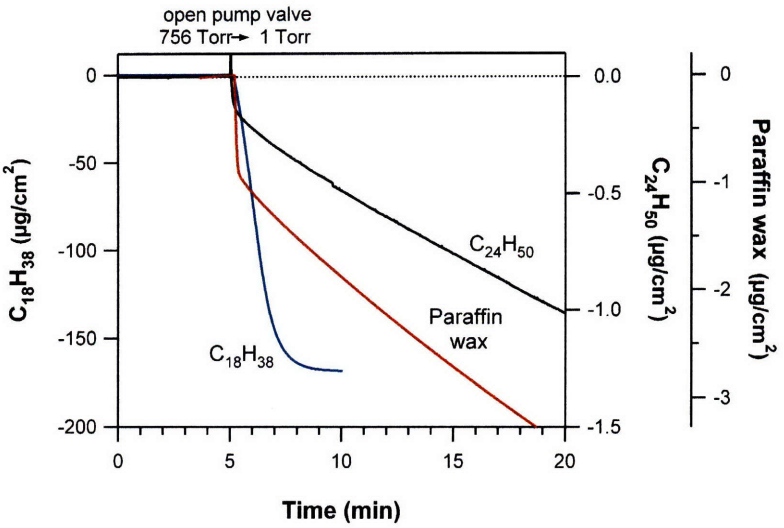


Figure 4-12: Volatilization of unoxidized alkane films at 1 Torr.

volatilization of a freshly-prepared paraffin wax sample was measured at a rate 5 to 6 times slower than at 1 Torr; $C_{24}H_{50}$ films were non-volatile at 100 Torr. Pumping paraffin wax films overnight at 1 Torr was sufficient to remove shorter-chain molecules in order to establish a steady baseline prior to performing OH-reactivity experiments. Loss of alkyl fragments $\leq C_{18}$ appears likely under flow conditions such that the loss of 18 $CH_2O$ molecules via $RO\cdot$ decomposition could result in loss of an entire $C_{36}H_{74}$ parent molecule. Simultaneous formation of surface C−O groups such as ketones or carboxylic acids would likely lower the vapor pressure, however.

### 4.3.3 Effect of $NO_x$

The presence of $NO_x$ resulted in a slower net volatilization of $C_{36}H_{74}$ films upon OH exposure as shown in Figure 4-9. Closer examination of the time-dependent mass change measured for individual experiments reveals important differences. Figure 4-13 shows the mass change of $C_{36}H_{74}$ films exposed to OH in both the presence and absence of $NO_x$ with [OH] = 72 – 77 kcps. An average Δmass/time rate was determined in each case by applying a linear fit approximation to the data corresponding to the period 10 – 20 mins after the onset of OH exposure. The following rates were obtained: -82.9 ± 12.1 ng/cm$^2$/min (H + $NO_2$); -84.4 ± 0.4 ng/cm$^2$/min (H + $O_2$ + M); -103.2 ± 7.1 ng/cm$^2$/min (H + $O_3$). Significant curvature (i.e., deviation from a linear Δmass/time rate) was commonly observed in all

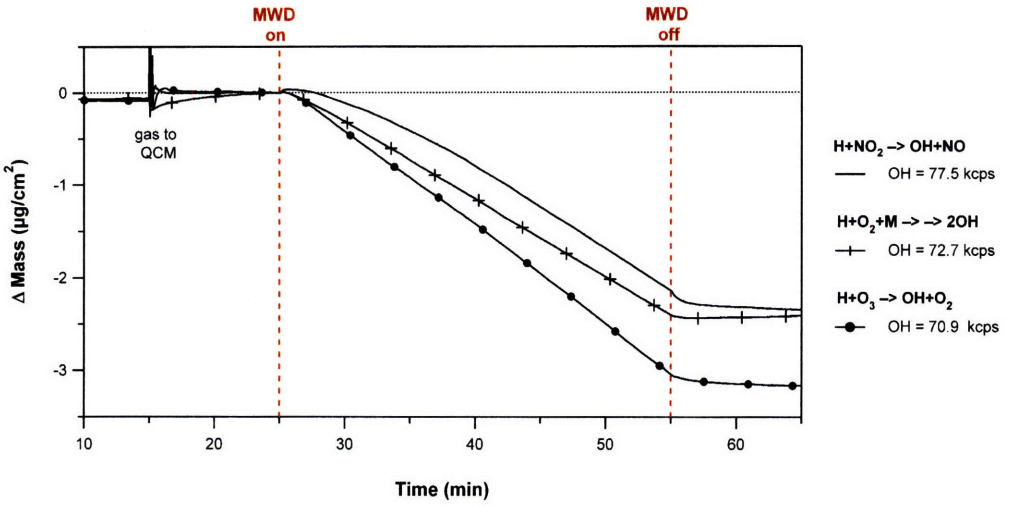


Figure 4-13: Mass loss by $C_{36}H_{74}$ thin films for comparison of reaction schemes used in OH production: $[O_2] = 2{\cdot}10^{18}$ molec/cm$^3$ and $[NO_2] = 6{\cdot}10^{11}$ molec/cm$^3$ (H + $NO_2$); $[O_2] = 10^{14}$ molec/cm$^3$ (H + $O_2$ + M); $[O_2] = 3{\cdot}10^{16}$ molec/cm$^3$ and $[O_3] = 7{\cdot}10^{12}$ molec/cm$^3$ (H + $O_3$).

experiments employing H + $NO_2$ → OH + NO as the OH production source, suggesting a gradual acceleration or initial suppression in the volatilization rate.

Non-linear behavior for the QCM–measured mass loss rate vs. OH in the presence of $NO_x$ ($0.1–1{\cdot}10^{12}$ molec/cm$^3$) is evident for OH concentrations > 100 kcps, in contrast to the $NO_x$–free regimes, shown in Figure 4-9. Given that this behavior was specific to $NO_x$ conditions, the most likely explanations include formation of alkyl nitrate or peroxynitrate compounds during surface oxidation, and/or adsorption of $HNO_3$ produced with increasing OH and $NO_2$ concentrations.

Nitric acid is readily detected in negative mode CIMS with $SF_6^-$ parent ions with a detection sensitivity on the same order as OH (Huey et al., 1995). Peaks at m/z 62 ($NO_3^-$) and/or m/z 82 ($NO_3^-HF$) were observed in the background CIMS spectrum as a result of passing the $N_2/SF_6$ flow through the $^{210}$Po source to generate $SF_6^-$ ions for all experiments. Employing the H + $NO_2$ → OH + NO reaction as OH production source resulted in a small increase above the background signals (5 – 10 kcps) which was generally no greater than 5% of the OH signal. Flow conditions were optimized such that only a small excess of $NO_2$ was necessary in most cases to prevent substantial $HO_2$ production leading to OH radical loss, or leading to secondary $HNO_3$ formation. A negative dependence for mass loss

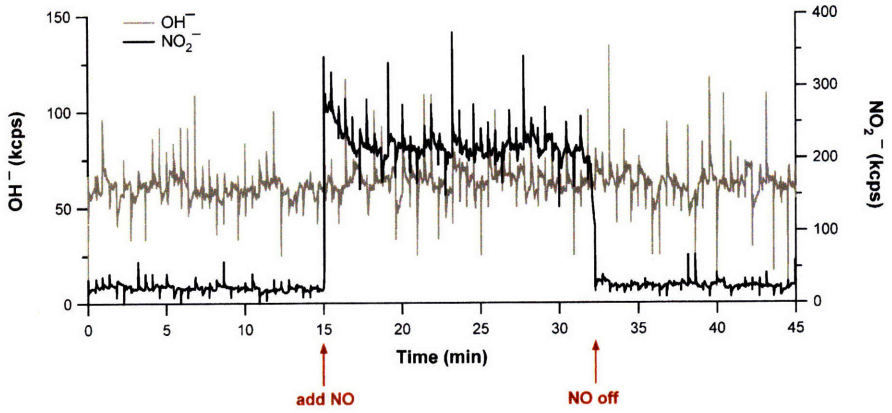


Figure 4-14: CIMS detection of $OH^-$ and $NO_2{}^-$ upon addition of [NO] = $10^{14}$ molec/cm$^3$ when using the H + $NO_2$ → OH + NO source for OH. An $NO_2$ impurity in NO is evident by the increase in the $NO_2{}^-$ signal; the $OH^-$ signal remains unchanged.

rate vs. $HNO_3$ at these concentrations was not observed as would be expected if surface adsorption of $HNO_3$ were responsible for the non-linear behavior.

Formation of alkyl nitrate or peroxynitrate compounds during heterogeneous oxidation of organics would be consistent with gas-phase data showing higher nitrate yields with increasing alkane chain length (Arey et al., 2001; Lim and Ziemann, 2005). To further investigate the role of $NO_x$ in the oxidation mechanism, several experiments were done in elevated NO and $NO_2$ concentrations independent of the OH production source. For these studies [$O_2$] = $3{\cdot}10^{16}$ molec/cm$^3$ and H + $NO_2$ → OH + NO was used as the OH production source.

NO was introduced into the main carrier gas flow from a calibrated mixture of 0.982% NO in $N_2$ containing a ~ 1% impurity of $NO_2$ (Praxair). Although NO may not be detected via CIMS in the negative mode, its introduction into the flow tube was signaled by an abrupt increase in $NO_2{}^-$, shown in Figure 4-14. The $OH^-$ ion was monitored simultaneously to ensure that the OH radical concentration remained constant and independent of the added $NO_x$.

The QCM mass change data for a $C_{36}H_{74}$ film exposed to OH with [NO] = $10^{14}$ molec/cm$^3$; [$NO_2$] = $1.2{\cdot}10^{12}$ molec/cm$^3$ are shown in Figure 4-15 where the mass loss rate was slowed by a factor of 2 – 3 in the higher $NO_x$ concentrations. Upon ignition of the MWD in Figure 4-15, shown more clearly in Figure 4-16, a distinct mass gain of 125 – 250

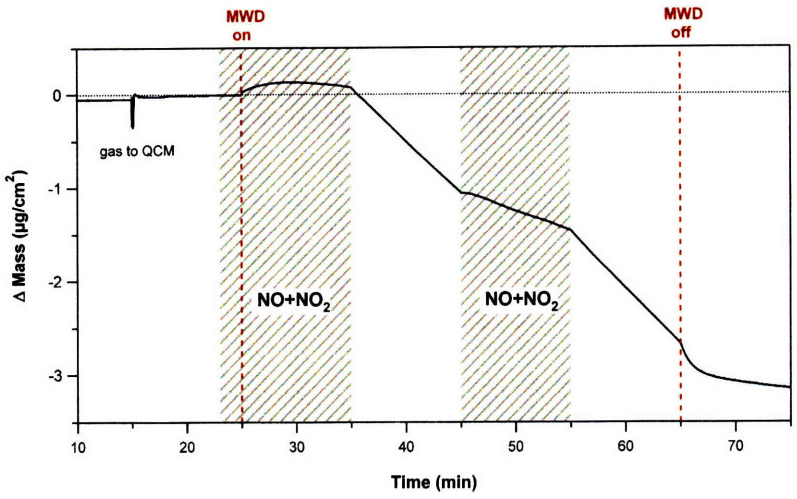


Figure 4-15: Effect of increased $NO_x$ on OH-oxidation of $C_{36}H_{74}$. The shaded area indicates when [NO] = $10^{14}$ molec/cm$^3$ was added with [$NO_2$] $\sim 1.2 \cdot 10^{12}$ molec/cm$^3$. The loss rates measured by QCM with [OH] = 65 kcps were: -115 $\pm$ 5 ng/cm$^2$/min and -43 ng/cm$^2$/min (added $NO_x$).

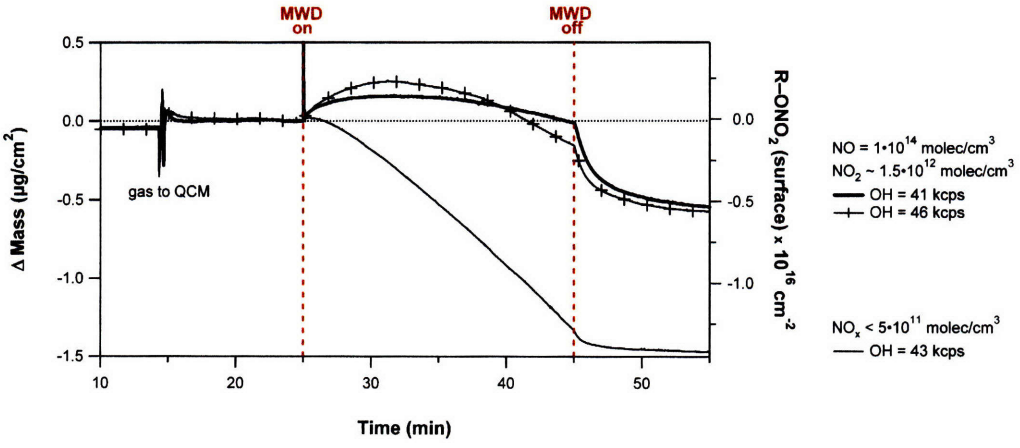


Figure 4-16: Mass change of a $C_{36}H_{74}$ film upon exposure to OH in elevated $NO_x$ concentrations.

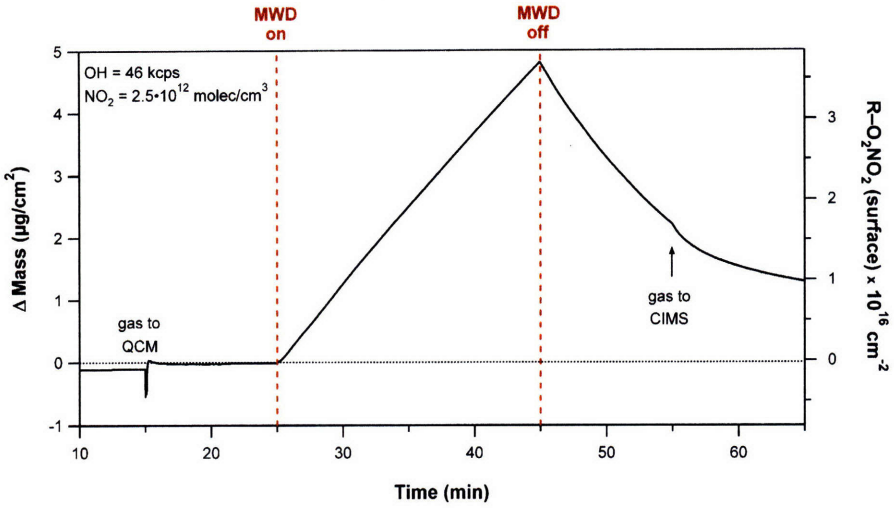


Figure 4-17: Mass change of a $C_{36}H_{74}$ film upon exposure to OH in elevated $NO_2$.

ng/cm$^2$ was detected within the first 5 to 10 mins of OH exposure. The right-hand axis in Figure 4-16 displays the measured mass change in equivalent $-ONO_2$ groups per cm$^2$ for comparison purposes. Converting this mass entirely to addition of $O_2$ and $NO_x$ as nitrate ($-ONO_2$) or peroxynitrate ($-O_2NO_2$) groups gives a density of (1–2.4)·$10^{15}$ cm$^{-2}$, which is reasonable within a factor of 2 to 3 for surface coverage of an alkane film. Surface decomposition likely occurs simultaneously, however, requiring a system of rate equations to describe the contribution of individual surface addition/decomposition reactions (see Sec. 4.3.4). After this initial period, the measured gain led into a continuous net loss where the curvature in $\Delta$mass/time is consistent with previously-discussed experiments done under lower $NO_x$ conditions (Fig. 4-13).

Because of the $NO_2$ impurity in NO, it was not clear if the mass gain detected on the oxidized alkane surface could be attributed to reactivity with NO or $NO_2$ reactivity, or a combination of both. Studies were therefore done in a relatively high $NO_2$ environment, $[NO_2] = 2.5{\cdot}10^{12}$ molec/cm$^3$, where $[NO] \sim [OH] < 3{\cdot}10^{11}$ molec/cm$^3$ as produced from H + $NO_2 \rightarrow$ OH + NO. Despite the dilution allowed by introducing $NO_2$ in the carrier gas region, substantial $HNO_3$ production was detected under these conditions. Based on the intensity of the m/z 62 peak upon ignition of the MWD, we estimate the $HNO_3$ concentration in the flow tube was $\sim$ 40% greater than OH and roughly an order of magnitude higher than previous experiments.

Shown in Figure 4-17, a $C_{36}H_{74}$ film exposed to OH under these conditions exhibited a sharp, continuous mass gain (230 ng/cm$^2$/min) which was immediately reversed (-270 ng/cm$^2$/min) upon stopping the OH exposure by turning off the MWD. This rate roughly translates to addition of $2{\cdot}10^{15}$ $-O_2NO_2$ groups per cm$^2$ where multilayer processes could be possible. These data suggest that $NO_2$ adds more efficiently to the surface than NO to form peroxynitrate compounds which thermally decompose with lifetimes on the order of seconds to minutes. Considering the increased $HNO_3$ production with high $NO_2$, however, it remains unclear to what degree adsorption/desorption of $HNO_3$ contributes to the observed mass change.

Additional studies would be necessary to investigate the role of NO vs. $NO_2$ in heterogeneous OH-initiated oxidation more thoroughly. Nevertheless, we are able to conclude from our studies that $NO_x$ plays an important role in the mechanism, a role which was not clear from earlier studies (Molina et al., 2004). Rather than converting $RO_2{\cdot}$ radicals to $RO{\cdot}$ with enhanced surface decomposition, it appears that $NO_x$ efficiently adds to the OH-activated surface to inhibit volatilization. Considering that $RO_2{\cdot}$ radicals are more stable than $RO{\cdot}$ radicals, the most likely species present are $RONO_2$ or $RO_2NO_2$ compounds resulting from reaction with NO or $NO_2$, respectively. Nitrogen-containing products were not observed by XPS analysis of the oxidized organic surfaces in (Molina et al., 2004), nor was there a measureable difference in the OH uptake coefficient, $\gamma_{OH}$, in the presence vs. absence of $NO_x$. One possible explanation for this discrepancy include short lifetimes of the surface nitrate compounds prohibiting their detection upon removal from the flow tube reactor. Also, XPS sensitivity may have imposed an additional limitation if only a fraction of surface radicals succeed in nitrate formation.

### 4.3.4 Kinetics modeling of the heterogeneous reaction mechanism

Data obtained from the QCM–CIMS experiments reflects the net result of an extremely complex system of individual reactions. To examine these results in more detail, a comprehensive set of rate equations has been developed to extract individual rate constants in a proposed mechanism (Johnson et al., 2007b). The following describes modeling efforts done in collaboration with Dr. Andrey Ivanov in continuation of earlier studies to describe this system (Molina et al., 2004).

We assume the heterogeneous reaction mechanism is analogous to gas phase oxidation

(Sec. 4.1.1) with the following:

- OH attack (H-abstraction) leads to a reservoir of surface $R^{\cdot}_{(s)}$, $RO^{\cdot}_{(s)}$, and $RO_{2}{}^{\cdot}_{(s)}$ radicals whose concentrations are determined by the diffusion-limited uptake of OH and heterogeneous reaction with $O_2$ and $NO_2$;
- The $RO_{2}{}^{\cdot}_{(s)}$ self-reaction between neighboring molecules is relatively fast;
- The major reaction pathways for $RO^{\cdot}_{(s)}$ radicals are C−C scission, isomerization, and reaction with $O_2$;
- Surface radicals resulting from C−C scission and isomerization are treated as new surface $R^{\cdot}_{(s)}$ radicals;
- No cross-linking occurs (peroxide formation).

Numerical modeling was used to describe the reaction scheme from the perspective of QCM detection, i.e., $O_2$ and $NO_x$ surface attachment, release of carbon-containing fragments resulting from $RO^{\cdot}$ scission, nitrate decomposition, and physical evaporation of shorter-chain products as a result of successive carbon chain scission. The relevant processes are illustrated in Figure 4-18 and rate expressions were taken from the following set of reactions:

$$OH_{(g)} + RH_{(s)} \rightarrow R^{\cdot}_{(s)} + H_2O_{(g)} \tag{4.40}$$

$$R^{\cdot}_{(s)} \leftrightarrow R^{\cdot}_{(s)} \tag{4.41}$$

$$R^{\cdot}_{(s)} + O_{2(g)} \rightarrow RO_{2(s)}^{\cdot} \tag{4.42}$$

$$RO_{2(s)}^{\cdot} + RO_{2(s)}^{\cdot} \rightarrow RO^{\cdot}_{(s)} + RO^{\cdot}_{(s)} + O_{2(g)} \tag{4.43}$$

$$\rightarrow ROH_{(s)} + R'R''C(O)_{(s)} + O_{2(g)} \tag{4.44}$$

$$RO_{2(s)}^{\cdot} \leftrightarrow R'{\cdot}OOH_{(s)} \tag{4.45}$$

$$RO_{2(s)}^{\cdot} + NO_{2(s)} \leftrightarrow RO_2NO_{2(s)} \tag{4.46}$$

$$RO_{2(s)}^{\cdot} + NO_{(s)} \leftrightarrow RONO_{2(s)} \tag{4.47}$$

$$RO^{\cdot}_{(s)} \rightarrow R'^{\cdot}_{(s)} + R''C(O)_{(g)} \tag{4.48}$$

$$\rightarrow R'{\cdot}OH_{(s)} \tag{4.49}$$

$$RO^{\cdot}_{(s)} + O_{2(g)} \rightarrow R'R''C(O)_{(s)} + HO_{2(g)} \tag{4.50}$$

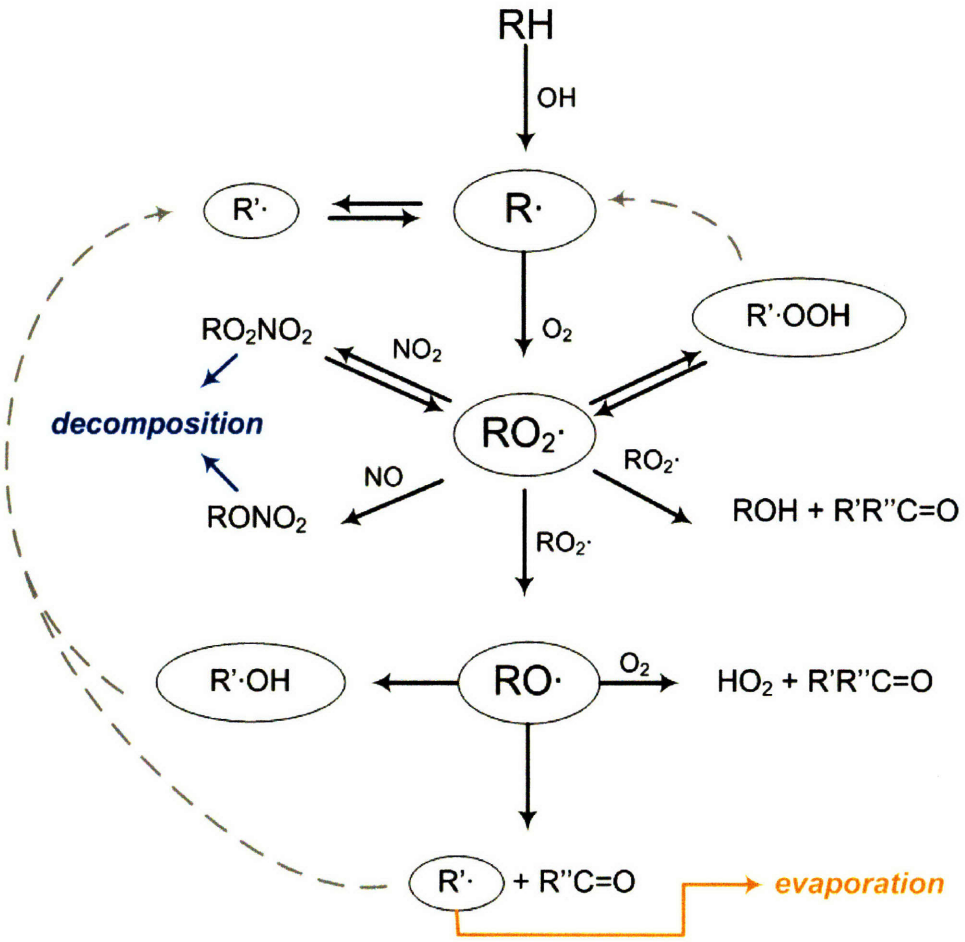


Figure 4-18: Proposed mechanism for heterogeneous OH-initiation oxidation of organic aerosol.

An unknown parameter in our studies was the availability of $O_2$ for reaction within the organic film ($\beta_{OH}$) which becomes important for $R^{\cdot}_{(s)}$ isomerization into the bulk ($k_{4.41} = 2{\cdot}10^4\ s^{-1}$) (Denisov and Afanas'ev, 2005). The value for $\beta_{OH}$ was determined by comparing the rate constant for the heterogeneous reaction $RO^{\cdot}_{(s)} + O_{2(g)}$ measured experimentally by Stepanov et al. (2006) on paraffin wax surfaces ($k_{4.50} = 1.7{\cdot}10^{-17}$ cm$^3$/molec/s) to that recommended for the gas phase reaction ($k_{4.22} = 8{\cdot}10^{-15}$ cm$^3$/molec/s) (Atkinson, 1997b). The value obtained, $\beta_{OH} = 2.1{\cdot}10^{-3}$, compares favorably with measured $O_2$ solubility in the amorphous phase of polymers (Denisov and Afanas'ev, 2005).

The initiation rate from $OH_{(g)} + RH_{(s)}$ is given by the formula of kinetic resistances (Equation 1.5) where $OH_0$ is the initial gas-phase concentration measured by CIMS from which we may determine the OH concentration near the organic surface, $[OH]_{QCM} = \alpha_{OH} \cdot [OH]_{FT}$ with $\alpha_{OH} = 1.25{\cdot}10^{-4}$. The rate constant for $RO_{2(s)}^{\cdot} + RO_{2(s)}^{\cdot}$ self-reaction was determined by analysis of the ODT monolayer experiments and $C_{36}H_{74}$ alkane films within the initial 30 seconds of reaction. Assuming that the mass gain corresponds to monolayer $O_2$ attachment balanced by $O_2$ release, taking the $RO_{2(s)}^{\cdot}$ self-reaction as the rate-determining step, and imposing steady-state conditions for $R^{\cdot}_{(s)}$ gives $k_{4.42} = 2.0{\cdot}10^{-14}$ cm$^2$/molec/s. We note that this value lies within the range of self-reaction rates measured for secondary $RO_2^{\cdot}$ radicals in the gas phase (Atkinson, 1997b).

Analysis of the abrupt surface volatilization detected after removing the OH source (Fig. 4-11) was done to determine values of the rate constant for $R^{\cdot} + O_2 \rightarrow RO_2^{\cdot}$ ($k_{4.41}$), and the three reaction channels for $RO^{\cdot}$ radicals ($k_{4.48}$ to $k_{4.50}$). This approach assumes that the net mass loss detected by QCM during this period is proportional to the contribution of $RO^{\cdot}_{(s)}$ decomposition into gas-phase products (i.e., release of $CH_2O_{(g)}$) where the mass has been normalized. Steady-state conditions were applied for $RO^{\cdot}_{(s)}$ and $RO_{2(s)}^{\cdot}$ radicals with the surface concentration of $R^{\cdot}$ determined by OH-attack and $O_2$ addition to the surface. Fitting the parameters to experimental data yielded the following values: $k_{4.41} = 1.3{\cdot}10^{-11}$ cm$^3$/molec/s, $k_{4.48} = 2.1{\cdot}10^3\ s^{-1}$, $k_{4.49} = 1.8{\cdot}10^2\ s^{-1}$, and $k_{4.50} = 8{\cdot}10^{-15}$ cm$^3$/molec/s.

These results indicate that the heterogeneous $R^{\cdot} + O_2$ reaction is comparable to rates measured in the gas phase upon accounting for $O_2$ solubility within the film. The rate constants obtained for the $RO^{\cdot}$ channels suggest that these reactions proceed more slowly on surfaces than in the gas phase, which may provide evidence for steric restrictions associated with a "rigid cage". This effect may be particularly important for the $RO^{\cdot}$ isomerization

channel which involves preferential formation of a 6-membered transition state. We may compare the diameter of benzene or cyclohexane ($\sim$ 6 Å) to the typical lattice spacing for alkane crystal structures (4 – 5 Å), which suggests that the rate of unimolecular isomerization could be reduced by close proximity to nearest neighbors within a crystalline film. Furthermore, this suggests that the RO· decomposition (C–C bond scission) becomes relatively more important in surface oxidation. The rate of the heterogeneous reaction $RO^{\cdot}_{(s)}$ + $O_{2\,(g)}$ $\rightarrow$ R'R"C=$O_{(s)}$ + $HO_{2\,(g)}$ compares favorably with gas phase data but due to the consideration for $O_2$ solubility within the film, this channel appears to be relatively less important for surfaces. We have tested the sensitivity of the model in describing the mass change behavior for alkane films exposed to OH radicals at various $O_2$ concentrations employed in our QCM–CIMS experiments, and reproduced the $O_2$ independence. Additionally, the model is able to reproduce a linear dependence on OH exposure, as well as effects on relative mass change related to physical evaporation and formation of nitrates on the surface in the presence of $NO_x$.

## 4.4 Carbon chain length dependence

While we investigated a wide range of experimental conditions relevant to the troposphere with a $C_{36}H_{74}$ model surface, field measurements (Azimi et al., 2005) and analysis of diesel exhaust (Sakurai et al., 2003) show that particulate alkanes typically range from $C_{24}$ to $C_{32}$ in length. To expore a possible dependence on carbon chain length, we compared the reactivity of a series of *n*-alkane films ($C_{24}H_{50}$, $C_{30}H_{62}$, and $C_{36}H_{74}$). Paraffin wax samples (a mixture of *n*-alkanes) which had been pumped at low pressure (1 Torr) for 24 – 48 hr exhibited comparable reactivity to $C_{36}H_{74}$ films within experimental error.

Although $C_{24}H_{50}$, $C_{30}H_{62}$, and $C_{36}H_{74}$ are very similar in appearance as white, finely-divided crystalline flakes, clear differences were observed in their reactivity to OH radicals as measured via net mass change. Based upon our data regarding volatilization of shorter-chain, unoxidized compounds (i.e., $C_{18}H_{38}$), a negative correlation between alkane chain length and the rate of mass loss upon reaction had been anticipated. In fact, the opposite was observed. Under equivalent conditions, we found that OH-initiated oxidation resulted in less net volatilization for shorter chain alkane molecules, independent of OH production source, non-linear with respect to carbon chain length, and consistent both in the presence

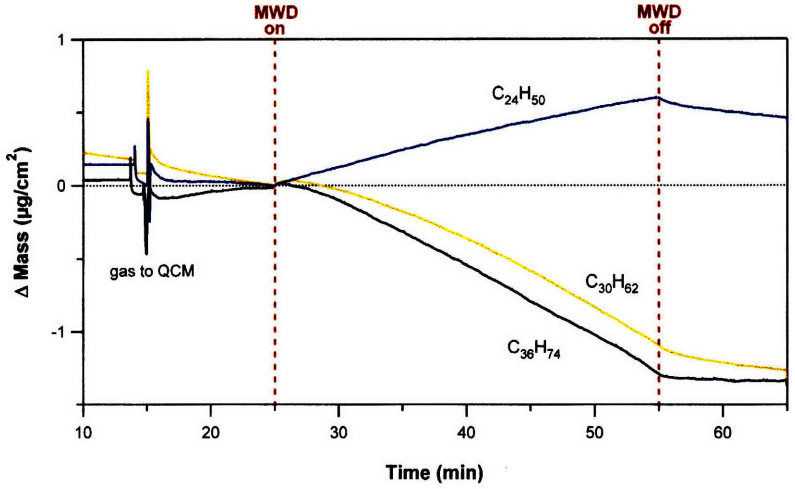


Figure 4-19: Time-dependent change in mass for $C_{24}H_{50}$, $C_{30}H_{62}$, and $C_{36}H_{74}$ upon exposure to OH = 54 kcps in $[O_2] = 2{\cdot}10^{18}$ molec/cm$^3$.

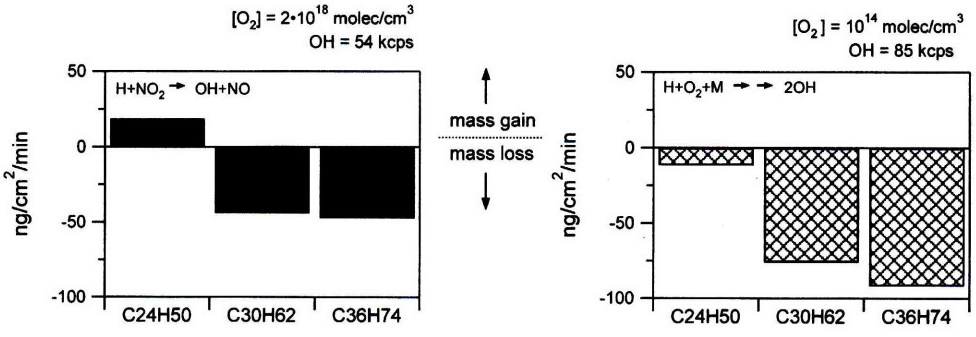


Figure 4-20: Reactivity comparison of $n$-alkane films; shorter-chain molecules exhibit lower net mass loss upon OH-initiated oxidation for all $O_2$ concentrations, and in presence as well as absence of $NO_x$.

and absence of $NO_x$. Figure 4-19 compares the mass change rates ($\Delta$mass/time) for $C_{24}H_{50}$, $C_{30}H_{62}$, and $C_{36}H_{74}$ exposed to OH with $[O_2] = 2{\cdot}10^{18}$ molec/cm$^3$. Experiments were performed consecutively under the same flow and gas-phase reactant concentrations. Figure 4-20 showed the rates of mass change for comparison of different OH production sources; the left panel shows data collected using the $H + NO_2 \rightarrow OH + NO$ reaction as OH radical source with $[O_2] = 2{\cdot}10^{18}$ molec/cm$^3$, while the right-hand panel shows data using the $H + O_2 + M \rightarrow 2OH + M$ reaction sequence. In both cases, the $C_{30}H_{62}$ film exhibited a slower mass loss rate (10 – 20%) compared to $C_{36}H_{74}$. The difference was greater for $C_{24}H_{50}$ films which exhibited only a slight mass loss ($NO_x$–free conditions) or net mass gain (in presence of $NO_x$). Additional studies employing the $H + NO_2 \rightarrow OH + NO$ source showed the same trend for $[O_2] = 3{\cdot}10^{14}$ molec/cm$^3$ and $[O_2] = 3{\cdot}10^{16}$ molec/cm$^3$.

We attribute these results to differences in sample morphology and/or crystal structure; a detailed microphysical characterization of our films is suggested for future study in order to fully rationalize these observations. Because organic aerosols in the atmosphere are complex mixtures with unknown microphysical structures, our films were prepared without special consideration to crystallization. The films were assumed to be semi-crystalline with some degree of amorphous character. This is based on the fact that the unoxidized $C_{36}H_{74}$ samples used in our experiments measured a water contact angle of 97° – 98°, compared to measurements for idealized $C_{18}$ alkane monolayers of 112° (Ulman, 1991).

It is known that $C_{24}H_{50}$ has a triclinic structure whereas $C_{30}H_{62}$ and $C_{36}H_{74}$ are monoclinic (Craig et al., 1994). Given the lattice spacing relevant to each, we approximate that a crystalline $C_{24}H_{50}$ film contains 1/3 the free volume available in $C_{36}H_{74}$ or $C_{30}H_{62}$ films. Closer packing of $C_{24}H_{50}$ molecules implies greater probability for neighboring chains to react, but may also impose mobility restrictions in the necessary orientation for unimolecular RO$\cdot$ isomerization. Since mass gain and loss are in competition from the perspective of QCM detection, a net mass gain implies extensive oxidation through formation of C–O functional groups at the expense of volatilization. The trend observed in our experiments indicates efficient $O_2$ addition to the surface; a relatively higher mass gain observed in the presence of $NO_x$ would be consistent with formation of alkyl nitrates and/or peroxynitrates as previously discussed.

Following the possibility for differences related to steric factors and/or crystal structure, we attempted to investigate an odd-numbered alkane, nonacosane $C_{29}H_{60}$. The question of

possible reactivity differences is also relevant to the fact that an odd/even preference has been observed for atmospheric alkanes originating from biogenic vs. petrochemical sources (Azimi et al., 2005). However, it was found that the $C_{29}H_{60}$ solid did not melt evenly across the crystal face, but rather formed an irregular film with crystals aggregated together. Odd-numbered alkanes are reported to have an orthorhombic crystal structure, different from most even-numbered alkane molecules, which may help to rationalize these complications. As a result of inhomogeneous surface coverage, the QCM had difficultly locking onto the frequency of the mass-loaded crystal. The high uncertainty prohibited drawing conclusions for an even/odd dependence.

## 4.5 Organic functional group investigation

Alkane films were chosen as model surfaces for our studies of heterogeneous OH-initiated oxidation because they represent the simplest system from a mechanistic standpoint, and considering that a large majority of atmospheric organic aerosols are expected to contain at least partial C−H saturation. However, it has been shown in numerous field studies that the oxygen content of organic aerosols increases with their photochemical age through increased C−O functionality (McFiggans et al., 2005; Rudich et al., 2007; Salcedo et al., 2006).

To investigate possible differences in OH-reactivity leading to surface decomposition as related to the presence of functional groups, we compared the mass change detected in alkane films upon exposure to OH radicals to that for several carboxylic and dicarboxylic acid compounds. Triacontanoic acid ($C_{30}H_{60}O_2$), a monocarboxylic acid, was chosen for direct comparison with the saturated analogue, $C_{30}H_{62}$. Glutaric ($C_5$) and azelaic acid ($C_9$) are dicarboxylic acids where the latter is a minor product of oleic acid ozonolysis (Katrib et al., 2004). Glutaric, azelaic, and oleic acid have all been identified in urban aerosol with concentrations $\sim$ 30 ng/m$^3$ (Rogge et al., 1993).

According to the anticipated heterogeneous mechanism (Sec. 4.3.4), OH reactivity is determined by the availability of H atoms for abstraction, including the nature of the C−H bond. Organic molecules with appreciable C−H saturation are therefore expected to exhibit comparable reactivity. However, it is important to reiterate that the QCM measures a net mass change such that the magnitude of the mass loss/gain rate depends upon the chemical

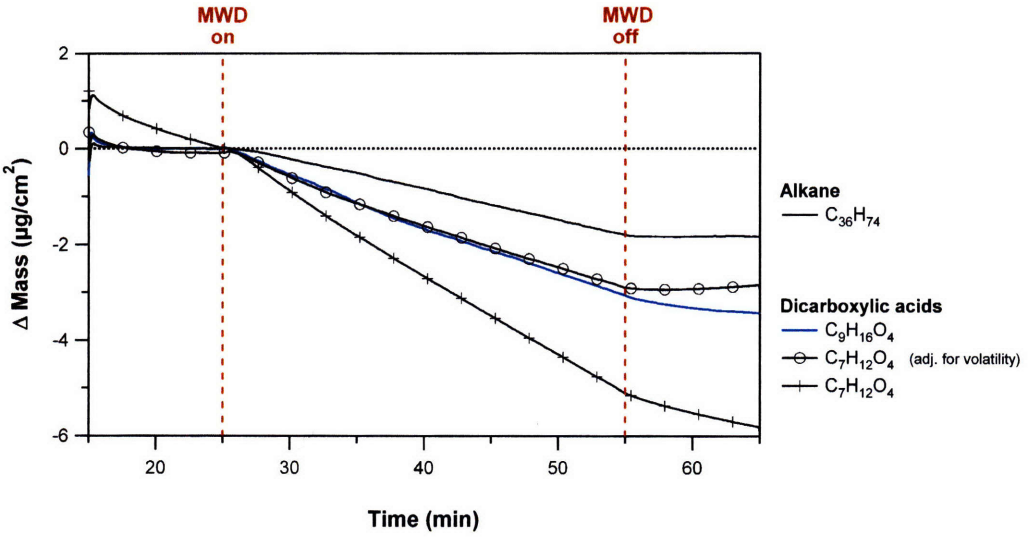


Figure 4-21: Mass loss comparison of alkane and dicarboxylic acid films. Experimental conditions were: $[O_2] = 3{\cdot}10^{16}$ molec/cm$^3$, OH = 77 kcps, H + $NO_2$ $\rightarrow$ OH + NO source at 100 Torr, 295K.

identity of the fragments leaving the surface. Additionally, the results obtained for different alkane chain lengths suggest that crystal structure may play an important role.

We found that $C_{30}H_{60}O_2$ films exhibited a comparable rate of volatilization, or slightly faster, than $C_{30}H_{62}$ within experimental error. A slightly higher quantity of mass released per unit time could reflect the loss of COOH end-groups vs. $CH_2O$, assuming the latter is a primary scission product of alkane oxidation.

Mass loss by azelaic acid films was observed to proceed 1.5 to 2 times faster than $C_{36}H_{74}$ under the same experimental conditions, as shown in Figure 4-21. It is likely that the shorter chain length of azelaic acid facilitates paritioning into the gas-phase upon loss of the $-$COOH end-groups through decomposition pathways. Glutaric acid was somewhat volatile under flow conditions at 100 Torr; a correction for the added volatilitiy shows agreement with reactivity of azelaic acid under the same experimental conditions. Comparing the measured volatility rate before reaction ($\sim$ 100 ng/cm$^2$/min) to that immediately following OH-exposure ($\sim$ 65 ng/cm$^2$/min), offers supporting evidence for a decrease in vapor pressure by formation of carbon-oxygen surface groups. This can be rationalized through the anticipated heterogeneous mechanism where different RO$\cdot$ branching ratios for decomposition (C$-$C scission) and reaction with $O_2$ to form non-radical products on the surface

(ketones, aldehydes).

## 4.6 Soot reactivity

In previous studies, we exposed soot films to $OH/O_3/H_2O/UV$ to simulate atmospheric chemical processing to investigate increased hygroscopicity of soot surfaces as a result of oxidation (Zuberi et al., 2005). It was found that the exposure enabled surface to take up water efficiently at relative humidity (RH) levels relevant to the troposphere ($102 \pm 2\%$). In these experiments, OH radicals were generated by photolysis of $O_3$ in the presence of water vapor (Reactions 4.1 and 4.2) where the OH concentration was calculated from known initial conditions. The QCM–CIMS system provides the possibility to study the reactivity of soot by exposure to a directly measured OH concentration.

Several comments should be made regarding the preparation of soot samples for QCM–CIMS studies performed at reduced pressure under constant flow. Soot has a loosely-held, powdery consistency which makes it difficult to adhere to the crystal surface. Freshly-emitted soot may also contain reactive semi-volatile organic compounds formed in the flame that condense on the surface, which could potentially be lost under reduced pressures. Despite these complications, it is extremely relevant and important to investigate chemical processing of soot considering its importance to urban environments and unique physico-chemical properties (see Ch. 3).

As done in our previous studies, soot samples were prepared by holding a QCM crystal in the exhaust above a methane flame for several minutes until the surface was brownish-black in appearance. The mass collected as measured by the QCM relative to the plain, uncoated crystal was $\leq 10\ \mu g/cm^2$; condensed water from the flame may have contributed to the total mass measured. Upon loading the crystal into the QCM holder and reducing the pressure from 756 Torr to 100 Torr under flow conditions, an immediate loss of 0.5 $\mu g/cm^2$ was detected and most likely consisted of volatile organics and/or condensed water. The $H + O_2 + M$ reaction sequence was used in OH production in consideration for the known reactivity of soot with $NO_x$ (Kirchner et al., 2000; Chughtai et al., 1994) and $O_3$ (Smith and Chughtai, 1996; Kamm et al., 1999; Disselkamp et al., 2000).

Figure 4-22 shows our data for the QCM-measured mass change by a methane soot film exposed to [OH] = 25 kcps. Also shown are data for a plain, uncoated crystal exposed to

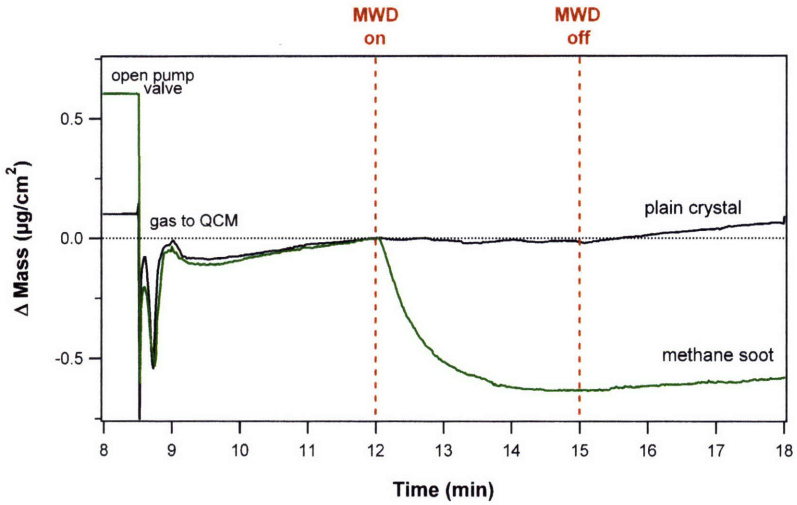


Figure 4-22: Mass loss by a methane soot film exposed to [OH] = 25 kcps generated via H + $O_2$ + M at 100 Torr.

OH under the same conditions. Ignition of the MWD to generate OH caused an immediate loss of 0.6 $\mu g/cm^2$ by the soot, quickly followed by a plateau in $\Delta$mass/time within 2 – 3 minutes exposure. Allowing for greater uncertainty inherent in QCM measurement of soot, we confirm a particularly high reactivity of soot with OH, in accordance with high OH uptake on soot ($\gamma_{OH} \sim 1$) reported by our laboratory (Bertram et al., 2001).

Similar to organic aerosol, few published reports are available to describe soot reactivity with OH. In a flow reactor study involving diesel particulate matter containing known amounts of various PAH compounds, Esteve et al. (2006) observed that OH reactivity with the surface was four orders of magnitude greater than reactions with $NO_2$. They also reported that compared to gas phase PAH molecules, heterogeneous oxidation of particle-bound PAHs appeared to occur more slowly, presumably due to the inaccessibility of OH reaching the PAH compounds owing from a high surface area of soot.

Considering the partial aromatic character of soot (Fig. 3-2 in Ch. 3), we performed QCM–CIMS experiments to explore the OH-reactivity of particulate PAH compounds where pyrene ($C_{16}H_{10}$, 4-ring PAH) was chosen as a model compound for study. Similar to the problems encountered with $C_{29}H_{60}$, it was difficult to establish a lock on the QCM frequency given the inhomogeneity in surface coverage. Irregular morphology of pyrene surfaces is evident by electron microscopy as highlighted by Bertram et al. (2001). Allowing for a higher error in QCM measurement, we found supporting evidence that $O_2$ addition to the

surface occurs upon surface activation by reaction with OH, as follows from the gas-phase mechanism for OH oxidation of aromatic compounds (Finlayson-Pitts and Pitts, 2000). Additional study would be required to develop and investigate the heterogeneous mechanism involving oxidation of aromatic compounds.

## 4.7 Discussion and conclusions

The primary goal of our studies, employing the QCM–CIMS technique to probe the mechanism of OH-initiated oxidation, was to evaluate the decomposition pathway for organic aerosol exposed to OH under tropospheric conditions. Specifically, it was unknown to what extent $O_2$ would be able to terminate the oxidation sequence via production of non-radical products which remain bound to the surface. Oxygen is expected to participate in two key reactions: addition to R· to form $RO_2$· radicals, and H-abstraction of RO· to form carbonyl compounds and $HO_2$ radicals. The rate constants obtained by numeric kinetic modeling compare well with those well-established for gas-phase reactions upon accounting for $O_2$ solubility in the film.

We confirmed a strong, linear dependence of surface decomposition on the OH concentration during exposure. The rate-limiting step in the oxidation mechanism under atmospheric conditions is likely to be the initial OH attack leading to formation of peroxy radicals on the surface, followed by fast formation and reaction of alkoxy radicals. As described in our kinetics modeling studies, two neighboring peroxy radicals can react to form alkoxy radicals, $RO^{\cdot}_{2(s)} + RO^{\cdot}_{2(s)} \rightarrow RO^{\cdot}_{(s)} + RO^{\cdot}_{(s)} + O_{2\,(g)}$, where subsequent reactions of the alkoxy radicals dictate the final oxidation products. However, an alternative possibility exists in which the peroxy radical reacts with a neighboring alkyl radical created by an additional OH attack, $RO^{\cdot}_{2(s)} + R^{\cdot}_{(s)} \rightarrow RO^{\cdot}_{(s)} + RO^{\cdot}_{(s)}$. This pathway is likely more significant in low $O_2$ concentrations, but due to the high reactivity of R· may also be important under atmospheric conditions. Decomposition of the alkoxy radical remains a relevant reaction pathway under tropospheric $O_2$ concentrations; furthermore it appears likely that RO· decomposition and isomerization are competitive reaction channels whose relative dominance depends on both the chemical and physical nature of the organic compound. Our results suggest that the reactivity of an organic film (as measured in a net mass change) is sensitive to the structural arrangement of molecules making up the surface. This is likely important

for both reactions between neighboring molecules, as well as unimolecular reactions which may require a minimum free volume to occur. The fact that oxygen-substituted compounds exhibited comparable reactivity as alkanes agrees with the availability of C–H bonds for OH attack, and extends the relevance of heterogeneous oxidation for a large body of organic compounds present in the atmosphere.

Both NO and $NO_2$ appear to play complex, yet exceptionally important roles in the heterogeneous oxidation mechanism for organics. Our results for relatively slower volatilization in presence of $NO_x$ are indicative of formation of nitrate compounds, however additional studies would be useful for their direct detection and identification. The potential for organic aerosols to act as temporary reservoirs for $NO_x$ via $RO^{\cdot}$ and/or $RO_2^{\cdot}$ reactions is important to understand both aerosol reactivy and atmospheric lifetime as well as regional transport of $NO_x$.

# Chapter 5

# Hydrophilic properties

## 5.1 Introduction

The fate of carbonaceous aerosols and their environmental effects are directly related to their interaction with water. Wet deposition is the dominant removal pathway for accumulation mode aerosols (0.1 $\mu$m $\leq$ $d_p$ $\leq$ 2.5 $\mu$m) via precipitation scavenging, snow deposition, impaction with fog and cloud droplets, or serving as nuclei in cloud formation followed by rainout. The efficiency of these processes depends upon both particle size and chemical composition.

The content of water vapor in the atmosphere is often expressed in terms of percent relative humidity (RH), defined as the ratio of the partial pressure of water ($P_{H2O}$) to its saturation vapor pressure ($P^{o}_{H2O}$) at a given temperature:

$$RH = \frac{P_{H2O}}{P^{o}_{H2O}} \cdot 100\% \tag{5.1}$$

RH levels vary widely in the troposphere, from less than 10% up to several percent supersaturation in clouds and fogs (Seinfeld and Pandis, 1998). Hygroscopic compounds, including most inorganic salts, absorb water and can exhibit a spontaneous, uncontrained uptake at the deliquescence RH (DRH) to form a saturated liquid droplet. The same droplet loses water with decreasing humidity in a hysteresis such that the efflorescence (crystallization) occurs at a lower RH (Finlayson-Pitts and Pitts, 2000). Several hygroscopic species such as $H_2SO_4$ take up water continuously.

Particles with greater water-soluble content undergo more efficient washout/rainout

(Hallberg et al., 1994; Sellegri et al., 2003; Massling et al., 2003). While inorganic sulfates and nitrates readily take up water, carbonaceous aerosols are more hydrophobic due to the non-polarity of their C−H bonds. Chemical and physical changes associated with atmospheric processing can greatly enhance their ability to take up water, however. For example, Kotzick and Niessner (1999) showed increased hygroscopicity of carbon aerosols upon $O_3$ oxidation, or by coagulation with NaCl and $H_2SO_4$ aerosols. Similarly, Demou et al. (2003) reported a correlation between the oxidation state (C−O functional groups) of an organic film and its measured water uptake (i.e. dicarboxylic acid > diol > alcohol).

Because atmospheric processing involves a complex set of chemical reactions and physical mechanisms which continuously modify the physico-chemical properties of aerosols, and considering the variability in environmental conditions and reactant concentrations, carbonaceous aerosol lifetimes are difficult to determine. This is currently one of the greatest sources of uncertainty in global climate assessments (Forster et al., 2007; Kanakidou et al., 2005). Modelers approach this problem by specifying hydrophobic and hydrophilic categories of black carbon (BC) soot and organic aerosols, where a specific time constant is assumed for a hydrophobic–to–hydrophilic transformation. The lifetime of the hydrophilic fraction is then determined by wet deposition removal according to its solubility (Henry's law constant) or based upon known scavenging characteristics of other compounds. For example, Tie et al. (2005), following the method of Cooke and Wilson (1996), assumed that initially hydrophobic BC and organic aerosols become hydrophilic in 1 day, and thereafter are scavenged at the same rate as sulfate aerosols. A sensitivity analysis by Cooke and Wilson (1996) showed a range of 6 to 10 days for the BC lifetime given different assumptions for the hydrophoblic–hydrophilic time constant.

Laboratory measurements reduce modeling uncertainties by providing information on the connections between atmospheric processing, aerosol composition, and their subsequent water uptake characteristics. Building upon our previous field analyses and laboratory studies, we explored the hygroscopicity of internally-mixed aerosols collected from the Mexico City Metropolitan Area (MCMA), and oxidized carbonaceous films as proxy surfaces for aerosols in atmospherically-relevant RH.

## 5.2 Hydration study of internally-mixed urban aerosols

As discussed in Chapter 3, aerosol processing in Mexico City occurs rapidly and leads to internal mixing such that individual particles contain components originating from different emissions sources. Special attention was given to the fact that soot particles were heavily mixed with ammonium sulfate inclusions, or were otherwise entirely embedded in sulfate. This mixing is expected to determine the lifetime of the particle, specifically related to the more hygroscopic component. The 2006 MILAGRO Campaign enabled us to collect additional samples to investigate the water uptake characteristics of these internally-mixed urban aerosols. These studies were done in collaboration with Dr. Yong Liu and Dr. Alex Laskin at Pacific Northwest National Laboratory.

### 5.2.1 FTIR – flow cell technique

A FTIR – flow cell detection system, described below, was used to investigate the water uptake characteristics of mixed urban aerosols. Fourier Transform Infrared (FTIR) spectroscopy provides specific information on the molecular structure of a compound through analysis of its IR absorption spectrum. Absorption of IR radiation (200 – 4000 $cm^{-1}$) excites a molecule to a higher vibrational state where transitions allowed by a change in dipole moment are characteristic of specific bonds within the molecule. The distinct advantages of IR spectroscopy include suitability for different media (solids, liquids, gases), high sensitivity to a wide range of functional groups, and the rich dataset of structural information that may be obtained. The latter can also present a disadvantage in the case of complex mixtures, however, where it may be difficult to extract information on a specific component.

For this study, particles were collected during the 2006 MILAGRO campaign in Mexico City from a site ("T0") located near downtown MCMA (see Sec. 2.5). Particles were collected in the same manner described previously onto TEM grid substrates by means of a TRAC collector (see Sec. 3.2). Before exposing the particles to a wet environment, morphology and mixing characteristics were analyzed by SEM/EDX, and the chemical composition of a collection of particles was determined by CCSEM/EDX. The reduced pressure during these analyses likely caused a loss of volatile compounds, including nitrates and organics. The composition statistics obtained by CCSEM/EDX were similar to results for ambient particles during the MCMA–2003 campaign (Johnson et al., 2005) with the

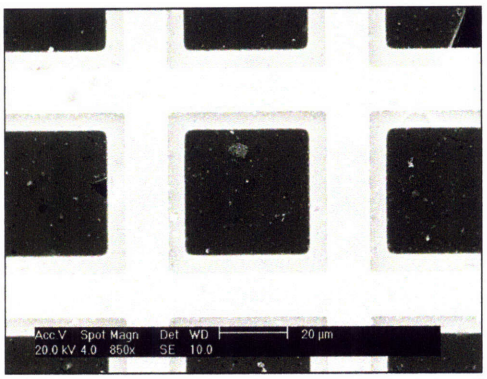


Figure 5-1: TEM grid area for the FTIR hydration study.

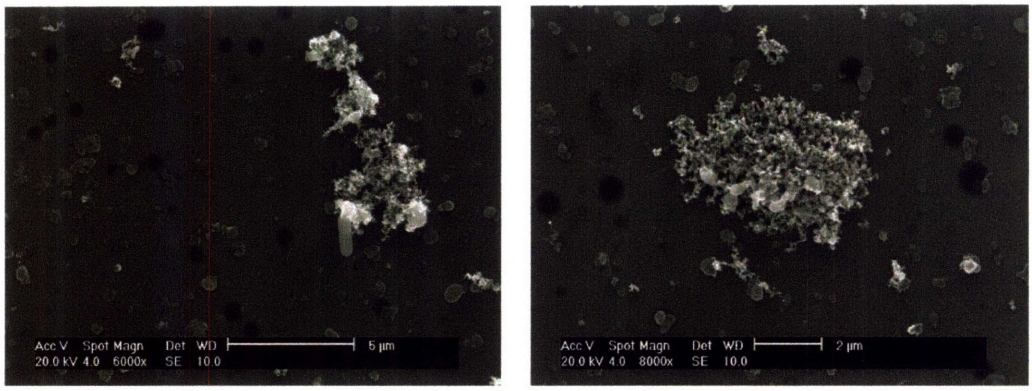


Figure 5-2: SEM images of aerosol samples collected during the 2006 MILAGRO campaign for the FTIR hydration study.

following elemental ratios: S/C = 0.035, O/C = 0.086, N/C = 0.095. The majority of the mixed particles contained sulfur and were sensitive to the intensity of the electron beam, which would be consistent with the presence of $(NH_4)_2SO_4$.

Following composition analysis by CCSEM/EDX, the aerosol sample grid and a blank reference grid were housed in a small flow cell and exposed to varying RH by adjusting the flow rates of dry $N_2$ and a $N_2/H_2O$ mixture controlled by a dew point hygrometer. The RH was increased or decreased in increments of 2 – 10% and the system allowed to equilibrate for at least 5 mins before recording a spectrum. A Bruker FTIR instrument equipped with OPUS software was used for data collection, and to correct for gas-phase $CO_2$ and $H_2O$ absorptions. Corrections for the absorption characteristics of the substrate were made by reference to the blank grid. This technique has shown agreement for the deliquescence of pure $NaNO_3$ particles, RH = 71 – 72% (A. Laskin, personal communication). Studies

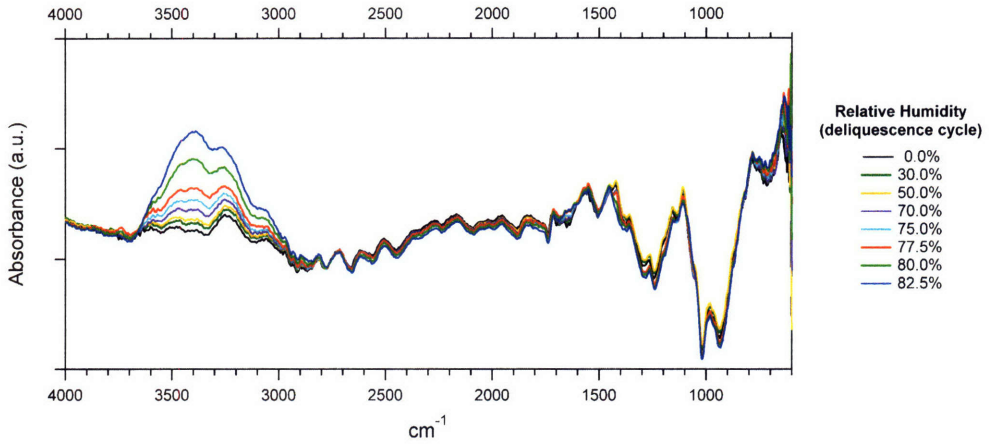


Figure 5-3: Deliquescence cycle of an aerosol sample collected near downtown Mexico City during the 2006 MILAGRO campaign as measured by FTIR. Increasing intensity of the broad O–H stretch at 3300 – 3500 $cm^{-1}$ indicates greater water uptake by the particles.

Table 5.1: IR absorption bands for select inorganic and organic species (Smith, 1999).

| Species | IR absorption band |
|---|---|
| $H_2O$ | 3300 – 3500 $cm^{-1}$ |
| $NH_4^+$ | 3270 $cm^{-1}$ |
| $SO_4^{-2}$ | 1100 $cm^{-1}$ |
| " | 600 – 650 $cm^{-1}$ (bend) |
| $NO_3^-$ | 1350 – 1450 $cm^{-1}$ |
| saturated $CH_3$, $CH_2$ | 2850 – 3000 $cm^{-1}$ (C–H) |
| unsaturated C=C, C≡C | > 3000 $cm^{-1}$ (C–H) |
| " | ~ 1660 $cm^{-1}$ (C=C) |
| aromatic | 1400 – 1620 $cm^{-1}$ (C=C) |
| " | < 1000 $cm^{-1}$ (C–H bend) |

of both the deliquescence (increasing RH) and efflorescence (decreasing RH) behavior of MCMA aerosol samples were performed at atmospheric pressure and 296 K.

The area of the sample grid used for FTIR analysis was approximately 3 x 3 windows, selected in order to maximize the FTIR signal intensity while minimizing the analyzed area. Particles are visible on the thin film windows in Figure 5-1 (dark area), which are divided by Cu grid supports (bright area). Magnified SEM images of particles within the analyzed area appear in Figure 5-2.

IR spectra recorded during the deliquescence cycle (RH = 0% to 82.5%) appear in Figure 5-3. Water uptake with increasing RH is evident by increasing intensity of the broad O–H stretch (3300 – 3500 $cm^{-1}$). The uptake is more clearly shown by a plot of the

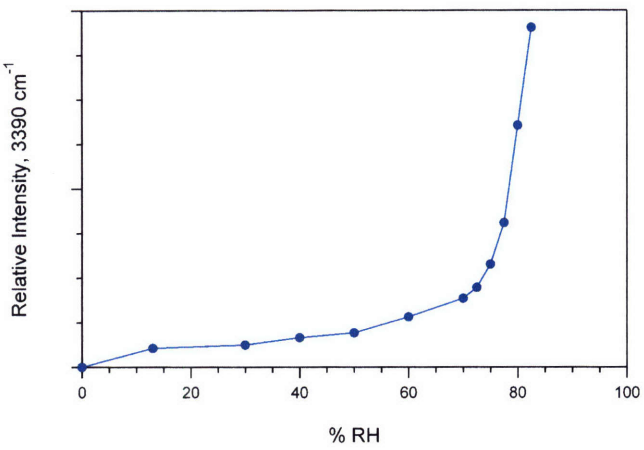


Figure 5-4: Relative humidity vs. water uptake by MCMA aerosol as measured by the relative FTIR absorption intensity at 3390 $cm^{-1}$.

intensity measured at the maximum absorption peak (3390 $cm^{-1}$) vs. RH, in Figure 5-4. A distinct increase in the absorption intensity as RH > 75% is comparable to the DRH of pure $(NH_4)_2SO_4$ particles (RH = 80.2%) (Marcolli et al., 2004). Literature values for the DRH of several other atmospheric inorganic and organic compounds are listed in Table 5.2 for reference.

Studies have shown that the deliquescence of mixed inorganic/organic particles may occur at a lower RH than either individual component (Choi and Chan, 2002; Salcedo, 2006; Marcolli et al., 2004). For example, Choi and Chan (2002) reported a range of DRH = 68.7% – 76.6% for a 1:1 mixture of glutaric acid and $(NH_4)_2SO_4$, where the DRH for pure glutaric acid has been measured at 88.2% (Marcolli et al., 2004). These results imply that a complex mixture of organic and inorganic compounds, as is the case for MCMA aerosols, can take up water well below RH = 80%. However, as discussed by Choi and Chan (2002), the ability for organics to either positively or negatively influence the water uptake of inorganics remains the subject of considerable debate and may be specific to the given compounds. Figure 5-4 shows an increase in the absorption peak above baseline for RH = 30% with incremental gains up to $\sim$ 75%, but the largest increase was observed as RH approaches 80%. As discussed in Chapter 2, ammonium sulfate comprises a major fraction of MCMA $PM_{2.5}$ (35% of the non-volatile mass, nearly 15% of total $PM_{2.5}$ (Salcedo et al., 2006)) and organic compounds make up more than 50%. CCSEM/EDX analysis under vacuum prior to the hydration study is expected to have caused loss of organics and

Table 5.2: Deliquescence RH for several atmospheric inorganic compounds.

| Compound | DRH (25°C) | Reference |
|---|---|---|
| $(NH_4)_2SO_4$ | 80.2% | Marcolli et al. (2004) |
| $NH_4HSO_4$ | 40.2% | Salcedo (2006) |
| $NH_4NO_3$ | 62.1% | Marcolli et al. (2004) |
| NaCl | 75.3% | Marcolli et al. (2004) |
| malonic acid | 72.4% | Marcolli et al. (2004) |
| oxalic acid | 97.8% | Marcolli et al. (2004) |
| glutaric acid | 88.2% | Marcolli et al. (2004) |
| adipic acid | 99.9% | Marcolli et al. (2004) |

nitrates, but the information provided by PESA analysis for organic H (Sec. 2.6.3) shows that non-volatile organics should have been retained. Because we would expect organics to affect the characteristic RH values for measureable water uptake by the mixed particles, additional studies in which samples are maintained at atmospheric pressure would be useful.

To our knowledge, this is the first use of FTIR to analyze hygroscopic properties of urban aerosols. The inherent complexity of MCMA $PM_{2.5}$ prohibits identification of all spectral features; Table 5.1 lists the absorption bands of several relevant functional groups for reference. Absorptions at 1110 $cm^{-1}$ ($SO_4{}^{-2}$ stretch) and 3270 $cm^{-1}$ ($NH_4{}^{+}$ stretch) offer support for the presence of $(NH_4)_2SO_4$. Schuttlefield et al. (2007) observed similar spectral features for laboratory-prepared $(NH_4)_2SO_4$ particles analyzed by attenuated total reflection FTIR (ATR-FTIR) coupled to a flow cell. They reported DRH = 81 $\pm$ 2% for $(NH_4)_2SO_4$ based upon the integrated intensity of the O–H stretching region.

The FTIR – flow cell technique used in our studies is not suitable for individual particles due to signal-to-noise limitations; however, our results suggest that water uptake by the collection of particles is dictated by sulfate, among the most abundant and hygroscopic components in MCMA $PM_{2.5}$. In a previous laboratory study, we found that freshly-emitted soot did not take up water, even at 15% supersaturation (Zuberi et al., 2005). Considering the large body of evidence showing extensive soot/sulfate mixing in MCMA aerosols, our results offer support for physical processing of soot leading to enhanced water uptake.

## 5.3 Heterogeneous OH-initiated oxidation in the presence of water vapor

In the previous chapter (Ch. 4), the OH-initiated oxidation of carbonaceous thin films was investigated in detail to obtain mechanistic information under conditions relevant to the troposphere. While we found that surface decomposition was insensitive to $O_2$ concentrations within the range studied ($\sim 10^{12} - 2{\cdot}10^{18}$ molec/cm$^3$), water vapor is also an important tropospheric constituent with the potential to affect organic aerosol oxidation. Possible effects of water include adsorption to an increasingly oxidized (polar) surface, and/or direct reaction with surface active sites. Studies were therefore performed to evaluate organic aerosol oxidation in a humid environment.

The QCM–CIMS system was used in the same manner described previously (see Sec. 4.2), however the $N_2/O_2$ carrier gas flow was passed through a water bubbler prior to entering the flow tube. A maximum of 3.5 Torr of $H_2O$ could be introduced into the flow tube, resulting in RH $\leq$ 17% ($P_{H_2O}$ = 21.1 Torr at 296 K (Lide, 2007)) for a concentration [$H_2O$] $\leq 1.1{\cdot}10^{17}$ molec/cm$^3$.

### 5.3.1 CIMS detection under relative humidity

Ion–molecule reactions between water and $SF_6^-$ have been discussed in the literature (Arnold and Viggiano, 2001; Viggiano et al., 2005) and involve formation of water clusters:

$$SF_6^- + H_2O \leftrightarrow SF_6^-(H_2O) \tag{5.2}$$

$$SF_6^-(H_2O) + H_2O \rightarrow SF_4O^- + 2HF + H_2O \tag{5.3}$$

where the reaction proceeds by an initial equilibrium with $SF_6^-$ ions and is second-order with respect to $H_2O$, $K_{5.2}$ = [$SF_6^-H_2O$]/[$SF_6^-$][$H_2O$] = $5.7{\cdot}10^{-17}$ cm$^3$/molec; $k_{5.3}$ = $2.6{\cdot}10^{-14}$ cm$^3$/molec/s at 100 Torr (Arnold and Viggiano, 2001). Subsequent clustering reactions lead to production of $(HF)F^-$ (m/z 39), and $(HF)_2F^-$ (m/z 59) ions:

$$F^- + HF \rightarrow (HF)F^- \tag{5.4}$$

$$(HF)F^- + HF \rightarrow (HF)_2F^- \tag{5.5}$$

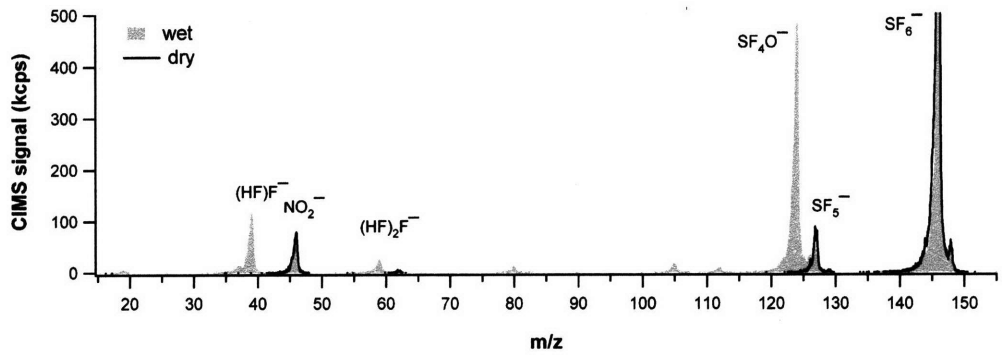


Figure 5-5: CIMS spectrum with $SF_6^-$ as parent ion in the presence of relative humidity (RH).

Figure 5-5 shows the CIMS spectrum for $NO_2$ with RH = 15%, $P_{FT}$ = 100 Torr at 296 K. The relative intensity of the peaks resulting from Reactions 5.2 to 5.5 is in agreement with the product distribution reported by Arnold and Viggiano (2001). From the initial $SF_6^-$ signal under dry conditions (100%), the following distribution was observed: $SF_6^-$ (48%), $SF_4O^-$ (42%), $(HF)F^-$ (7%), and $(HF)_2F^-$ (2%). Under wet conditions with RH = 15% the measured sensitivity for $NO_2$ and OH were reduced by 35–40%.

Studies were performed with $H + NO_2 \rightarrow OH + NO$ used as the source of OH radicals. To maintain conditions relevant to the troposphere, experiments were done in $[O_2] = 2{\cdot}10^{18}$ molec/cm$^3$ such that $[O_2]/[H_2O] \geq 10$. Upon passing the carrier gas through the water bubbler, flows were allowed to equilibrate for 1 hour during which time the $SF_6^-$ ion intensity decreased to approximately half the original value with simultaneous appearance of $SF_4O^-$, $(HF)_2F^-$, and $(HF)F^-$ ions.

Figure 5-6 compares the QCM-measured mass change by $C_{36}H_{74}$ films exposed to OH under dry and wet conditions. In both cases, a continuous net mass loss was detected upon exposure to OH, confirming that organic aerosol decomposition occurs in $O_2$ and $H_2O$ concentrations relevant to the troposphere. Water uptake by unoxidized films was not detected by the QCM. The OH concentrations normalized to the $SF_6^-$ signal were 60.2 kcps (dry) and 58.9 kcps (wet). The presence of water vapor at these levels changes the OH diffusion constant by less than 3%, therefore the OH concentrations to reach the organic surface are assumed equivalent for both cases within experimental error. Our results show a slower rate of mass loss by alkane films in RH, which could indicate $H_2O$ adsorption on the oxidized (polar) surface.

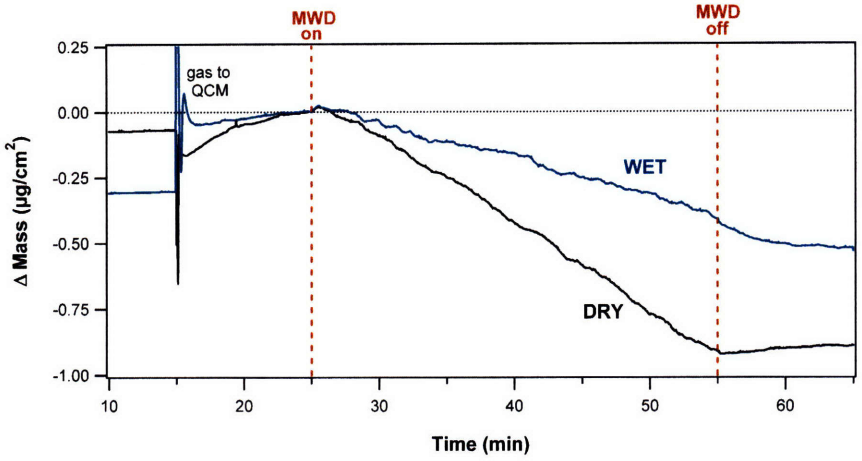


Figure 5-6: QCM-measured mass change by $C_{36}H_{74}$ films upon OH exposure under dry and wet (RH = 15%) conditions. The loss rates were $-34.2$ ng/cm$^2$/min with OH = 60.2 kcps (dry), $-14.5$ ng/cm$^2$/min with OH = 58.8 kcps (wet). The OH production source was H + $NO_2 \rightarrow$ OH + NO with $[NO_2] = 4.8{\cdot}10^{11}$ molec/cm$^3$.

To explore this possibility, several studies were done with azelaic acid ($C_9$ dicarboxylic acid). As for the alkane films, the unoxidized surface did not exhibit measurable water uptake. Upon exposure to OH radicals, a continuous mass loss was detected with a rate 2 to 3 times faster than $C_{36}H_{74}$ for an OH concentration about 30% higher (OH = 77.6 kcps; rate = -34.6 ng/cm$^2$/min). These differences in reactivity observed in a humid environment are similar to comparison of the two compounds under dry conditions (see Sec. 4.5). The arguments related to crystal structure and/or length of the parent molecule are also applicable under wet conditions. Since water uptake was not measured for the unoxidized surface at RH = 15%, it is more likely for water to interact with radical species on the activated surface rather than nonradical polar groups.

Additional studies would be required to more fully investigate the role of water vapor in the oxidation mechanism. We should anticipate a dependence on RH in order to explain the slower rate observed in comparison to dry conditions. However, considering the water molecule concentrations in our experiments, $[H_2O] = 1{\cdot}10^{17}$ molec/cm$^3$, effects related to water appear to be less significant than those related to $NO_x$ where $[NO] \leq 10^{14}$ molec/cm$^3$ and $[NO_2] \leq 5{\cdot}10^{12}$ molec/cm$^3$ led to a striking net mass gain measurement.

Since the RH levels in our studies were lower than the average for many locations (e.g., Mexico City RH $\sim$ 40%), the behavior of organic oxidation as RH approaches saturation

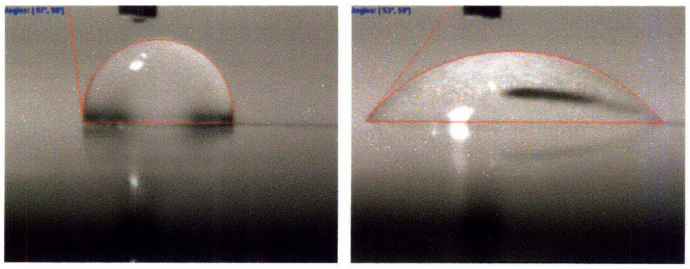

Figure 5-7: Water contact angle of a $C_{36}H_{74}$ thin film before (left), and after (right) oxidation by exposure to OH radicals.

may differ from these observations. For example, Demou et al. (2003) reported water uptake by malonic acid (a $C_3$ dicarboxylic acid) only for RH $\geq$ 60%, at which point the water adsorbed increased by a factor of 6.

Despite the fact that water adsorption was not measured within the detection limits of the QCM, the oxidized films were demonstrably hydrophilic. The water contact angle for a $C_{36}H_{74}$ thin film decreased from 97° to 51° after exposure to OH in $[O_2] = 2{\cdot}10^{18}$ molec/cm$^3$ at 100 Torr (dry conditions). This agrees with previous results from our laboratory for oxidized paraffin wax films (Bertram et al., 2001) as well as the more recent assessment by Petters et al. (2006) that chemical aging of organic aerosols ($d_p < 0.1$ $\mu$m) by OH-oxidation did not render organic aerosol surfaces hygroscopic enough for activation as cloud condensation nuclei (CCN).

## 5.4 Conclusions

Water plays an integral role in the evolution of carbonaceous aerosols in the troposphere. The atmospheric lifetimes of organic and soot particles are directly related to their hygroscopicity, and hence susceptibility to wet deposition removal. Since carbonaceous compounds are initially hydrophobic, the efficiency of their removal is determined to a great extent by changes to their physico-chemical properties through atmospheric processing.

We found that aerosols collected near downtown Mexico City exhibited gradual water uptake for RH = 30% to 75%, after which a more sudden adsorption was observed consistent with the deliquescence RH of $(NH_4)_2SO_4$ particles. Considering the extensive internal mixing between soot and sulfate particles observed in these particles, as well as information from previous analyses, we infer that physical processing of soot by coagulation/condensation of

water soluble inorganics, primarily sulfate, allow soot to become more hygroscopic which effectively dictates its atmospheric lifetime.

Chemical processing of carbonaceous aerosols can similarly enhance their ability to uptake water by formation of polar C−O groups on the surface. Studies into the potential involvement of water vapor in the heterogeneous mechanism for OH-initiated oxidation suggest that the decomposition rate is slowed in the presence of RH = 15%. Additional studies should be done with a wider range of RH levels to determine the RH dependence, and evaluate the decomposition pathway under conditions approaching high humidities.

# Chapter 6

# Conclusions

Incomplete understanding of the chemistry of atmospheric aerosols and processes driving their environmental effects is a leading source of uncertainty in global climate modeling. The chemical complexity of tropospheric aerosols, the balance between their sources and sinks, and the mechanisms underlying their physical and chemical transformations necessitates a comprehensive research approach. While field measurements are essential to frame the most important questions, careful laboratory study is essential for unraveling complex chemical mechanisms.

Carbonaceous aerosols are among the most important, yet least understood components of the troposphere, particularly in urban environments. They undergo extensive processing during their atmospheric lifetimes through interaction with other particles and gas-phase oxidants. Currently less than half the particulate organic mass in the atmosphere can be identified as to chemical structure and chemical composition, leaving important questions regarding their sources and removal mechanisms. In this thesis we have described detailed chemical analyses both from a field and laboratory perspective, aimed toward furthering our understanding of the mechanism underlying the transformation processes of carbonaceous aerosols.

## 6.1 Emissions sources and chemical composition of urban aerosols

The Mexico City Metropolitan Area (MCMA) is an exceedingly complex, yet immensely valuable laboratory for atmospheric chemical research due to its unique geographical and meteorological characteristics, in addition to socio-economic factors driving rapid population growth. Among the most important and problematic aspects of MCMA pollution is particulate matter $\leq 2.5$ $\mu$m in diameter ($PM_{2.5}$). Our analysis as part of the MCMA–2003 field campaign showed that over 50% of the non-volatile $PM_{2.5}$ is comprised by soot and organic aerosols. Other major emissions sources of particulates include sulfate (via secondary formation from $SO_2$), soil, and industrial sources.

A unique hydrogen marker for organics obtained via Proton Elastic Scattering Analysis (PESA) enabled the first-ever analysis of non-volatile vs. total organics in an urban environment by comparison with AMS real-time measurement of organic aerosol mass. Given the difference in pressure conditions employed during PESA and AMS detection, we found that non-volatile organics make up as much as 25% the total organic aerosol mass in Mexico City.

Soot aerosols are prevalent in Mexico City, primarily emitted from mobile sources and industrial activities, as well as from biomass burning. We showed that individual soot particles quickly become internally-mixed with inorganic sulfates, whose morphology suggests coagulation and/or condensation. An increase of water-soluble material by initially hydrophobic soot is expected to enhance its ability to uptake water and susceptibilty to wet deposition removal. Support for this argument was found by exposing these types of mixed particles to an increasingly humid environment in a FTIR – flow cell technique. The water uptake characteristics were indicative of $(NH_4)_2SO_4$ particles, observed as small inclusion on soot particles, or entirely enveloping a soot aggregate. Rapid mixing of soot particles is a key parameter to determine their atmospheric lifetimes and direct/indirect climate effects.

## 6.2 Laboratory studies of OH-initiated oxidation of organics and soot

Considering the importance of carbonaceous aerosols in the troposphere, particularly urban environments, laboratory experiments were designed to probe the reactions related to chemical processing via OH-initiated oxidation. A new experimental technique was designed, coupling together a flow tube with a Quartz Crystal Microbalance (QCM) for real-time monitoring of the surface reaction, and Chemical Ionization Mass Spectrometry (CIMS) for detection and quantification of the gas-phase reactants.

Previous studies showed that OH radicals efficiently oxidize carbonaceous surfaces leading to net decomposition. Anticipating similarities with the reaction mechanism for gas-phase oxidation, we explored the mass loss dependence by thin films exposed to OH on $O_2$ concentrations relevant to the troposphere. While the change in mass was strongly and linearly dependent on OH concentrations, the rate was independent of $O_2$ over a range of 6 orders of magnitude ($\sim 10^{12}$ – $2 \cdot 10^{18}$ molec/cm$^3$). This leads to the conclusion that decomposition remains an important channel in organic aerosol oxidation in the troposphere. Striking differences were observed in the presence of $NO_x$ and water vapor, suggesting however that these tropospheric constituents can inhibit mass loss via formation of nitrate compounds on the surface, and surface adsorption to polar reactive intermediates or oxidation products, respectively. Nitrate compounds have the potential to serve as temporary reservoirs for $NO_x$ and play a role in its transport from urban source regions to remote locations. Although the presence of water vapor appears to slow the loss rate, oxidized carbonaceous films were found to be hydrophilic, which could impact their wet deposition times and dictate their atmospheric lifetimes.

A key finding from our study was the importance of the film characteristics. It appears that the microphysical structure of the organic molecules, specifically the ability of neighboring molecules to interact chemically, or the space allowed for unimolecular reactions dictates the net effect of accumulated oxidation products in the film, or a net release of mass from the surface.

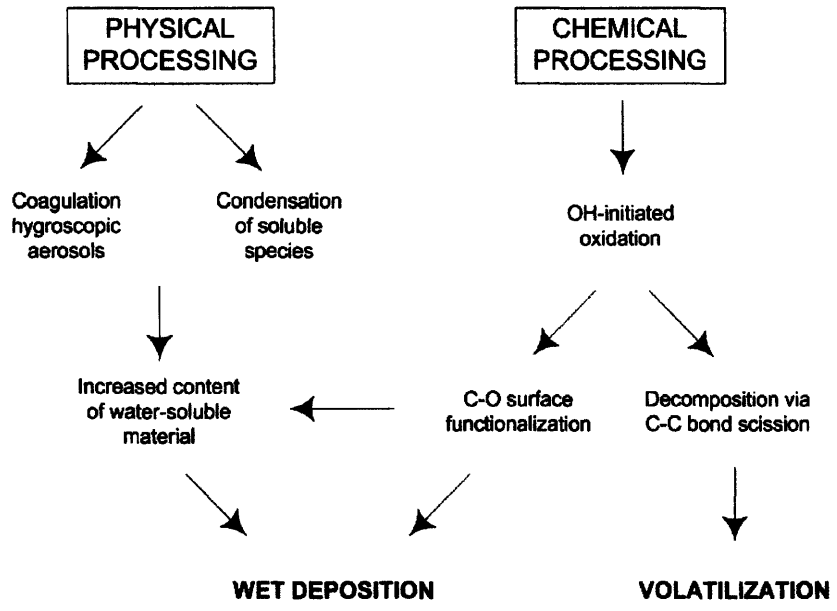


Figure 6-1: Physical and chemical aerosol processing and the fate of carbonaceous aerosols in the troposphere.

## 6.3 Atmospheric processing: physical and chemical mechanisms as related to aerosol lifetimes

Our results provide key insights into the possible removal mechanisms for carbonaceous compounds in the atmosphere. Combining the results from field and laboratory studies, the connections between physical and chemical processing of atmospheric aerosols may begin to be understood, as shown schematically in Figure 6-1. Physical mixing of hydrophobic carbonaceous compounds with more hygroscopic inorganics can lead to enhanced water uptake, as inferred from our studies of field samples collected in the MCMA. We showed that OH-initiated oxidation also enhances the hydrophilicity of the oxidized surface, likely by formation of oxygen-containing functional groups such as aldehydes and ketones. Oxidation of organic aerosol presents an additional removal mechansim via volatilization (C−C bond scission).

It remains to be experimentally investigated, or otherwise computationally determined

under which specific conditions physical vs. chemical processing becomes more important in determining the atmospheric lifetimes of soot and organic aerosols. These processes likely occur simultaneously and depend upon many parameters, several of which were explored here ($O_2$, $NO_x$, $H_2O$ concentrations).

# Chapter 7

# Recommendations for future research

This thesis describes studies of extremely complex atmospheric systems related to atmospheric aerosols. While we obtained a great deal of information and were able to reach important conclusions regarding the nature and reactivity of carbonaceous aerosols, several topics warrant additional investigation.

## 7.1 S(IV) to S(VI) oxidation on a soot surface

We found that soot particles collected from the Mexico City Metropolitan Area (MCMA) were mixed with $(NH_4)_2SO_4$, likely involving physical mechanisms of coagulation and condensation. Chemical reactions related to this system should also be studied. The ability for soot to act as a catalyst for heterogeneous $SO_2$ oxidation was proposed as early as 1974 (Novakov et al., 1974), prompting subsequent studies by others (Grgić et al., 1993; Chughtai et al., 1993; Smith et al., 1989). Although there is considerable variability in the experimental approaches taken, including the choice of model soot surfaces, most studies concluded that soot plays a minor role in S(IV) to S(VI) oxidation. However, Chughtai et al. (1993) studied the potential for transition metals found in trace amounts within soot particles to influence oxidation kinetics, and found the highest sulfate yield resulting from $SO_2$ reactions with a soot/$MnO_2$/$V_2O_5$ mixture. The high surface area afforded by soot and redox chemistry associated with the metals was invoked as an explanation for these results. A more recent study by Kim et al. (2005) showed that metal additives in fuel lower

the activation energy for soot oxidation.

Since Mn and V (among other metals) traced to industrial emissions and co-emitted with soot during the 2003 and 2006 field campaigns in Mexico City, and considering the importance of sulfate aerosols in the MCMA, soot as a potential heterogeneous reaction surface for $SO_2$ chemistry should be revisited. Important variables to explore include relative humidity (RH), OH, and $O_3$ which are known to enhance $SO_2$ oxidation rates in the aqueous phase (Finlayson-Pitts and Pitts, 2000).

In contrast to previous studies exploring this subject, careful attention should be given to the type of soot used. As observed in our studies, atmospheric soot is more chemically complex and heterogeneous than model compounds often used, including flame soot.

## 7.2 Influence of surface properties on oxidation kinetics of organic aerosol

Our QCM-CIMS studies of the OH-reactivity of *n*-alkanes as a function of carbon chain length suggest that the physical properties of the solid film matrix, specifically the proximity of neighboring hydrocarbon molecules on the surface in relation to both unimolecular and biomolecular reactions, significantly affect the oxidation kinetics observed. To further investigate these results, unoxidized surfaces should be well-characterized to provide a more complete understanding of the microphysical structure.

We found that the volatilization rate for *n*-alkane molecules was very sensitive within a narrow range of $C_{24}$ – $C_{36}$ (applicable to hydrocarbons detected in the atmosphere). Longer hydrocarbon chains (e.g., $C \geq 50$) would provide additional insight regarding carbon chain length. Branched alkanes could reveal information related to steric effects. A more controlled approach would involve preparation of organic films with well-characterized crystal structures and/or varying degrees of crystallinity.

## 7.3 Effects of relative humidity in the heterogeneous OH-initiated oxidation of organic aerosol

A major goal of this research was to probe the mechanism for OH-initiated oxidation of organic aerosol to assess the importance of volatilization under conditions applicable to the

troposphere. We sought specifically to understand the role of $O_2$; as noted, water vapor may also play an important role. While we have initial information that water can inhibit organic aerosol volatilization from OH-initiated oxidation, additional studies should be performed to determine a dependence on RH. Our studies were done at relatively low humidities (RH $\leq$ 15%), whereas oxidized organics are known to efficiently take up water at RH $\geq$ 60%. CIMS detection in a humid environment presents technical complictions, foremost a reduction in OH sensitivity. Applying the QCM-CIMS technique to explore higher relative humidities would require modifications similar to those employed in commercial atmospheric pressure ionization mass spectrometer (APIMS) systems. This would also enable studies to be done at atmospheric pressure, reducing the loss of semi-volatile organics we observed at the reduced flow tube pressures of 100 Torr.

## 7.4 Temperature dependence in heterogeneous oxidation of organic aerosol

In addition to $O_2$ and $H_2O$, temperature is an important parameter to include in order to survey a range of atmospheric conditions. Differences in the product distribution observed at the surface (P = 760 Torr, T = 288K, $[O_2] = 5{\cdot}10^{18}$ molec/cm$^3$) vs. the upper troposphere (P = 200 Torr, T = 223K, $[O_2] = 1.3{\cdot}10^{18}$ molec/cm$^3$) should be expected. A decrease in temperature could render certain energy activation barriers inaccessible; less energy available for unimolecular decomposition of RO$\cdot$ radicals could give rise to an accumulation of non-radical oxidation products in the aerosol phase and simultaneous release of $HO_2$ radicals for participation in $HO_x$ and $NO_x$ cycling reactions. A negative temperature dependence has been observed in the gas-phase formation of $RONO_2$ and $RO_2NO_2$ formation in the presence of NO (Atkinson et al., 1983); formation of nitrate and peroxynitrate compounds in the aerosol phase may become more important at colder temperatures, with a potential role in regional and long-range $NO_x$ transport.

These questions could be addressed through experimental study employing the QCM in a temperature-controlled environment. The information obtained would be useful to extract energetic parameters in order to test the robustness of the proposed oxidation mechanism and reaction rates. Studies are underway in our laboratory to measure the OH uptake coefficient $\gamma_{OH}$ on organic surfaces as a function of temperature.

# References


A.S. Ackerman, O.B. Toon, D.E. Stevers, A.J. Heymsfield, V. Ramamanthan, and E.J. Welton. Reduction of tropical cloudiness by soot. *Science*, 288:1042–1047, 2000.

M.S. Akhter, A.R. Chughtai, and D.M. Smith. The structure of hexane soot I: Spectroscopic studies. *Appl. Spectr.*, 39:143–153, 1985a.

M.S. Akhter, A.R. Chughtai, and D.M. Smith. The structure of hexane soot II: Extraction studies. *Appl. Spectr.*, 39:154–167, 1985b.

M.S. Akhter, A.R. Chughtai, and D.M. Smith. Spectroscopic studies of oxidized soots. *Appl. Spectr.*, 45:653–665, 1991.

F. Aldape, J. Flores M., J. Flores A., A. Retama-Hernández, and O. Rivera-Hernández. Elemental composition and source identification of $PM_{2.5}$ particles collected in downtown Mexico City. *Int. J. PIXE*, 15:263–270, 2005.

M. Ammann, M. Kalberer, D.T. Jost, L. Tobler, E. Rossler, D. Piguet, H.W. Gaggeler, and U. Baltensperger. Heterogeneous production of nitrous acid on soot in polluted air masses. *Nature*, 395:157–160, 1998.

J. Arey, S.M. Aschmann, E.S.C. Kwok, and R. Atkinson. Alkyl nitrate, hydroxyalkyl nitrate, hydroxycarbonyl formation from the $NO_x$–air photooxidations of $C_5$–$C_8$ *n*-alkanes. *J. Phys. Chem. A*, 105:1020–1027, 2001.

S.T. Arnold and A.A. Viggiano. Turbulent ion flow tube study of the cluster-mediated reactions of $SF_6^-$ with $H_2O$, $CH_3OH$, and $C_2H_5OH$ from 50 to 500 Torr. *J. Phys. Chem. A*, 105, 2001.

R. Atkinson. Atmospheric chemistry of VOCs and $NO_x$. *Atmos. Environ.*, 34:2063–2101, 2000.

R. Atkinson. Kinetics of the gas-phase reactions of OH radicals with alkanes and cycloalkanes. *Atmos. Chem. Phys.*, 3:2233–2307, 2003.

R. Atkinson. Atmospheric reactions of alkoxy and $\beta$-hydroxyalkoxy radicals. *Int. J. Chem. Kinet.*, 29:99–111, 1997a.

R. Atkinson. Gas-phase tropospheric chemistry of volatile organic compounds: 1. Alkanes and alkenes. *J. Phys. Chem. Ref. Data*, 26:215–290, 1997b.

R. Atkinson, W.P.L. Carter, and A.M. Winer. Effects of temperature and pressure on alkyl nitrate yields in the $NO_x$ photooxidations of *n*-pentane and *n*-heptane. *J. Phys. Chem.*, 87:2012–2018, 1983.

D.G. Aubin and J.P. Abbatt. Adsorption of gas-phase nitric acid to n-hexane soot: Thermodynamics and mechansim. *J. Phys. Chem. A*, 107:11030–11037, 2003.

S. Azimi, V. Rocher, M. Muller, R. Moilleron, and D.R. Thevenot. Sources, distribution and variability of hydrocarbons and metals in atmospheric deposition in an urban area (Paris, France). *Sci. Tot. Environ.*, 337:223–239, 2005.

J.C. Barnard, E.I. Kassianov, T.P. Ackerman, K. Johnson, B. Zuberi, L.T. Molina, and M.J. Molina. Estimation of a "radiatively correct" black carbon specific absorption during the Mexico City Metropolitan Area (MCMA) 2003 field campaign. *Atmos. Chem. Phys.*, 7: 1645–1655, 2007.

M.C. Barth and A.T. Church. Regional and global distributions and lifetimes of sulfate aerosols from Mexico City and southeast China. *J.Geophys. Res.*, 104:30231–30239, 1995.

G. Bench, P.G. Grant, D. Ueda, S.S. Cliff, K.D. Perry, and T.A. Cahill. The use of STIM and PESA to measure profiles of aerosol mass and hydrogen content, respectively, across Mylar rotating drums impactor samples. *Aerosol. Sci. Technol.*, 36:642–651, 2002.

A.K. Bertram, A.V. Ivanov, M. Hunter, L.T. Molina, and M.J. Molina. The reaction probability of OH on organic surfaces of tropospheric interest. *J. Phys. Chem. A*, 105: 9415–9421, 2001.

T.C. Bond, D.G. Streets, K.F. Yarber, S.M. Nelson, J. Woo, and Z. Klimont. A technology-based global inventory of black and organic carbon emissions from combustion. *J. Geophys. Res.*, 109:doi:10.1029/2003JD003697, 2004.

A.H. Bravo, E.R. Sosa, A.P. Sánchez, P.M. Jaimes, and R.M.I. Saavedra. Impact of wildfires on the air quality of Mexico City. *Environ. Poll.*, 117:243–253, 2002.

M. Buback, M. Kling, and S. Schmatz. Decomposition of tertiary alkoxy radicals. *Int. J. Res. Phys. Chem. Chem. Phys.*, 219:1205–1222, 2005.

H. Burtscher, S. Künzel, and C. Hüglin. Characterization of particles in combustion engine exhaust. *J. Aerosol Sci.*, 29:389–396, 1998.

CAM. Inventario de emisiones 2002 de la Zona Metropolitana del Valle México. Technical report, Comisión Ambiental Metropolitana, 2004.

M.J. Campen, J.P. Nolan, M.C.J. Schladweiler, U.P. Kodavanti, P.A. Evansky, D.L. Costa, and W.P. Watkinson. Cardiovascular and thermoregulatory effects on inhaled PM-associated transition metals: A potential interaction between nickel and vanadium sulfate. *Tox. Sci.*, 64:243–252, 2001.

M.R. Canagaratna, J.T. Jayne, D.A. Ghertner, S. Herndon, Q. Shi, J.L. Jimenez, P.J. Silva, P. Williams, T. Lanni, F. Drewnick, K.L. Demerjian, C.E. Kolb, and D.R. Worsnop. Chase studies of particulate emissions from in-use New York City vehicles. *Aerosol Sci. Technol.*, 38:555–573, 2004.

P. Cassanelli, D. Johnson, and R. Anthony Cox. A temperature-dependent relative-rate study of the OH initiated oxidation of *n*-butane: The kinetics of the reactions of the 1- and 2-butoxy radicals. *Phys. Chem. Chem. Phys.*, 7:3702–3710, 2005.

R.S. Chapman, W.P. Watkinson, K.L. Dreher, and D.L. Costa. Ambient particulate matter and respiratory and cardiovascular illness in adults: Particle-borne transition metals and the heart-lung axis. *Environ. Toxicol. Pharmacol.*, 4:331–338, 1997.

M.Y. Choi and C.K. Chan. The effects of organic species on the hygroscopic behaviors of inorganic aerosols. *Environ. Sci. Technol.*, 36:2422–2428, 2002.

K.Y. Choo and S.W. Benson. Arrhenius parameters for the alkoxy radical decomposition reactions. *Int. J. Chem. Kinet.*, 13:833–844, 1981.

J.C. Chow, J.G. Watson, S.A. Edgerton, and E. Vega. Chemical composition of $PM_{2.5}$ and $PM_{10}$ in Mexico City during winter 1997. *Sci. Tot. Environ.*, 287:177–201, 2002.

A.R. Chughtai, M.E. Brooks, and D.M. Smith. Effect of metal oxides and black carbon (soot) on $SO_2/O_2/H_2O$ reaction systems. *Aerosol Sci. Technol.*, 19:121–132, 1993.

A.R. Chughtai, S.A. Gordon, and D.M. Smith. Kinetics of the hexane soot reaction with $NO_2/N_2O_4$ at low concentrations. *Carbon*, 32:405–416, 1994.

A.R. Chughtai, G.R. Williams, M.O. Atteya, N.J. Miller, and D.M. Smith. Carbonaceous particle hydration. *Atmos. Environ.*, 33:2679–2687, 1999.

A.R. Chughtai, J.M. Kim, and D.M. Smith. The effect of air/fuel ratio on properties and reactivity of combustion soots. *J. Atmos. Chem.*, 43:21–43, 2002.

S.H. Chung and J.H. Seinfeld. Global distribution and climate forcing of carbonaceous aerosols. *J. Geophys. Res.*, 107:doi:10.1029/2001JD001397, 2002.

A.D. Clarke, T. Uehara, and J.N. Porter. Atmospheric nuclei and related aerosol fields over the Atlantic: Clean subsiding air and continental pollution during ASTEX. *J. Geophys. Res.*, 102:25281–25292, 1997.

N. Cohen. Are reaction rate coefficients additive? Revised transition state theory calculations for OH + alkane reactions. *Int. J. Chem. Kinet.*, 23:397–417, 1991.

W.F. Cooke and J.J.N. Wilson. A global black carbon aerosol model. *J. Geophys. Res.*, 101:19395–19409, 1996.

S.R. Craig, G.P. Hastie, K.J. Roberts, and J.N. Sherwood. Investigation into the structures of some normal alkanes within the homologous series $C_{13}H_{28}$ to $C_{60}H_{122}$ using high-resolution synchrotron X-ray powder diffration. *J. Mater. Chem.*, 4:977–981, 1994.

B. de Foy, E. Caetano, V. Magaña, A. Zitácuaro, B. Cárdenas, A. Retama, R. Ramos, L.T. Molina, and M.J. Molina. Mexico City basin wind circulation during the MCMA–2003 field campaign. *Atmos. Chem. Phys.*, 5:2267–2288, 2005.

B. de Foy, J.R. Varela, L.T. Molina, and M.J. Molina. Rapid ventilation of the Mexico City basin and regional fate of the urban plume. *Atmos. Chem. Phys.*, 6:2321–2335, 2006.

P.F. DeCarlo, J.G. Slowik, D.R. Worsnop, P. Davidovits, and J.L. Jimenez. Particle morphology and density characterization by combined mobility and aerodynamic diameter measurements. Part 1: theory. *Aerosol Sci. Technol.*, 38:1185–1205, 2004.

S. Decesari, M.C. Facchini, E. Matta, M. Mircea, S. Fuzzi, A.R. Chughtai, and D.M. Smith. Water soluble organic compounds formed by oxidation of soot. *Atmos. Environ.*, 36:1827–1832, 2002.

E. Demou, H. Visram, D.J. Donaldson, and P.A. Makar. Uptake of water by organic films: the dependence on the film oxidation state. *Atmos. Environ.*, 37:3529–3537, 2003.

E.T. Denisov and I.B. Afanas'ev, editors. *Oxidation and Antioxidants in Organic Chemistry and Biology.* Taylor & Francis, Boca Raton, 2005.

R.V. Díaz, F. Aldape, and J. Flores M. Identification of airborne particulate sources, of samples collected in Ticomán, Mexico, using PIXE and multivariate analysis. *Nucl. Instr. Meth. Phys. Res. B*, 189:249–253, 2002.

R.S. Disselkamp, M.A. Carpenter, J.P. Cowin, C.M. Berkowitz, E.G. Chapman, R.A. Zaveri, and N.S. Laulainen. Ozone loss in soot aerosols. *J. Geophys. Res.*, 105:9767–9771, 2000.

D.W. Dockery, C.A. Pope, X. Xu, J.D. Spengler, J.H. Ware, M.E. Fay, B.G. Ferris, and F.E. Speizer. An association between air pollution and mortality in six U.S. cities. *New Engl. J. Med.*, 329:1753–1759, 1993.

L. D'Ottone, D. Bauer, P. Campuzano-Jost, M. Fardy, and A.J. Hynes. Vibrational deactivation studies of OH X $^2\pi$ ($\nu = 1$–5) by $N_2$ and $O_2$. *Phys. Chem. Chem. Phys.*, 6: 4276–4282, 2004.

J. Eberhard, C. Muller, D.W. Stocker, and J.A. Kerr. Isomerization of alkoxy radicals under atmospheric conditions. *Eviron. Sci. Technol.*, 29:232–241, 1995.

M. Ebert, S. Weinbruch, A. Rausch, G. Gorzawski, P. Hoffmann, H. Wex, and G. Helas. Complex refractive index of aerosols during LACE 98 as derived from the analysis of individual particles. *J. Geophys. Res.*, 107:doi:10.1029/2000JD000195, 2002.

R.A. Eldred and T.A. Cahill. Sulfate sampling artifact from $SO_2$ and alkaline soil. *Environ. Sci. Technol.*, 31:1320–1324, 1997.

T.L. Eliason, J.B. Gilman, and V. Vaida. Oxidation of organic films relevant to atmospheric aerosols. *Atmos. Environ.*, 38:1367–1378, 2004.

W. Esteve, H. Budzinski, and E. Villenave. Relative rate constants for the heterogeneous reactions of $NO_2$ and OH radicals with polycyclic aromatic hydrocarbons adsorbed on carbonaceous particles. Part 2: PAHs adsorbed on diesel particulate exhaust SRM 1650a. *Atmos. Environ.*, 40:201–211, 2006.

M.C. Facchini, M. Mircea, S. Fuzzi, and R.J. Charlson. Cloud albedo enhancement by surface-active organic solutes in growing droplets. *Nature*, 401:257–259, 1999.

M.C. Facchini, S. Decesari, M. Mircea, S. Fuzzi, and G. Loglio. Surface tension of atmospheric wet aerosol and cloud/fog droplets in relation to their organic carbon content and chemical composition. *Atmos. Environ.*, 34:4853–4857, 2000.

J.D. Fast and S. Zhong. Meteorological factors associated with inhomogeneous ozone concentrations within the Mexico City basin. *J. Geophys. Res.*, 103:18927–18946, 1998.

B.J. Finlayson-Pitts and J.N. Jr. Pitts. *Chemistry of the Upper and Lower Atmosphere.* Academic Press, New York, 2000.

A.M. Florea and D. Büsselberg. Occurrence, use and potential toxic effects of metals and metal compounds. *Biometals*, 19:419–427, 2006.

P. Forster, V. Ramaswamy, P. Artaxo, T. Berntsen, R. Betts, D.W. Fahey, J. Haywood, J. Lean, D.C. Lowe, G. Myhre, J. Nganga, R. Prinn, G. Raga, M. Schulz, and R. Van Dorland. *Climate Change 2007: The Physical Science Basis. Contribution of Working Group I to the Fourth Assessment Report of the Intergovernmental Panel on Climate Change*, chapter Changes in Atmospheric Constituents and in Radiative Forcing. Cambridge University Press, 2007.

S. Gao, D.A. Hegg, P.V. Hobbs, T.W. Kirchstetter, B.I. Magi, and M. Sadilek. Water-soluble organic components in aerosols associated with savanna fires in southern Africa: identification, evolution, and distribution. *J. Geophys. Res.*, 108:doi:10/1029/2002JD002324, 2003.

A. Gaudichet, F. Echalar, B. Chatenet, J.P. Quisefit, G. Maingre, H. Cachier, P. Buat-Menard, P. Artaxo, and W. Maenhaut. Trace elements in tropical African savanna biomass burning aerosols. *J. Atmos. Chem.*, 22:19–39, 1995.

A.J. Ghio and R.B. Devlin. Inflammatory lung injury after bonchial instillation of air pollution particles. *Am. J. Respir. Crit. Care Med.*, 164:704–708, 2001.

I. Grgić, v. Hudnik, and M Bizjak. Aqueous S(IV) oxidation – III. Catalytic effect of soot particles. *Atmos. Environ.*, 27:1409–1416, 1993.

A. Hallberg, J.A. Ogren, K.J. Noone, K. Okada, J. Heintzenberg, and I.B. Svenningsson. The influence of aerosol particle composition on cloud droplet formation. *J. Atmos. Chem.*, 19:153–171, 1994.

L.D. Hansen, J.F. Ryder, N.F. Mangelson, M.W. Hill, K.J. Faucette, and D.J. Eatough. Inaccuracies encountered in sulfur determination by Particle Induced X-ray Emission. *Anal. Chem.*, 52:821–824, 1980.

A.G. Harrison, editor. *Chemical ionization mass spectrometry.* CRC Press, Boca Raton, 1991.

S. Hasegawa and S. Ohta. Some measurements of the mixing state of soot-containing particles at urban and non-urban sites. *Atmos. Environ.*, 36:3899–3908, 2002.

J.D. Hearn, A.J. Lovett, and G.D. Smith. Ozonolysis of oleic acid particles: evidence for a surface reaction and secondary reactions involving Criegee intermediates. *Phys. Chem. Chem. Phys.*, 7:501–511, 2005.

L.G. Huey, D.R. Hanson, and C.J. Howard. Reactions of $SF_6^-$ and $I^-$ with atmospheric trace gases. *J. Phys. Chem.*, 99:5001–5008, 1995.

T. Ishida, S. Tsuneda, N. Nishida, M. Hara, H. Sasabe, and W. Knoll. Surface-conditioning effect of gold substrates on octadecanethiol self-assembled monolayer growth. *Langmuir*, pages 4638–4643, 1997.

A.V. Ivanov, S. Trakhtenberg, A.K. Bertram, Y.M. Gershenzon, and M.J. Molina. OH, $HO_2$, and ozone gaseous diffusion coefficients. *J. Phys. Chem. A*, 111:1632–1637, 2007.

M.Z. Jacobson. A physically-based treatment of elemental carbon optics: Implications for global direct forcing of aerosols. *Geophys. Res. Lett.*, 27:217–220, 2000.

J.T. Jayne, D.C. Leard, X. Zhang, P. Davidovits, K.A. Smith, C.E. Kolb, and D.R. Worsnop. Development of an Aerosol Mass Spectrometer for size and composition analysis of submicron particles. *Aerosol Sci. Technol.*, 33:49–70, 2000.

M. Jiang, L.C. Marr, E.J. Dunlea, S.C. Herndon, J.T. Jayne, C.E. Kolb, W.B. Knighton, T.M. Rogers, M. Zavala, L.T. Molina, and M.J. Molina. Vehicle fleet emissions of black carbon, polycyclic aromatic hydrocarbons, and other pollutants measured by a mobile laboratory in Mexico City. *Atmos. Chem. Phys.*, 5:3377–3387, 2005.

J.L. Jimenez, J.T. Jayne, Q. Shi, C.E. Kolb, D.R. Worsnop, I. Yourshaw, J.H. Seinfeld, R.C. Flagan, X. Zhang, K.A. Smith, J.W. Morris, and P. Davidovits. Ambient aerosol sampling using the Aerodyne Aerosol Mass Spectrometer. *J. Geophys. Res.*, page doi:10.1029/2001JD001213, 2003.

S. Johansson, J.L. Campbell, and K.G. Malmqvist, editors. *Particle-Induced X-ray Emission Spectrometry (PIXE).* John Wiley & Sons, Inc., New York, 1995.

D. Johnson, P. Cassanelli, and R. Anthony-Cox. Correlation-type structure activity relationships for the kinetics of the decomposition of simple and $\beta$-substituted alkoxy radicals. *Atmos. Environ.*, 38:1755–1765, 2004.

K.S. Johnson, B. Zuberi, L.T. Molina, M.J. Molina, M.J. Iedema, J.P. Cowin, D.J. Gaspar, C. Wang, and A. Laskin. Processing of soot in an urban environment: Case study from the Mexico City Metropolitan Area. *Atmos. Chem. Phys.*, 5:3033–3043, 2005.

K.S. Johnson, B. de Foy, B. Zuberi, L.T. Molina, M.J. Molina, Y. Xie, A. Laskin, and V. Shutthanandan. Aerosol composition and source apportionment in the Mexico City Metropolitan Area with PIXE/PESA/STIM and multivariate analysis. *Atmos. Chem. Phys.*, 6:4591–4600, 2006.

K.S. Johnson, R. Gonzalez, L.T. Molina, R.J. Hopkins, A.V. Tivanski, M.K. Gilles, Y. Desyaterik, and A. Laskin. Microscopy and microprobe methods in Mexico City: Single particle studies. MILAGRO Second Science Meeting, Mexico City, May 2007a.

K.S. Johnson, A.V. Ivanov, L.T. Molina, and M.J. Molina. OH-initiated oxidation of organic aerosol. *in preparation for J. Phys. Chem. A*, 2007b.

K.S. Johnson, V. Shutthanandan, Y. Xie, A. Laskin, B. de Foy, L.T. Molina, K. Dzepina, J.L. Jimenez, D. Salcedo, and M.J. Molina. Aerosol characterization in the Mexico City Metropolitan Area by PIXE/PESA and application in analysis of the organic component. XI International Conference on Particle Induced X-ray Emission (PIXE) and its Analytical Applications, May 2007c.

JPL. Chemical kinetics and photochemical data for use in atmospheric studies. Evaluation 15, Jet Propulsion Laboratory, 2003.

H. Jung, D.B. Kittelson, and M.R. Zachariah. The influence of engine lubricating oil on diesel nanoparticle emissions and kinetics of oxidation. *SAE Technical Paper Series*, pages 2003–01–3179, 2003.

C.O. Justice, L. Giglio, S. Korontzi, J. Owens, J.T. Morisette, D. Roy, J. Descloitres, S. Alleaume, F. Petitcolin, and Y. Kaufman. The MODIS fire products. *Rem. Sens. Environ.*, 83:244–262, 2002.

M. Kalberer, D. Paulsen, M. Sax, M. Steinbacher, J. Dommen, A.S.H. Prevot, R. Fisseha, E. Weingartner, V. Frankevich, R. Zenobi, and U. Baltensperger. Identification of polymers as major components of atmospheric organic aerosols. *Science*, 303:1659–1662, 2004.

S. Kamm, O. Mohler, K.H. Naumann, H. Saathoff, and U. Schurath. The heterogeneous reaction of ozone with soot aerosol. *Atmos. Environ.*, 33:4651–4661, 1999.

M. Kanakidou, J.H. Seinfeld, S.N. Pandis, I. Barnes, F.J. Dentener, M.C. Facchini, R. Van Dingenen, B. Ervens, A. Nenes, C.J. Nielsen, E. Swietlicki, J.P. Putaud, Y. Balkanski, S. Fuzzi, J. Horth, G.K. Moortgat, R. Winterhalter, C.E.L. Myhre, K. Tsigaridis, E. Vignati, E.G. Stephanou, and J. Wilson. Organic aerosol and global climate modelling: a review. *Atmos. Chem. Phys.*, 5:1053–1123, 2005.

Y. Katrib, S.T. Martin, H. Hung, Y. Rudich, H. Zhang, J.G. Slowik, P. Davidovitz, J.T. Jayne, and D.R. Worsnop. Products and mechanisms of ozone reactions with oleic acid

for aerosol particles having core-shell morphologies. *J. Phys. Chem. A*, 108:6686–6695, 2004.

K.A. Katrinak, P. Rez, and P.R. Buseck. Structural variations in individual carbonaceous particles from an urban aerosol. *Environ. Sci. Technol.*, 26:1967–1976, 1992.

S.H. Kim, R.A. Fletcher, and M.R. Zachariah. Understanding the difference in oxidative properties between flame and diesel soot nanoparticles: The role of metals. *Environ. Sci. Technol.*, 11:4021–4026, 2005.

U. Kirchner, V. Scheer, and R. Vogt. FTIR spectroscopic investigation of the mechanism and kinetics of the heterogeneous reactions of $NO_2$ and $HNO_3$ with soot. *J. Phys. Chem. A*, 104:8908–8915, 2000.

D.B. Kittelson, W.F. Watts, J.C. Savstrom, and J.P. Johnson. Influence of a catalytic stripper on the response of real time aerosol instruments to diesel exhaust aerosol. *J. Aerosol Sci.*, 36:1089–1107, 2005.

L.I. Kleinman, P.H. Daum, Y. Lee, G.I. Senum, S.R. Springston, J. Wang, C. Berkowitz, J. Hubbe, R.A. Zaveri, F.J. Brechtel, J. Jayne, T.B. Onasch, and D. Worsnop. Aircraft observations of aerosol composition and ageing in New England and Mid-Atlantic states during the summer 2002 New England Air Quality Study field campaign. *J. Geophys. Res.*, 112:doi:10.1029/2006JD007786, 2007.

D.A. Knopf, J. Mak, S. Gross, and A.K. Bertram. Does atmospheric processing of saturated hydrocarbon surfaces by $NO_3$ lead to volatilization? *Geophys. Res. Lett.*, 33: doi:10.1029/2006GL026884, 2006.

C.E. Kolb, S.C. Herndon, J.B. McManus, J.H. Shorter, M.S. Zahniser, D.D. Nelson, J.T. Jayne, M.R. Canagaratna, and D.R. Worsnop. Mobile laboratory with rapid response instruments for real-time measurements of urban and particulate distributions and emission source characteristics. *Environ. Sci. Technol.*, 38:5694–5703, 2004.

R. Kotzick and R. Niessner. The effects of the aging process on critical supersaturation ratios of ultrafine carbon aerosols. *Atmos. Environ.*, 33:2669–2677, 1999.

G.S. Kowalczyk, G.E. Gordon, and S.W. Rheingrover. Identification of atmospheric particulate sources in Washington, D.C. using chemical element balances. *Environ. Sci. Technol.*, 16:79–90, 1982.

E.S.C. Kwok, J. Arey, and R. Atkinson. Alkoxy radical isomerization in the OH radical-initiated reactions of $C_4$–$C_8$ *n*-alkanes. *J. Phys. Chem.*, 100:214–219, 1996.

A. Laskin, M.J. Iedema, and J.P. Cowin. Time-resolved aerosol collector for CCSEM/EDX single-particle analysis. *Aerosol Sci. Technol.*, 37:246–260, 2003.

J. Li, M. Pósfai, P.V. Hobbs, and P. Buseck. Individual aerosol particles from biomass burning in southern Africa: 2. Compositions and aging of inorganic particles. *J. Geophys. Res.*, 108:doi:10.1029/2002JD002310, 2003.

H.G. Libuda, O. Shestakov, J. Theloke, and F. Zabel. Relative-rate study of thermal decomposition of the 2-butoxyl radical in the temperature range 280-313 k. *Phys. Chem. Chem. Phys.*, 4:2579–2586, 2002.

D.R. Lide, editor. *CRC Handbook of Chemistry and Physics.* CRC Press, Boca Raton, 72nd edition, 2007.

P.D. Lightfoot, R.A. Cox, J.N. Crowley, M. Destriau, G.D. Hayman, M.E. Jenkin, G.K. Moortgat, and F. Zabel. Organic peroxy radicals: Kinetics, spectroscopy and tropospheric chemistry. *Atmos. Environ.*, 26:1805–1961, 1992.

Y.B. Lim and P.J. Ziemann. Products and mechanism of secondary organic aerosol formation from reactions of *n*-alkanes with OH radicals in the presence of $NO_x$. *Environ. Sci. Technol.*, 39:9229–9236, 2005.

C. Lin, S. Chen, K. Huang, W. Hwang, G.C. Chien, and W. Lin. Characteristics of metals in nano/ultrafine/coarse particles collected beside a heavily trafficked road. *Environ. Sci. Technol.*, 39:8113–8122, 2005.

C. Liousse, J.E. Penner, C. Chuang, J.J. Walton, H. Eddleman, and H. Cachier. A global three-dimensional model study of carbonaceous aerosols. *J. Geophys. Res.*, 101:19411–19432, 1996.

J.B. Lipson, T.W. Beiderhase, L.T. Molina, M.J. Molina, and M. Olzmann. Production of HCl in the OH + ClO reaction: laboratory measurements and statistical rate theory calculations. *J. Phys. Chem. A*, 103:6540–6551, 1999.

E.R. Lovejoy, T.P. Murrells, A.R. Ravishankara, and C.J. Howard. Oxidation of $CS_2$ by reaction with OH. 2. Yields of $HO_2$ and $SO_2$ in oxygen. *J. Phys. Chem.*, 94:2386–2393, 1990.

C. Lu and A.W. Czanderna, editors. *Applications of piezoelectric quartz crystal microbalances.* Elsevier, New York, 1984.

M. Mallet, J.C. Roger, S. Depiau, J.P. Putaud, and O. Dubovik. A study of the mixing state of black carbon in urban zone. *J. Geophys. Res.*, 109:doi:10.1029/2003JD003940, 2004.

W.C. Malm, J.F. Sisler, D. Huffman, R.A. Eldred, and T.A. Cahill. Spatial and seasonal trends in particle concentration and optical extinction in the United States. *J. Geophys. Res.*, 99:1347–1370, 1994.

C. Marcolli, B. Luo, and T. Peter. Mixing of the organic aerosol fractions: Liquids as the thermodynamically stable phases. *J. Phys. Chem. A*, 108:2216–2224, 2004.

A. Massling, A. Wiedensohler, B. Busch, C. Neususs, P. Quinn, T. Bates, and D. Covert. Hygroscopic properties of different aerosol types over the Atlantic and Indian Oceans. *Atmos. Chem. Phys.*, 3:1377–1397, 2003.

G. McFiggans, M.R. Alfarra, J. Allan, K. Bower, K. Coe, M. Cubison, D. Topping, P. Williams, S. Decesari, C. Facchini, and S. Fuzzi. Simplification of the representation of the organic component of atmospheric particulates. *Faraday Discuss.*, 130:341–362, 2005.

V.F. McNeill, G.M. Wolfe, and J.A. Thornton. The oxidation of oleate in submicron aqueous salt aerosols: Evidence of a surface process. *J. Phys. Chem. A*, 111:1073–1083, 2007.

R. Méreau, M.T. Rayez, F. Caralp, and J.C. Rayez. Theoretical study on the comparative fate of the 1-butoxy and $\beta$-hydroxy-1-butoxy radicals. *Phys. Chem. Chem. Phys.*, 2: 1919–1928, 2000.

M.F. Mérienne, A. Jenouvrier, and B. Coquart. The $NO_2$ absorption spectrum. I. Absorption cross-sections at ambient temperature in the 300–500 nm region. *J. Atmos. Chem.*, 20:281–297, 1995.

J. Miranda, J.R. Morales, T.A. Cahill, F. Aldape, and J. Flores M. A study of elemental contents in atmospheric aerosols in Mexico City. *Atmósfera*, 5:95–108, 1992.

J. Miranda, T.A. Cahill, J.R. Morales, F. Aldape, J. Flores M., and R.V. Díaz. Determination of elemental concentrations in atmospheric aerosols in Mexico City using Proton Induced X-ray Emission, Proton Elastic Scattering, and laser absorption. *Atmos. Environ.*, 28:2299–2306, 1994.

J. Miranda, E. Andrade, A. López-Suárez, R. Ledesma, T.A. Cahill, and P.H. Wakabayashi. A receptor model for atmospheric aerosols from a southwestern site in Mexico City. *Atmos. Environ.*, 30:3471–3479, 1996.

J. Miranda, V.A. Barrera, A.A. Espinosa, O.S. Galindo, A. Núñez Orosco, R.C. Montesinos, A. Leal-Castro, and J. Meinguer. PIXE analysis of atmospheric aerosols from three sites in Mexico City. *Nucl. Instr. Meth. Phys. Res. B*, 219-220:157–160, 2004.

R.C. Moffet, Y. Desyaterik, R.J. Hopkins, A.V. Tivanski, M.K. Gilles, V. Shutthanandan, L.T. Molina, R.A. Gonzalez, K.S. Johnson, M.J. Molina, V. Mugica, A. Laskin, and K.A. Prather. Characterization of aerosols containing Zn, Pb, and Cl from an industrial region of Mexico City. *in preparation*, 2007.

L.T. Molina, C.E. Kolb, B. de Foy, B.K. Lamb, W.H. Brune, J.L. Jimenez, and M.J. Molina. Air quality in North America's most populous city – overview of MCMA-2003 campaign. *Atmos. Chem. Phys.*, 7:2447–2473, 2007.

M.J. Molina and L.T. Molina, editors. *Air Quality in the Mexico Megacity: an Integrated Assessment.* Kluwer Academic, Boston, 2002.

M.J. Molina, A.V. Ivanov, S. Trakhtenberg, and L.T. Molina. Atmospheric evolution of organic aerosol. *Geophys. Res. Lett.*, 31:doi:10.1029/2004GL020910, 2004.

H. Motz and H. Wise. Diffusion and heterogeneous reaction III. Atom recombination at a catalytic boundary. *J. Chem. Phys.*, 32:1893–1894, 1960.

M. Moya, T. Castro, M. Zepeda, and A. Baez. Characterization of size-differentiated inorganic composition of aerosols in Mexico City. *Atmos. Environ.*, 37:3581–201, 2003.

T. Novakov, S.G. Chang, and A.B. Harker. Sulfates as pollution particulates: Catalytic formation on carbon (soot) particles. *Science*, 186:259–261, 1974.

T. Novakov, M.O. Andreae, R. Gabriel, T.W. Kirchstetter, O.L. Mayol-Bracero, and V. Ramanathan. Origin of carbonaceous aerosols over the tropical Indian Ocean: biomass burning or fossil fuels? *Geophys. Res. Lett.*, 27:4061–4064, 2000.

J.J. Orlando, G.S. Tyndall, and T.J. Wallington. The atmospheric chemistry of alkoxy radicals. *Chem. Rev.*, 103:4657–4689, 2003.

P. Paatero and U. Tapper. Positive matrix factorization: A non-negative factor model with optimal utilization of error estimates of data values. *Environmetrics*, 5:111–126, 1994.

PEMEX. Calidad de combustibles. Technical report, Petróleos Mexicanos (PEMEX), 2003.

M.D. Petters, A.J. Prenni, S.M. Kreidenweis, P.J. DeMott, A. Matsunaga, Y.B. Lim, and P.J. Ziemann. Chemical aging and the hydrophobic-to-hydrophilic conversion of carbonceous aerosol. *Geophys. Res. Lett.*, 33:doi:10.1029/2006GL027249, 2006.

C.A. Pope, R.T. Burnett, M.J. Thun, E.E. Calle, D. Krewski, K. Ito, and G.D. Thurston. Lung cancer, cardiopulmonary mortality, and long-term exposure to fine particulate air pollution. *JAMA*, 287:1132–1141, 2002.

M. Pósfai, J.R. Anderson, and P.R. Buseck. Soot and sulfate aerosol particles in the remote marine troposphere. *J. Geophys. Res.*, 104:21685–21693, 1999.

W.H. Press. *Numerical Recipes in C: The Art of Scientific Computing.* Cambridge University Press, Cambridgeshire, 1992.

G.B. Raga, G.L. Kok, D. Baumgardner, A. Báez, and I. Rosas. Evidence for volcanic influence on Mexico City aerosols. *Geophys. Res. Lett.*, 26:1149–1152, 1999.

J.S. Reid, R. Koppmann, T.F. Eck, and D.P. Eleuterio. A review of biomass burning emissions part II: Intensive physical properties of biomass burning particles. *Atmos. Chem. Phys.*, 5:799–825, 2005.

F. Reisen, S.M. Aschmann, R. Atkinson, and J. Arey. 1,4-hydroxycarbonyl products of the OH radical initiated reactions of $C_5$–$C_8$ *n*-alkanes in the presence of NO. *Environ. Sci. Technol.*, 39:4447–4453, 2005.

C.B. Richardson, R.L. Hightower, and A.L. Pigg. Optical measurement of the evaporation of sulfuric acid droplets. *Appl. Opt.*, 25:1226–1229, 1986.

F.W. Richter, H. Ries, and W. Watjen. On the problem of sulfur losses during PIXE analysis. *Nucl. Instrum. Meth. B*, 3:151–153, 1984.

N. Riemer, H. Vogel, and B. Vogel. Soot aging time scales in polluted regions during day and night. *Atmos. Chem. Phys.*, 4:1885–1893, 2004.

A.L Robinson, N.M. Donahue, M.K. Shrivastava, E.A. Weitkamp, A.M. Sage, A.P. Grieshop, T.E. Lane, J.R. Pierce, and S.N. Pandis. Rethinking organic aerosols: semivolatile emissions and photochemical aging. *Science*, 315:1259–1262, 2007.

W.F. Rogge, M.A. Mazurek, L.M. Hildemann, G.R. Cass, and B.R.T Simoneit. Quantification of urban organic aerosols at a molecular level: Identification, abundance and seasonal variation. *Atmos. Environ.*, 27A:1309–1330, 1993.

Y. Rudich. Laboratory perspective on the chemical transformations of organic matter in atmospheric particles. *Chem. Rev.*, 103:5097–5124, 2003.

Y. Rudich, N.M. Donahue, and T.F. Mentel. Aging of organic aerosol: Bridging the gap between laboratory and field studies. *Ann. Rev. Phys. Chem.*, 58:321–352, 2007.

H. Sakurai, K. Park, P.H. McMurry, D.D. Zarling, D.B. Kittelson, and P.J. Ziemann. Size-dependent mixing characteristics of volatile and nonvolatile components in diesel exhaust aerosols. *Environ. Sci. Technol.*, 34:5487–5495, 2003.

D. Salcedo. Equilibrium phase diagrams of aqueous mixtures of malonic acid and sulfate/ammonium salts. *J. Phys. Chem. A*, 110:12158–12165, 2006.

D. Salcedo, T.B. Onasch, K. Dzepina, M.R. Canagaratna, Q. Zhang, J.A. Huffman, P.F. DeCarlo, J.T. Jayne, P. Mortimer, D.R. Worsnop, C.E. Kolb, K.S. Johnson, B. Zuberi, L.C. Marr, R. Volkamer, L.T. Molina, M.J. Molina, B. Cardenas, R.M. Bernabé, C. Márquez, J.S. Gaffney, N.A. Marley, A. Laskin, V. Shutthanandan, Y. Xie, W. Brune, R. Lesher,

T. Shirley, and J.L. Jimenez. Characterization of ambient aerosols in Mexico City during the MCMA-2003 campaign with Aerosol Mass Spectrometry: Results from the CENICA Supersite. *Atmos. Chem. Phys.*, 6:925–946, 2006.

V. Samburova, R. Zenobi, and M. Kalberer. Characterization of high molecular weight compounds in urban atmospheric particles. *Atmos. Chem. Phys.*, 5:2163–2170, 2005.

M. Schnaiter, H. Horvath, O. Mohler, K.H. Naumann, H. Saathoff, and O.W. Schock. UV-VIS-NIR spectral optical properties of soot and soot-containing aerosols. *J. Aerosol Sci.*, 34:1421–1444, 2003.

J. Schuttlefield, H. Al-Hosney, A. Zachariah, and V.H. Grassian. Attenuated total reflection Fourier Transform Infrared Spectroscopy to investigate water uptake and phase transitions in atmospherically relevant particles. *Appl. Spectr.*, 61:283–292, 2007.

J.H. Seinfeld and S.N. Pandis. *Atmospheric Chemistry and Physics.* John Wiley & Sons, Inc., New York, 1998.

K. Sellegri, P. Laj, R. Dupuy, M. Legrand, S. Preunkert, and J.P. Putaud. Size dependent scavenging efficiencies of multicomponent atmospheric aerosols in clouds. *J. Geophys. Res.*, 108:doi:10/1029/2002JD002749, 2003.

S. Sharma, D. Lavoué, H. Cachier, L.A. Barrie, and S.L. Gong. Long-term trends of the black carbon concentrations in the Canadian Arctic. *J. Geophys. Res.*, 109: doi:10.1029/2003JD004331, 2004.

J.P. Shi and R.M. Harrison. Investigation of ultrafine particle formation during diesel exhaust dilution. *Environ. Sci. Technol.*, 33:3730–3736, 1999.

J.E. Shilling, S.M. King, M. Mochida, D.R. Worsnop, and S.T. Martin. Mass spectral evidence that small changes in composition caused by oxidative aging processes alter aerosol CCN properties. *J. Phys. Chem. A*, 111:3358–3368, 2007.

N.K. Shonija, O.B. Poposicheva, N.M. Persiantseva, A.M. Savel'ev, and A.M. Starik. Hydration of aircraft engine soot particles under plume conditions: effect of sulfuric and nitric acid processing. *J. Geophys. Res.*, 112:doi:10.1029/2006JD007217, 2007.

V. Shutthanandan, S. Thevuthasan, R. Disselkamp, A. Stroud, A. Cavanagh, E.M. Adams, D.R. Baer, L.A. Barrie, S.S. Cliff, M. Jimenez-Cruz, and T.A. Cahill. Development of PIXE, PESA and transmission ion microscopy capability to measure aerosols by size and time. *Nucl. Instr. Meth. Phys. Res. B*, 189:284–288, 2002.

B. Smith, editor. *Infrared Spectral Interpretation: A Systematic Approach.* CRC Press, Boca Raton, 1999.

D.M. Smith and A.R. Chughtai. Reaction kinetics of ozone at low concentrations with *n*-hexane soot. *J. Geophys. Res.*, 101:19607–19620, 1996.

D.M. Smith, J.R. Keifer, M. Novicky, and A.R. Chughtai. An FT-IR study of the effect of simulated solar radiation and various particulates on the oxidation of $SO_2$. *Appl. Spectr.*, 43:103–107, 1989.

E. Smolders and F. DeGryse. Fate and effect of zinc from tire debris in soil. *Environ. Sci. Technol.*, 36:3706–3710, 2002.

A.V. Stepanov, Y.M. Gershenzon, A.V. Ivanov, and M.J. Molina. Atmospheric lifetime of surface alkoxy radicals. 19th International Symposium on Gas Kinetics, July 2006. Orléans, France.

T. Thornberry and J.P.D. Abbatt. Heterogeneous reaction of ozone with liquid unsaturated fatty acids: detailed kinetics and gas-phase product studies. *Phys. Chem. Chem. Phys.*, 6:84–93, 2004.

X. Tie, S. Madronich, S. Walters, D.P. Edwards, P. Ginoux, N. Mahowald, R.Y. Zhang, C. Lou, and G. Brasseur. Assessment of the global impact of aerosols on tropospheric oxidants. *J. Geophys. Res.*, 110:doi:10.1029/2004JD005359, 2005.

H.J. Tobias, D.E. Beving, P.J. Ziemann, H. Sakuri, M. Zuk, P.H. McMurry, D. Zarling, R. Waytulonis, and D.B. Kittelson. Chemical analysis of diesel engine nanoparticles using a Nano-DMA/thermal desorption particle beam mass spectrometer. *Environ. Sci. Technol.*, 35:2233–2243, 2001.

J. Troe. Predictive possibilities of unimolecular rate theory. *J. Phys. Chem.*, 83:114–126, 1979.

UC-Davis. IMPROVE data guide. Technical report, University of California Davis, 1995.

A. Ulman, editor. *An Introduction to Ultrathin Organic Films: From Langmuir–Blodgett to Self-Assembly.* Academic Press, Boston, 1991.

UNFPA. State of world population 2007. Technical report, United Nations, 2007.

E. Vega, I. García, D. Apam, M. Esther Ruiz, and M. Barbiaux. Application of a chemical mass balance receptor model to respirable particulate matter in Mexico City. *J. Air Waste Manage. Assoc.*, 47:524–529, 1997.

E. Vega, V. Mugica, E. Reyes, G. Sanchez, J.C. Chow, and J.G. Watson. Chemical composition of fugitive dust emitters in Mexico City. *Atmos. Environ.*, 35:4033–4039, 2001.

A.A. Viggiano, A.I. Fernandez, and J. Troe. Ion–molecule kinetics at 15–700 Torr. *Phys. Chem. Chem. Phys.*, 7:1533–1539, 2005.

A.K.K. Virtanen, J.M. Ristimaki, K.M. Vaaraslahti, and J. Keskinen. Effect of engine load on diesel soot particles. *Environ. Sci. Technol.*, 38:2551–2556, 2004.

T.J. Wallington, P. Dagaut, and M.J. Kurylo. Ultraviolet absorption cross sections and reaction kinetics and mechanisms for peroxy radicals in the gas phase. *Chem. Rev.*, 92: 667–710, 1992.

M. Wentzel, H. Gorzawski, K.H. Naumann, H. Saathoff, and S. Weinbruch. Transmission electron microscopical and aerosol dynamical characterization of soot aerosols. *J. Aerosol Sci.*, 34:1347–1370, 2003.

F. Zabel, A. Reimer, K.H. Becker, and E.H. Fink. Thermal decomposition of alkyl peroxynitrates. *J. Phys. Chem.*, 93:5500–5507, 1989.

S. Zappoli, A. Andracchio, S. Fuzzi, M.C. Facchini, A. Gelencser, G. Kiss, Z. Krivacsy, A. Molnar, E. Meszaros, H.C. Hansson, K. Rosman, and Y. Zebuhr. Inorganic, organic and macromolecular components of fine aerosol in different areas of Europe in relation to their water solubility. *Atmos. Environ.*, 33:2733–2743, 1999.

J. Zhang, T. Dransfield, and N.M. Donahue. On the mechanism for nitrate formation via the peroxy radical + NO reaction. *J. Phys. Chem. A*, 108:9082–9095, 2004.

Q. Zhang, M.R. Alfarra, D.R. Worsnop, J.D. Allan, H. Coe, M.R. Canagaratna, and J.L. Jimenez. Deconvolution and quantification of hydrocarbon-like and oxygenated organic aerosol based on Aerosol Mass Spectrometry. *Environ. Sci. Technol.*, 39:4938–4952, 2005a.

Q. Zhang, D.R. Worsnop, M.R. Canagaratna, and J.L. Jimenez. Hydrocarbon-like and oxygenated organic aersools in Pittsburgh: Insights into sources and processes of organic aerosols. *Atmos. Chem. Phys.*, 5:3289–3311, 2005b.

B. Zielinska, J. Sagebiel, W.P. Arnott, C.F. Rogers, K.E. Kelly, D.A. Wagner, J.S. Lighty, A.F. Sarofim, and G. Palmer. Phase and size distribution of polycyclic aromatic hydrocarbons in diesel and gasoline vehicle emissions. *Environ. Sci. Technol.*, 38:2557–2567, 2004.

P.J. Ziemann. Aerosol products, mechanisms, and kinetics of heterogeneous reactions of ozone with oleic acid in pure mixed particles. *Faraday Discuss.*, 130:469–490, 2005.

B. Zuberi, K.S. Johnson, G.K. Aleks, L.T. Molina, M.J. Molina, and A. Laskin. Hydrophilic properties of aged soot. *Geophys. Res. Lett.*, 32:doi:10.1029/2004GL021496, 2005.